A Piezo-Tunable Gigahertz Cavity Microelectromechanical Resonator

by

Stephen Ming-Chang Hou

S.B. Electrical Science and Engineering
Massachusetts Institute of Technology, 2003

S.B. Physics
Massachusetts Institute of Technology, 2003

Submitted to the Department of Electrical Engineering and Computer Science
in partial fulfillment of the requirements for the degree of

Master of Engineering in Electrical Engineering and Computer Science

at the

MASSACHUSETTS INSTITUTE OF TECHNOLOGY

May 2004 [June 2004]

Author ....
Department of Electrical Engineering and Computer Science
May 24, 2004

Certified by...............................
Jeffrey H. Lang
Professor of Electrical Engineering
Thesis Supervisor

Accepted by..
Arthur C. Smith
Chairman, Department Committee on Graduate Students

A Piezo-Tunable Gigahertz Cavity Microelectromechanical Resonator

by

Stephen Ming-Chang Hou

Submitted to the Department of Electrical Engineering and Computer Science
on May 24, 2004, in partial fulfillment of the
requirements for the degree of
Master of Engineering in Electrical Engineering and Computer Science

Abstract

RF systems need high-frequency widely-tunable high-Q bandpass filters for channel selection filters and local oscillators. This thesis describes the design, fabrication and testing of a electromagnetic cavity resonator designed for such applications. Alternative technologies provide wide tuning or high Q, but not both, and are generally not tunable. This resonator is distinguished by its simultaneous high Q near 200 and its wide high-frequency tuning range of 2.5 GHz to 4.0 GHz, which have been experimentally demonstrated. The resonator is fabricated using standard MEMS technologies and consists of a gold-lined capacitor and toroidal inductor cavity formed by etching silicon in potassium hydroxide. Frequency tuning is performed by compressing the cavity to close the capacitor gap. Testing was done with a piezoelectric actuator for this task. The match between the modeled and measured impedance is extremely good up to and beyond 5 GHz, with less than a 1% error in magnitude and phase.

Thesis Supervisor: Jeffrey H. Lang
Title: Professor of Electrical Engineering

Acknowledgments

This thesis would not have been possible without the efforts of many people. First, I would like to express gratitude to Prof. Jeffrey Lang, my supervisor and academic advisor, and Prof. Alexander Slocum, the other head of the Nanogate group, for their creative insights and guidance, and also for the countless hours they spent with me.

I would like to thank the other members of the Nanogate group. I am especially grateful to Dr. James White, who worked with me in the lab and in the office fabricating and testing devices, and giving me many pieces of advice throughout. I also want to thank Dave Wentzloff for allowing me use the Agilent network analyzer in Prof. Anantha Chandrakasan's lab and for his help on constructing the wire loops in the resonators, Alexis Weber for his analysis of mechanical stress based on models of my devices and for speaking to me about KOH corner compensation, Alex Sprunt for helping me make graphical models of my devices in ProEngineer, Jian Li for sharing his experience with etching Pyrex, A. John Hart and Jaime Werkmeister for helping me use an SEM to analyze gold coverage over etched slopes, and Xue'en Yang and Joachim Sihler for their invaluable tips on fabrication techniques.

I would to thank other members of the MEMS community at MIT. In particular, I would like to thank Dr. Christine Tsau for sharing her knowledge about gold-gold bonding, and Prof. Joel Voldman for his experience with HF etching. I would like to express great appreciation for the MIT Microsystems Technology Laboratories where my fabrication was carried out. In particular, I am grateful to MTL staff members Kurt Broderick, Paul Tierney and Bob Bicchieri, who patiently trained me on each of the machines, answered my calls and e-mails when I needed help, and offered advice.

I would like to thank the National Science Foundation, MIT Deshpande Center and the MIT Department of Electrical Engineering and Computer Science for their funding of my research. I am also grateful that MIT EECS invited me to present this work at the annual MasterWorks Symposium.

Finally, I would like to thank my family for their unwavering support and encouragement. I am indebted to my parents' love and their dedicated efforts in providing me the opportunities I've had throughtout my education.

Contents

List of Figures

List of Tables

Chapter 1

Introduction

1.1 Motivation and Objective

Microelectromechanical systems (MEMS) is a growing field that deals with the design and fabrication of small scale systems. One such system is a tunable electronic resonator, which has the advantages of being extremely small, easy to produce, and highly resilient to environmental conditions. Applications of these devices include RF systems, such as cell phones and local wireless communication networks, which often need high-frequency widely-tunable high-Q bandpass filters for channel selection filters and local oscillators. Present technologies provide wide tuning or high Q, but not both. For example, crystal resonators exhibit exceptionally high Q, but they are generally not tunable. Mechanical MEMS resonators can also exhibit very high Q, but they are not widely tunable, and do not generally operate in the gigahertz range [19], [40], [41], [28], [39]. Finally, resonators that employ tunable MEMS capacitors can be widely tunable [4], but the associated inductor, often formed through surface micromachining or with a bonding wire, is usually so lossy that a high-Q resonator can not be obtained [8], [11], [43].

This thesis describes the design, fabrication and testing of a cavity MEMS resonator that achieves all three objectives: it operates in the range of 2.5 GHz to 5.0 GHz, which is both wide and in the gigahertz range, and has a Q over 100, which have been experimentally demonstrated. The first report of our work is contained in [14], a paper presented at the 2004 Solid-State Sensor and Actuator Workshop at Hilton Head Island, South Carolina. The resonator is fabricated using standard MEMS technologies and consists of a single gold-lined capacitor and toroidal inductor cavity formed by etching a pair of silicon wafers in potassium hydroxide. Experiments with other etching techniques did not produce smooth enough sidewalls for adequate gold deposition. Frequency tuning is performed by compressing the cavity to close the capacitor gap. Testing is done with an external piezoelectric actuator for this task. When combined with an integrated internal actuator, the resonator is suitable for use in electronically-tunable RF systems. Both electric and magnetic coupling to the resonator are possible. Magnetic coupling was tested by slipping an externally accessible wire loop in slits along the inductor wall. The match between the modeled and measured impedance is extremely good up to and beyond 5 GHz, with less than a 1% error in magnitude and phase.

1.2 Project History

In 2002, James White of the Department of Mechanical Engineering developed the Nanogate as his Ph.D. thesis. The Nanogate is the world's highest precision valve. The gate opening is controlled on a subnanometer scale using a piezoelectric actuator. It enables the ability to control flow channels at nanometer length scales for sensing and filtration of large molecules such as proteins and DNA. Examining the Nanogate, Prof. Jeffrey Lang of the Department of Electrical Engineering and Computer Science proposed coating the plates of the Nanogate with metal and using it as a high-precision tunable capacitor. Coupled with a non-lossy inductor, the resulting device acts as a high-Q tunable resonator. And thus this thesis project was born.

It started as a project under the MIT Undergraduate Research Opportunities Program (UROP). The resonators were designed with Pyrex glass as the base material. Experiments performed with the hydrofluoric acid, the standard etchant for Pyrex, however, did not produce smooth continuous surfaces needed for a conducting layer of metal to be deposited for proper device operation. After this project evolved into a graduate research assistantship (RAship), anisotropic etching of silicon was used instead. When (100) silicon is placed in potassium hydroxide (KOH), planes are etched at an angle of 54.7° from the surface. Four-point probe tests on gold-lined KOH-etched trenches and SEM analysis confirmed that these boundaries are much smoother and not as abrupt as the Pyrex ones so that a conducting layer can be deposited. A major geometric change is that the device can no longer be circularly symmetric. When KOH etches (100) silicon, the etch boundaries of the resulting features as viewed from the surface are always rectagular. Thus, the device is designed to be square symmetric.

The process flow is straightforward, and all fabrication steps were done at the MIT Microsystems Technology Laboratories (MTL). After devices were built, Alexis Weber, a graduate student in the MIT Department of Mechanical Engineering, constructed piezoelectric actuators to tune the resonant frequency. We tested them successfully, and the results are presented here as my thesis project. We experimented with other types of piezoelectric actuators with mixed success. We are currently considering other resonator designs, including electrical coupling, automatic feedback tuning, and more robust packaging.

1.3 Document Organization

This chapter, Chapter 1, explains the motivation and objectives of the thesis and provides a broad overview the chronology of the work. Chapter 2 introduces resonators and shows the physical design of a magnetically-coupled device. An ideal circuit model is provided, and an electromagnetic analysis provides the circuit parameters in terms of the physical dimensions. Chapter 3 explains the fabrication design of the device, including wafer etching, wafer bonding, and mask design. A process flow is provided. Chapter 4 contains the fabrication measurements that confirm that KOH-etching (100) silicon is a viable etch technology for the resonator. Corner compensation was demonstrated. Microscope photographs, SEM images, and electrical measurements showed that a good conducting layer of metal can be deposited over KOH-etched silicon. Chapter 5 is the analysis of data taken from measurements of the frequency response of an actual device. A refined circuit model of the device is provided, and its calculated parameters match well with the predicted values.

The resonator is demonstrated to be widely-tunable, to have high-Q, and to operate in the gigahertz range. Chapter 6 has a summary of the thesis document, conclusions drawn from the project, and suggestions for future work.

There are several appendices that provide more detailed information relevant to the main text. Appendix A contains the physical dimensions for five sizes of resonators and the resulting circuit parameters and resonant frequencies. Appendix B lists chemical formulas for common names and abbreviations used in this document. Appendix C contains the recipe for etching Pyrex with HF. Appendix D contains the full device process flow. Appendix E shows the transparency masks used during fabrication. Appendix F contains the MATLAB codes used for data analysis and plotting.

Finally, a list of reference materials is provided at the end of this document.

Chapter 2

Device Design

This chapter introduces resonators, beginning with a theoretical overview of the classic second-order ideal LC and RLC resonators. The physical design of our magnetically-coupled single-cavity KOH-etched silicon resonator is presented along with ProE-simulated figures and a physical schematic. An ideal circuit model of the magnetically-coupled resonator is proposed. Finally, an electromagnetic analysis provides the circuit parameters in terms of the physical dimensions.

2.1 Ideal Resonators

2.1.1 Lossless LC resonators

Figure 2-1 shows the circuit model of an ideal inductor-capacitor (LC) resonator. It consists of an inductor with fixed inductance L in parallel with a capacitor with tunable capacitance C.

The circuit can be analyzed as a linear time-invariant (LTI) system with the current $i(t)$ as the input signal and the voltage $v(t)$ as the output signal. The transfer function $H_{\mathrm{LC}}(s)$ can be derived from the impedance method, where $X(s)$ denotes the Laplace transform of

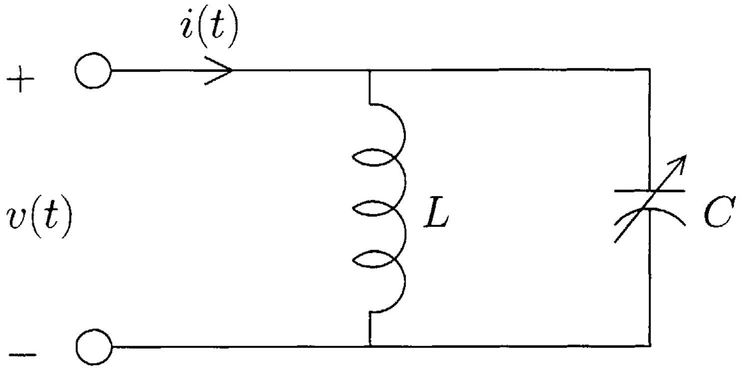

Figure 2-1: Circuit model of an ideal LC resonator.

the time-domain signal $x(t)$. It is

$$
\begin{aligned}
H_{\mathrm{LC}}(s) &= \frac{V(s)}{I(s)} && (2.1)\\
&= sL || \left(\frac{1}{sC}\right) && (2.2)\\
&= \frac{sL \cdot \frac{1}{sC}}{sL + \frac{1}{sC}} && (2.3)\\
\longrightarrow \quad H_{\mathrm{LC}}(s) &= \frac{sL}{1 + s^2LC}. && (2.4)
\end{aligned}
$$

The pole-zero diagram of $H_{\mathrm{LC}}(s)$ for unity L and C is given in Figure 2-2, and the frequency and step responses are given in Figures 2-3.

The LC resonator is a rational second-order system with a zero at the origin and two poles on the $j\omega$ axis at $w = \pm\omega_o$, where ω_o, the *resonant frequency* of the LC resonator, is given by

$$\omega_o = \frac{1}{\sqrt{LC}}. \qquad (2.5)$$

The corresponding frequency response[1] is the transfer function evaluated on the $j\omega$-axis, and is given by

$$H_{\mathrm{LC}}(j\omega) = \frac{j\omega L}{1 - \omega^2 LC}. \qquad (2.6)$$

---

[1] Throughout the rest of this document, all transfer functions and frequency responses shall refer to the complex impedances of single-port circuits.

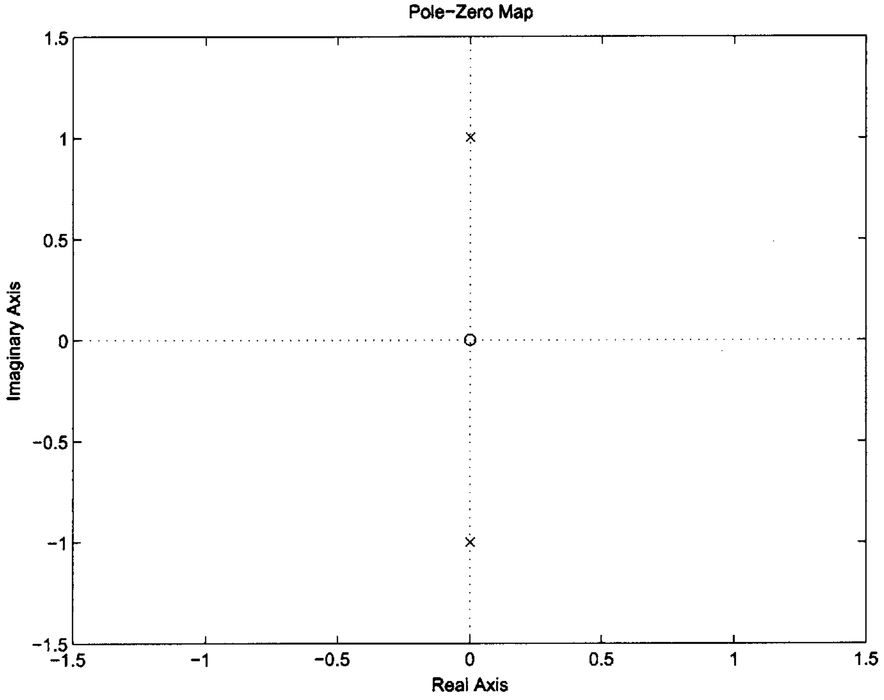

Figure 2-2: Pole-zero diagram of an ideal LC resonator with unity L and C.

From the magnitude plot, we see that this system is a bandpass filter centered around the resonant frequency ω_o. At ω_o, the magnitude of the frequency response is infinite. From the step response, we see that a constant current input results in an everlasting undamped oscillation in voltage that has frequency ω_o.

2.1.2 RLC resonators

In reality, there is some energy dissipation in the system. We can model this effect as a resistor placed in series with the capacitor.[2] Figure 2-4 shows this RLC circuit.

---

[2] Alternatively, we can place a resistor in series with the inductor as well; the poles of the resulting system are the same.

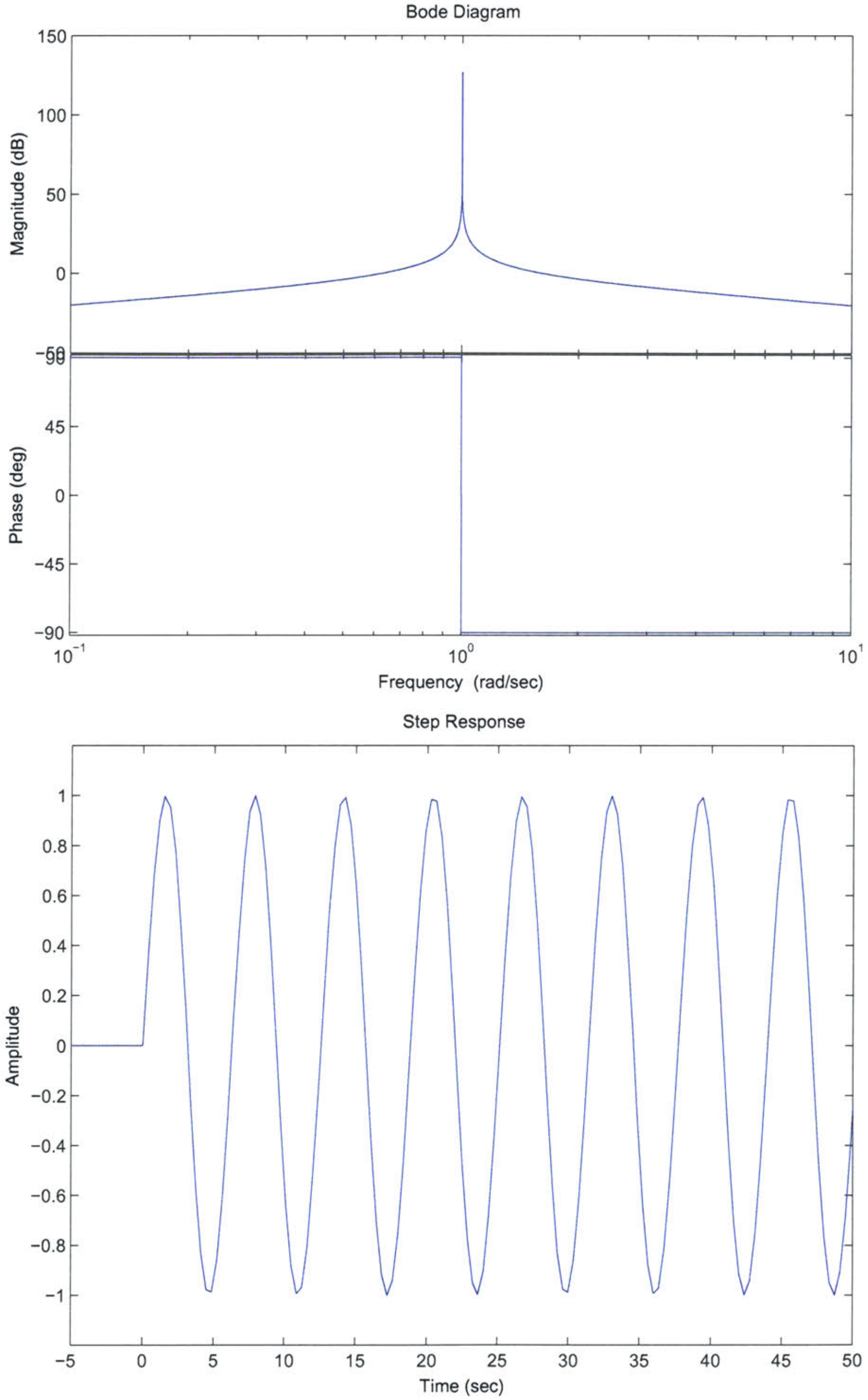

Figure 2-3: Frequency and step responses of an ideal LC resonator with unity L and C.

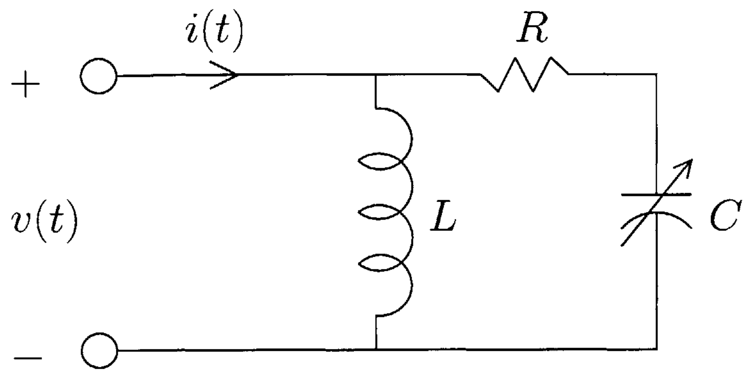

Figure 2-4: Circuit model of an ideal RLC resonator.

Its transfer function is

$$H_{\mathrm{RLC}}(s) = \frac{V(s)}{I(s)} \tag{2.7}$$

$$= sL \| \left(R + \frac{1}{sC}\right) \tag{2.8}$$

$$= \frac{sL\,(R + \frac{1}{sC})}{sL + R + \frac{1}{sC}} \tag{2.9}$$

$$\longrightarrow \quad H_{\mathrm{RLC}}(s) = \frac{Rs^2 + \frac{s}{C}}{s^2 + \frac{R}{L}s + \frac{1}{LC}}. \tag{2.10}$$

We recognize the denominator as that of a damped second-order system, which is of the form

$$D(s) = s^2 + 2\zeta\omega_n s + \omega_n^2, \tag{2.11}$$

where ω_n is the *natural resonant frequency* and ζ is the *damping ratio*.[3] Thus, we can match terms to find the canonical parameters in terms of R, L and C. Matching the no-s-term produces

$$\omega_n = \frac{1}{\sqrt{LC}}, \tag{2.12}$$

which is same as the resonant frequency ω_o for the undamped case; hence the term "natural

---

[3] The rest of this discussion is adapted from [6].

resonant frequency." Matching the s-term produces

$$2\zeta\omega_n = \frac{1}{RC}. \tag{2.13}$$

Combining Equations 2.12 and 2.13, we get the expression for ζ

$$\zeta = \frac{R}{2}\sqrt{\frac{C}{L}}. \tag{2.14}$$

The roots of $s^2 + 2\zeta\omega_n s + \omega_n^2$, or the poles $p_\pm$ of the damped system, are

$$p_\pm = -\zeta\omega_n \pm \omega_n\sqrt{\zeta^2 - 1}. \tag{2.15}$$

When $\zeta > 1$, the roots are real, we can decompose the system into two first-order systems. The impulse response is then two decaying exponentials; we called this the *overdamped* case. When $\zeta = 1$, the roots are equal, and we have the *critically damped* case. Finally, when $\zeta < 1$, both roots are complex

$$p_\pm = -\zeta\omega_n \pm j\omega_n\sqrt{1 - \zeta^2}, \tag{2.16}$$

and we have the *underdamped* case, which has damped oscillations in its impulse response. For $\zeta < \sqrt{2}/2$, there is a maximum peak in the magnitude of the frequency response at

$$\omega_{\text{max}} = \omega_n\sqrt{1 - 2\zeta^2}, \tag{2.17}$$

The dimensionless quantity called the *quality factor*, or Q, is used to describe the sharpness of the peak at $\omega = \omega_{max}$ and is defined as

$$Q \equiv \frac{1}{2\zeta}. \tag{2.18}$$

For the RLC resonator, Q is

$$Q = \frac{1}{R}\sqrt{\frac{L}{C}}. \tag{2.19}$$

We are most interested in the case when Q is in the hundreds so that the bandpass filter is narrow and the system is lightly damped. For a high-Q second-order system that begins with some energy and is allowed to evolve without further input, a useful energy interpretation of Q is that it is 2π times the inverse of the proportion of energy lost per oscillation. Note that if $\zeta \ll 1$, then the real part of the poles is $-\zeta\omega_n$ and the imaginary parts are $\pm\omega_n$

$$p_{\pm} \quad = \quad -\zeta\omega_n \pm j\omega_n. \tag{2.20}$$

The peak magnitude then appears at

$$\omega_{\max} \quad \approx \quad \omega_n. \tag{2.21}$$

The pole-zero diagram of $H_{\mathrm{RLC}}(s)$ for unity L and C is given in Figure 2-5. There are two poles very close to the imaginary axis, a zero at the origin, and a zero at $-\frac{1}{RC}$.

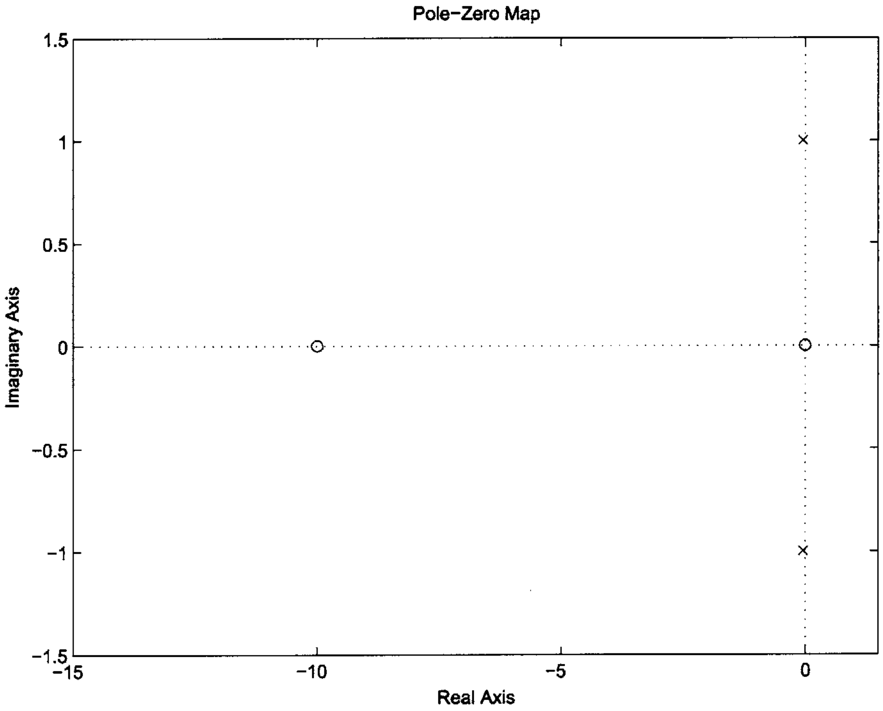

Figure 2-5: Pole-zero diagram of an ideal RLC resonator with unity L and C and $R = 0.1$.

We can use geometric evaluation of rational Laplace transform to examine the behavior of the Bode plot as we move up and down the $j\omega$-axis. If ω moves to $\omega_n \pm \zeta\omega_n$, the length of the vector from the upper pole is scaled by $1/\sqrt{2}$. Power is magnitude squared, so power is cut in half (3 dB lower). Hence, the margin

$$\Delta\omega = 2\zeta\omega_n = \frac{\omega_n}{Q} \tag{2.22}$$

is called the *half-power bandwidth*, or the *full-width half maximum* (FWHM), and is interpreted as the band such that the magnitude is within 3 dB of the maximum. We also see that the angle in this range falls from $-\pi/4$ to $-3\pi/4$. Equation 2.22 provides another interpretation for $Q = \omega_n/\Delta\omega$: the quality factor is the ratio of the resonant frequency to the half-power bandwidth. This is consistent with the notion that Q measures the sharpness of the magnitude peak in the frequency response.

The Bode plots of $H_{\mathrm{RLC}}(j\omega)$ and the step responses for unity L and C and various values of R are given in Figure 2-6. From the magnitude plot, we see that as Q increases (*i.e.* ζ decreases), the half-power bandwidth decreases and the height of the peak increases, both of which result in a better bandpass filter. We see that the step response of the damped system is a exponentially decaying sinusoid. The frequencies of oscillation for all cases are about equal, but the rate of decay decreases as Q increases. Thus, less energy is dissipated per cycle. We can express Q and ω_n in terms of R, L and C as

$$Q = \frac{1}{R}\sqrt{LC}, \tag{2.23}$$

$$\omega_n = \frac{1}{\sqrt{LC}}, \tag{2.24}$$

so we can also express Q as

$$Q = \frac{\omega_n L}{R} = \frac{1}{\omega_n RC}. \tag{2.25}$$

It can verified that a damping resistor in series with the inductor instead of the capacitor would result in the exactly the same expressions for ω_n and Q in terms of R, L and C.

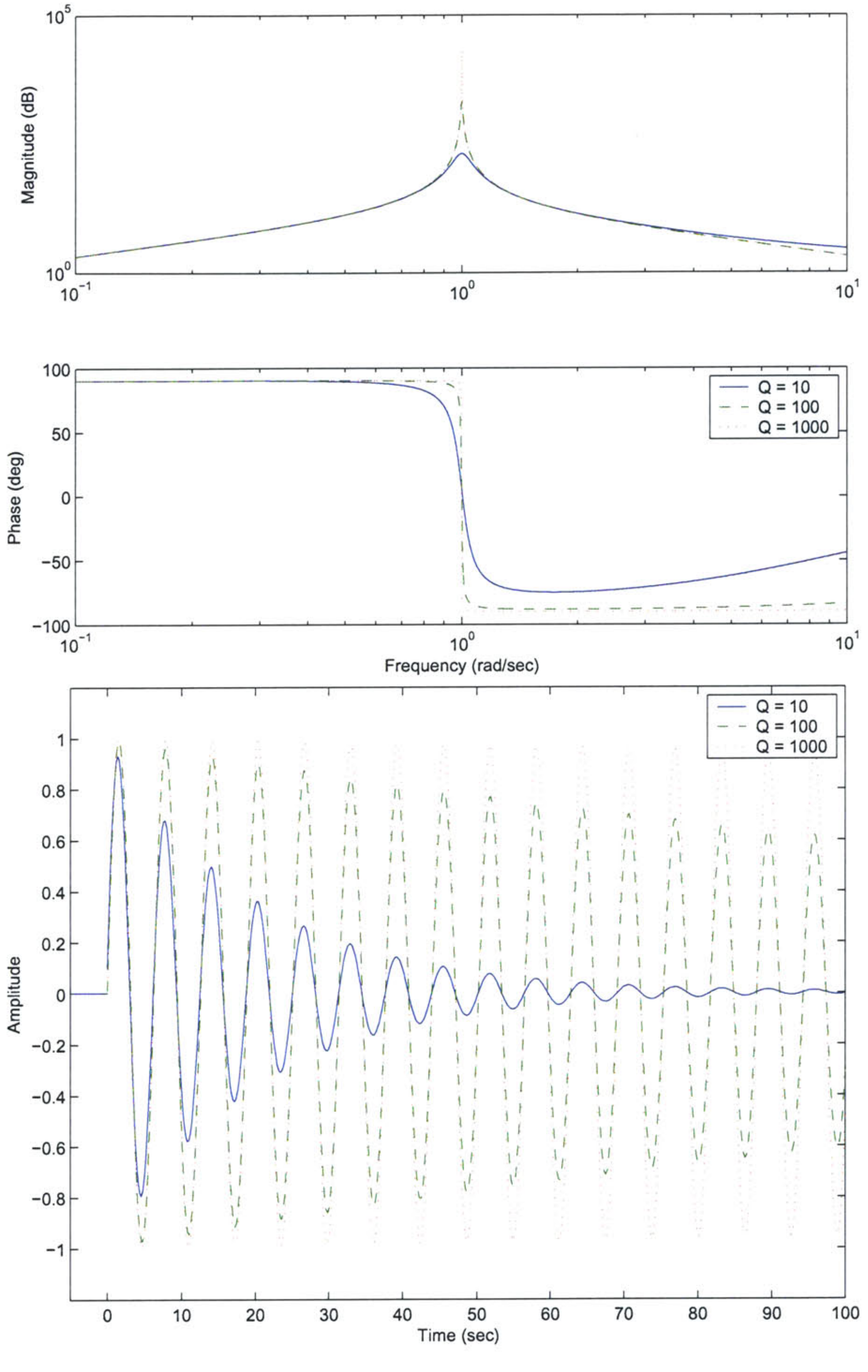

Figure 2-6: Frequency and step responses of an ideal RLC resonator with unity L and C and $R = 0.1$, 0.01, 0.001. $Q = 1/R$, so this is equivalent to $Q = 10$, 100, 1000.

For the devices constructed in this thesis, we will model physical capacitors and inductors as ideal capacitors and inductors in series with inherent resistances. Thus, we shall model a resonator tank to consist of an inductance L_{T} in series with an inductor resistance of R_{LT}, which together are in parallel with a capacitor C_{T} that is in series with a capacitor resistance of R_{CT}. The quality factor Q_{CT} of the capacitor is

$$Q_{\mathrm{CT}} = \frac{1}{\omega_{\mathrm{T}} R_{\mathrm{CT}} C_{\mathrm{T}}}, \tag{2.26}$$

and the quality factor Q_{LT} of the inductor is

$$Q_{\mathrm{LT}} = \frac{\omega_{\mathrm{T}} L_{\mathrm{T}}}{R_{\mathrm{LT}}}. \tag{2.27}$$

Since Q is inversely proportional to resistance, the total tank quality factor Q_{T} is the inverse sum of the individual quality factors, so we have

$$Q_{\mathrm{T}}^{-1} = Q_{\mathrm{CT}}^{-1} + Q_{\mathrm{LT}}^{-1}. \tag{2.28}$$

2.2 Physical Resonators

Our design for building the tunable resonator uses two (100) silicon wafers bonded together. As explained in Section 3.1.4 beginning on Page 48, only rectangular features can be KOH-etched on such wafers, so the gold-coated cavities will be squares instead of circles as viewed from above. The first of three possible designs has the inductor on the outside and the capacitor on the inside. These cavities are self-contained, and are accessible only by a small hole etched through the wafer. A loop of wire placed through the hole interacts with the resonator by mutual inductance to form a transformer. This is the magnetically-coupled design. The next two designs are electrically coupled. The second design has external leads coming out from the capacitor plates by cutting across the inductor cavity. In the third design, the position of the capacitor and inductor are inverted, and the metal from the capacitor is exposed to the outside, which is attached to other devices by direct contact.

Only the first design was fully designed, fabricated and tested, and it is the one presented throughout the rest of this thesis. After testing, it was realized that the electrically-coupled designs are in fact nicer choices due to loop parasitics in the magnetically-coupled resonator. Figure 2-7 shows the side view of the magnetically-coupled resonator design.

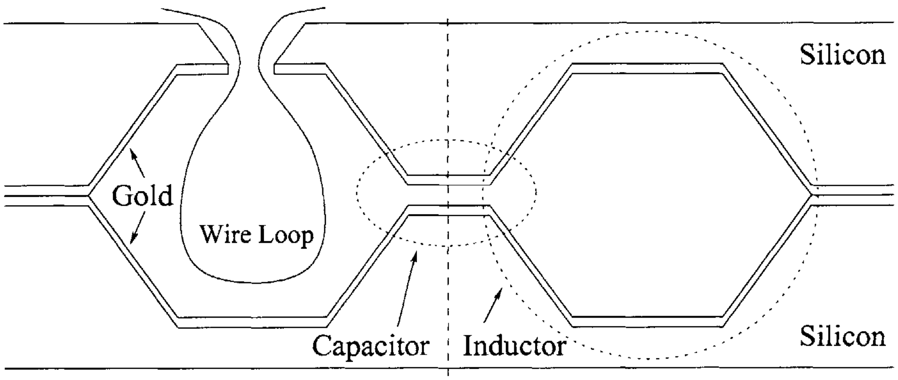

Figure 2-7: Side view of the magnetically-coupled resonator.

At 3 GHz, the wavelength of light is 10 cm. Since a 3-GHz resonator is much smaller than 10 cm, it is a quasi-static device [13]. Therefore, it has identifiable capacitive regions in which electric-field energy storage dominates, and inductive regions in which magnetic-field energy storage dominates. This argument also holds for higher frequency resonators because, as we shall see, size will scale down as frequency scales up. In the resonator shown in Figure 2-7, the central plateau region functions as a parallel-plate capacitor while the surrounding hexagonal-toroidal cavity functions as a single-turn inductor. Together, the central capacitor and the toroidal inductor form a parallel resonant tank. Losses are in the inductor walls and capacitor plates.

2.2.1 Physical Schematic

Figure 2-8 shows the top and side views of the resonator and labels the physical dimensions.

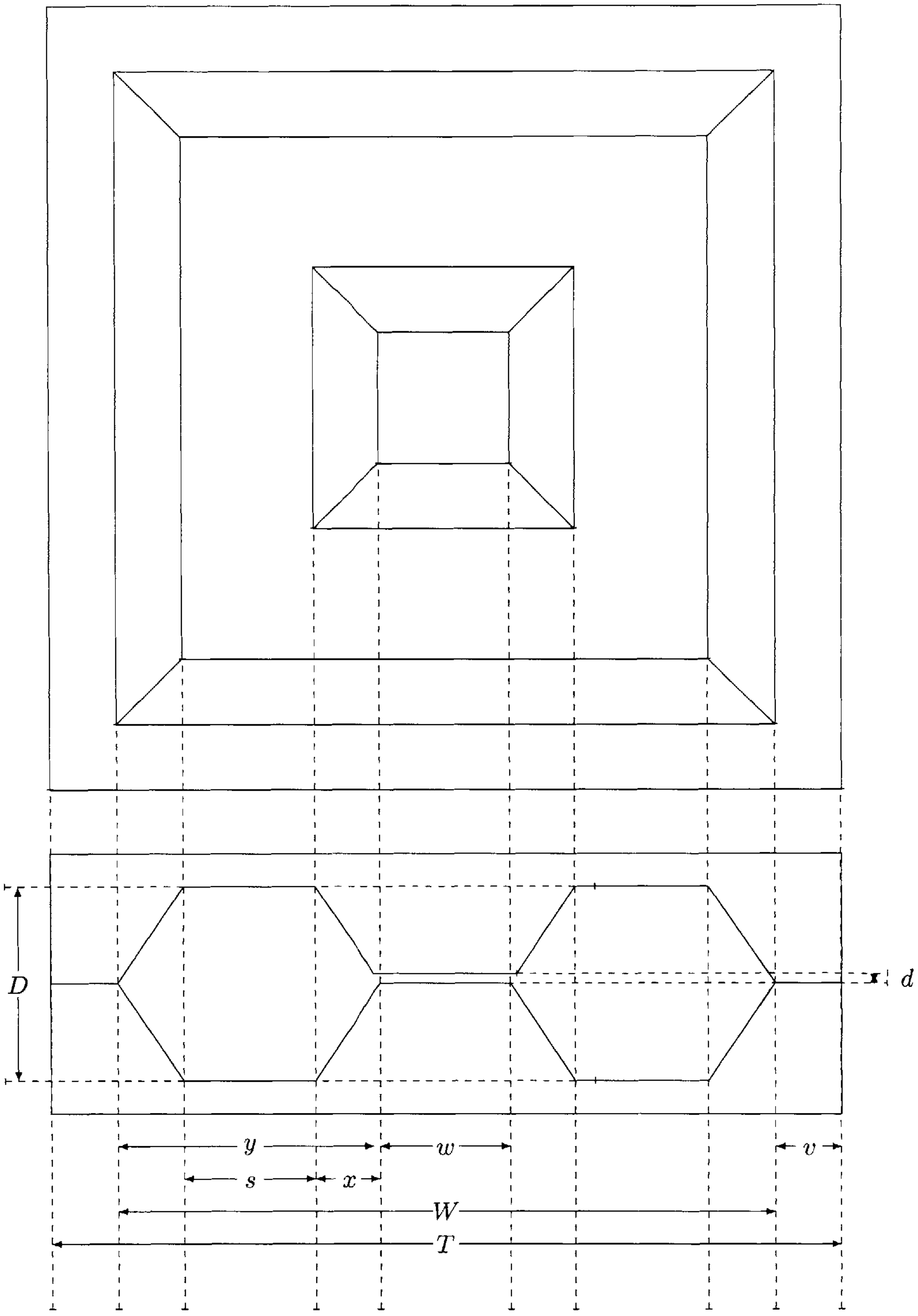

Figure 2-8: Physical schematic of the resonator.

2.2.2 ProE images

Figures 2-9, 2-10, 2-11 and 2-12 show cutaway views of the resonator. These images were produced by Alex Sprunt (MIT MechE) using ProEngineer.

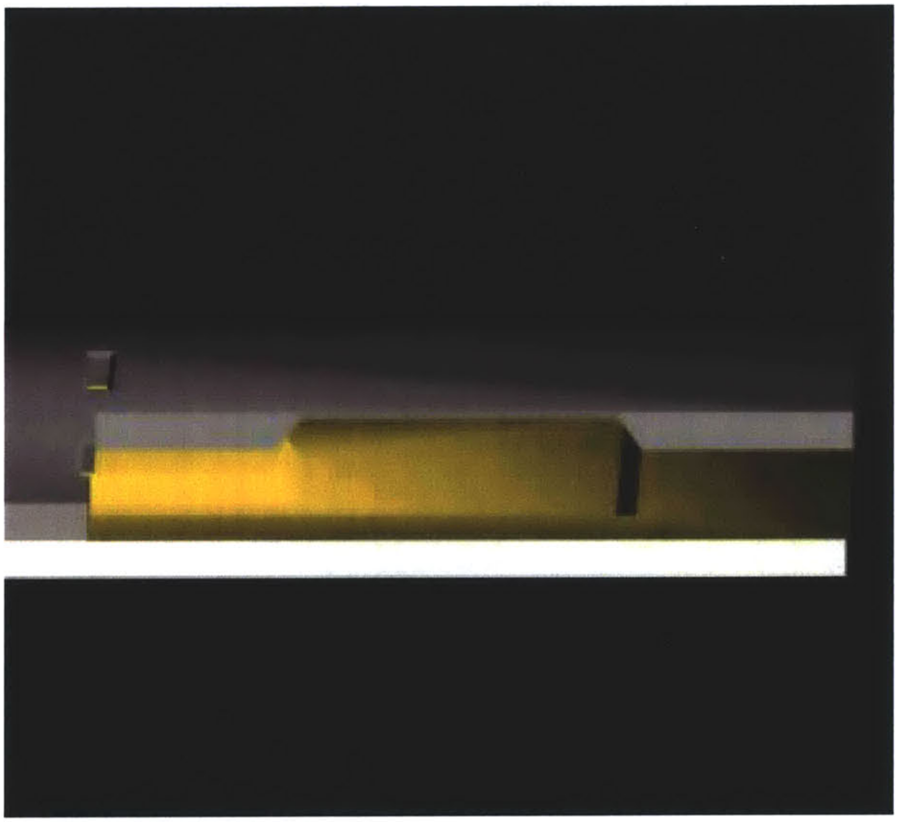

Figure 2-9: Top quarter-cutaway view of resonator model.

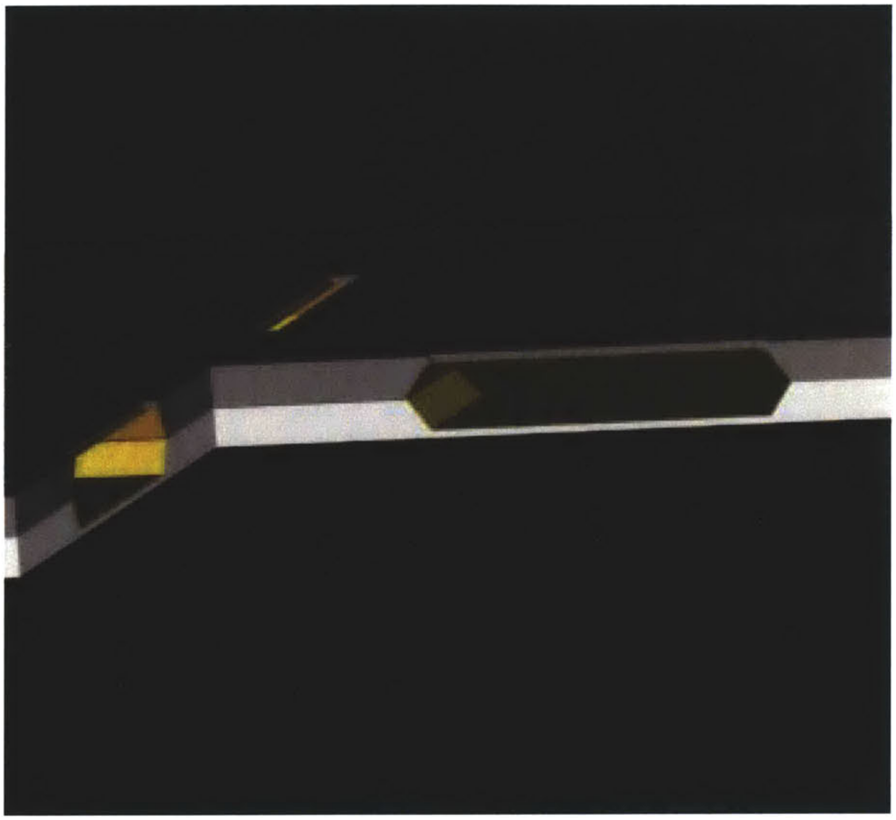

Figure 2-10: Full quarter-cutaway view of resonator model (I).

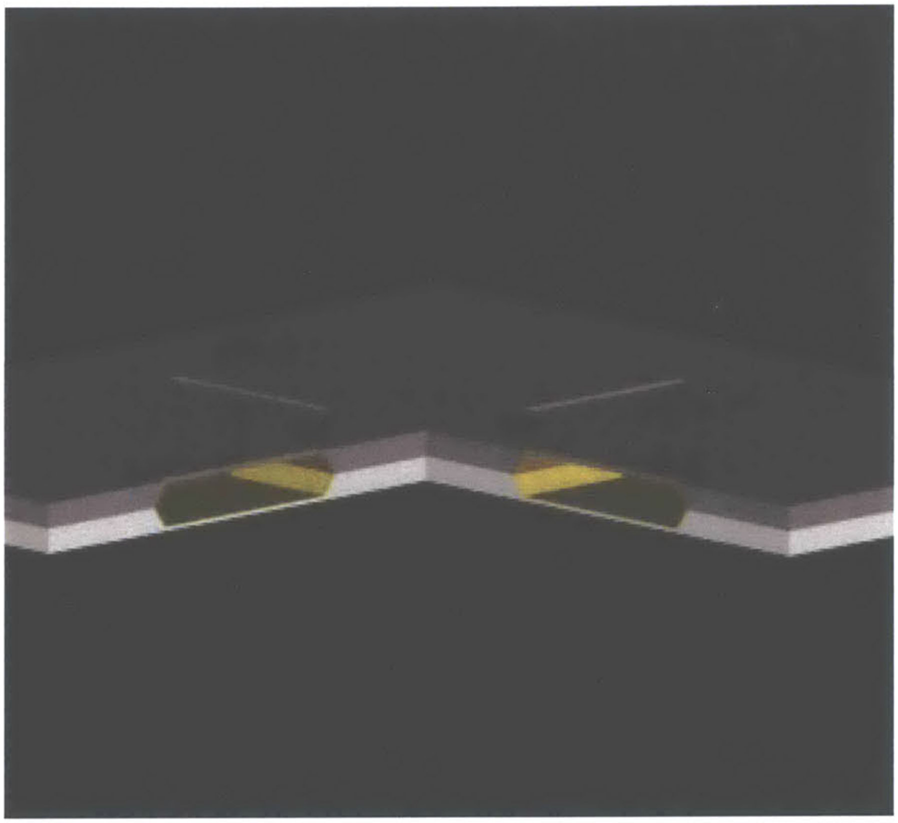

Figure 2-11: Full quarter-cutaway view of resonator model (II).

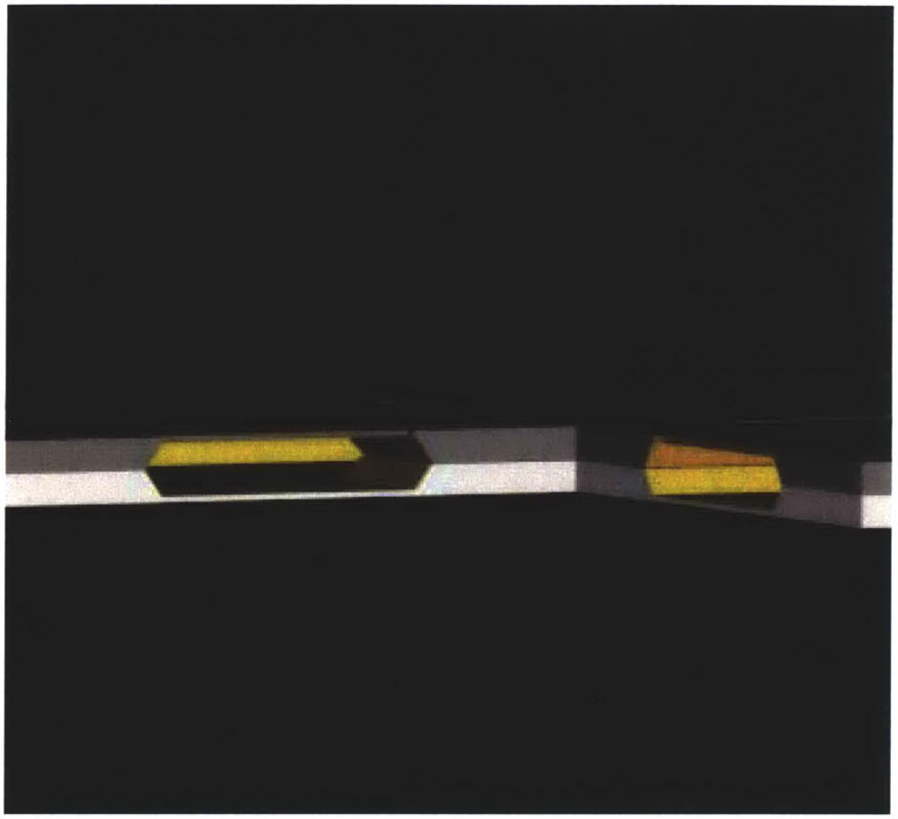

Figure 2-12: Full quarter-cutaway view of resonator model (III).

2.3 Ideal Circuit Model of Magnetically-Coupled Resonator

Before analyzing data from an actual device, we can propose a circuit model for the magnetically-coupled resonator. Denote C_T as the tunable tank capacitance, L_T as the fixed tank inductance and R_T as the total series resistance of the tank inductor and capacitor. These three components in series form one part of the circuit. The wire loop can be modeled as a (non-ideal) inductor with self-inductance L'_L and series resistance R_L. The loop inductor and tank inductor have some mutual inductance $M \equiv \alpha L_\mathrm{T}$, where α is the ratio of the cross-sectional area of the tank inductor that is captured by the loop.

2.3.1 Mutual inductance

To simplify the circuit analysis of mutual inductance, we begin by representing two inductors L_1 and L_2 with mutual inductance M as the circuit in Figure 2-13. The matrix differential equation that describes the two voltages in terms of the two currents is

$$\begin{bmatrix} v_1(t) \\ v_2(t) \end{bmatrix} = \begin{bmatrix} L_1 & \pm M \\ \pm M & L_2 \end{bmatrix} \cdot \frac{\mathrm{d}}{\mathrm{d}t} \begin{bmatrix} i_1(t) \\ i_2(t) \end{bmatrix} \tag{2.29}$$

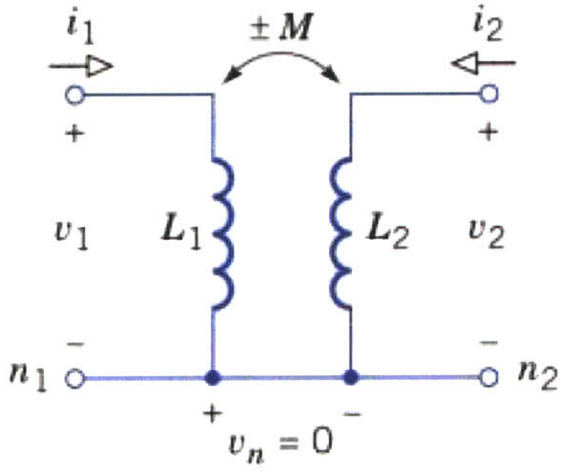

Figure 2-13: Ideal transformer model. Reproduced from [7].

It can be verified that the equivalent T-network circuit model in Figure 2-14 also obeys Equation 2.29. The two parallel inductors are replaced with three inductors with a joint node. The inductor between the joint node and the joint reference ground has inductance M and other two are the original inductances reduced by M.

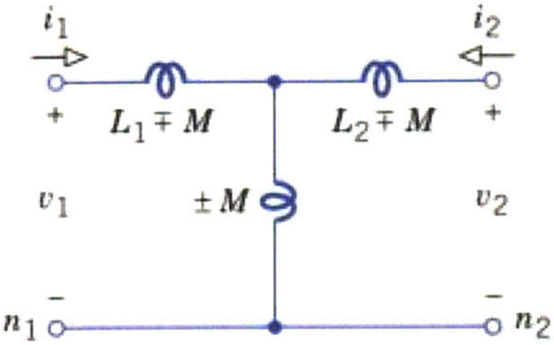

Figure 2-14: Equivalent T-network circuit model. Reproduced from [7].

Thus, the transformer in the resonator can be written in the T-network form. There is now a central inductance αL_{T}, the tank inductor is replaced by one with inductance $L_{\mathrm{T}} - \alpha L_{\mathrm{T}} = (1-\alpha)L_{\mathrm{T}}$, and the loop inductor is replaced by one with inductance $L_{\mathrm{L}} \equiv L'_{\mathrm{L}} - \alpha L_{\mathrm{T}}$. The proposed ideal circuit model for the magnetically-coupled resonator is given in Figure 2-15.

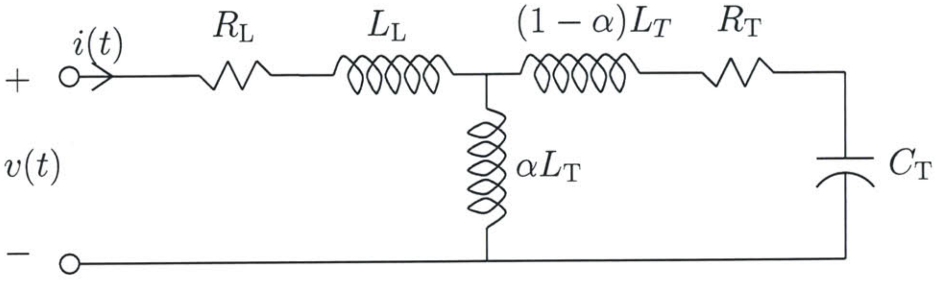

Figure 2-15: Ideal circuit model of magnetically-coupled resonator.

Finally, the transfer function of the system, or the impedance of the circuit, is

$$\begin{aligned} H_{\text{ideal,mag}}(s) &= R_{\text{L}} + sL_{\text{L}} + s\alpha L_{\text{T}} || \left(s(1-a)L_{\text{T}} + R_{\text{T}} + \frac{1}{sC_{\text{T}}} \right) && (2.30) \\ &= R_{\text{L}} + sL_{\text{L}} + \frac{(s\alpha L_{\text{T}}) \left(s(1-a)L_{\text{T}} + R_{\text{T}} + \frac{1}{sC_{\text{T}}} \right)}{s\alpha L_{\text{T}} + s(1-a)L_{\text{T}} + R_{\text{T}} + \frac{1}{sC_{\text{T}}}} && (2.31) \\ \longrightarrow \quad H_{\text{ideal,mag}}(s) &= R_{\text{L}} + sL_{\text{L}} + \frac{(s\alpha L_{\text{T}}) \left((1-a)L_{\text{T}}C_{\text{T}}s^2 + R_{\text{T}}C_{\text{T}}s + 1 \right)}{L_{\text{T}}C_{\text{T}}s^2 + R_{\text{T}}C_{\text{T}}s + 1}. && (2.32) \end{aligned}$$

We defer further circuit analysis to Section 5.5 beginning on Page 104, where a more refined experimental circuit model is developed based on frequency response measurements of actual devices. For now, it is sufficient to note that the denominator $D(s)$ of $H_{\text{ideal,mag}}(s)$ is (after dividing through by $L_{\text{T}}C_{\text{T}}$)

$$D(s) = s^2 + \frac{R_{\text{T}}}{L_{\text{T}}} s + \frac{1}{L_{\text{T}}C_{\text{T}}}. \qquad (2.33)$$

This is exactly the same form as that of the ideal RLC circuit analyzed in Section 2.1.2 on Page 23. Thus, the same expressions for the resonant frequency and quality factors hold.

2.3.2 Electromagnetic analysis

In this subsection, we determine the circuit parameters of the resonator tank in terms of the physical dimensions as labeled in Figure 2-8 on Page 32. Let us denote the side length of the parallel-plate capacitor by w, and the distance across the gap by d. Then, the capacitance of the tank, C_{T}, is approximated by

$$C_{\text{T}} \approx \frac{\epsilon_o w^2}{d}, \qquad (2.34)$$

where $\epsilon_o \approx 8.85 \times 10^{-12}\,\text{F/m}$ is the free-space permittivity. Fringing is ignored in Equation 2.34 since $w \gg d$.

The analysis for the inductor is a bit more involved. Let us denote the outer side length by W and the depth of the cavity by D. From the $54.7^\circ = \arctan\sqrt{2}$ angle characteristic of all KOH-etched sidewalls, we can determine the following quantities in terms of w, W and

D.

- The width y of the hexagon is

$$y = \frac{W-w}{2}. \tag{2.35}$$

- The width x of the sidewall is

$$x = \frac{D\cot(54.7^\circ)}{2} = \frac{D}{2\sqrt{2}}. \tag{2.36}$$

- The width s of the toroidal floor is

$$\begin{aligned} s &= y - 2x && (2.37)\\ &= \frac{W-w}{2} - D\cot(54.7^\circ) && (2.38)\\ &= \frac{W-w}{2} - \frac{D}{\sqrt{2}}. && (2.39) \end{aligned}$$

A single-coil solenoidal inductor with cross-sectional area A and path length l has inductance

$$L = \frac{\mu_o A}{l}, \tag{2.40}$$

where $\mu_o = 4\pi \times 10^{-7}\,\mathrm{H/m}$ is the free-space permeability. The cross-sectional area A for our inductor is the area of the hexagon, which can be calculated by taking the area of the a rectangle with height D and width y and subtracting off four triangles with height $D/2$ and width x. It is

$$\begin{aligned} A &= Dy - 4\cdot\frac{1}{2}\cdot\frac{D}{2}\cdot x && (2.41)\\ &= D(y-x) && (2.42)\\ &= D\left(\frac{W-w}{2} - \frac{D/\sqrt{2}}{2}\right) && (2.43)\\ \longrightarrow \quad A &= \frac{D\left(W-w-D/\sqrt{2}\right)}{2}. && (2.44) \end{aligned}$$

The path of the solenoidal magnetic field through the toroid can be approximated as straight segments with length w when the field travels parallel to the capacitor. As the field rounds the corner, it can be approximated as a quarter-circle with a radius that is half the width of the solenoid. Thus, the mean path length l of the solenoid is approximately

$$l \approx 4w + \frac{\pi(W-w)}{2}. \tag{2.45}$$

Combining Equations 2.40, 2.44 and 2.45, the inductance of the tank, L_T, is thus approximately

$$\begin{aligned} L_\mathrm{T} &\approx \frac{\mu_\mathrm{o} A}{l} && (2.46)\\ &= \frac{\mu_\mathrm{o}\frac{D(W-w-D/\sqrt{2})}{2}}{4w+\frac{\pi(W-w)}{2}} && (2.47)\\ \longrightarrow \quad L_\mathrm{T} &\approx \frac{\mu_\mathrm{o} D(W-w-D/\sqrt{2})}{8w+\pi(W-w)}. && (2.48) \end{aligned}$$

Better approximations for L_T can be obtained from [12]. Thus, by plugging Equations 2.34 and 2.48 into Equation 2.5, the resonant frequency of the device is

$$\begin{aligned} \omega_\mathrm{o} &= \frac{1}{\sqrt{L_\mathrm{T} C_\mathrm{T}}} && (2.49)\\ &\approx \frac{1}{\sqrt{\frac{\mu_\mathrm{o} D(W-w-D/\sqrt{2})}{8w+\pi(W-w)} \cdot \frac{\epsilon_\mathrm{o} w^2}{d}}} && (2.50)\\ &= \frac{1}{\sqrt{\mu_\mathrm{o}\epsilon_\mathrm{o}}} \cdot \sqrt{\frac{d(8w+\pi(W-w))}{D(W-w-D/\sqrt{2})w^2}}. && (2.51) \end{aligned}$$

We further recognize $1/\sqrt{\mu_\mathrm{o}\epsilon_\mathrm{o}}$ as the speed of light $c \equiv 299792458\,\mathrm{m/s}$, so the resonant frequency is

$$\omega_\mathrm{o} = c\sqrt{\frac{d(8w+\pi(W-w))}{D(W-w-D/\sqrt{2})w^2}}. \tag{2.52}$$

The series resistances of the inductor and capacitor can also be determined. Let σ be the metal conductivity, and δ be the smaller of the metal thickness and its skin depth. Since $D \ll (W-w)$ for the resonators described here, the series resistance of the inductor is dominated by the resistance of the metal covering the floor and ceiling of the inductor cavity. In this case, the path length of the solenoidal current around the inductor toroid is approximately $(W - w)$, and the mean cross sectional area through which the current passes is approximately $\delta(W + w)/2$. The series resistance of the tank inductor, R_{LT}, is thus approximately

$$R_{\mathrm{LT}} \approx \frac{2(W - w)}{\sigma\delta(W + w)}. \tag{2.53}$$

Note that when δ is a skin depth, then R_{LT} is a function of frequency. Again, better approximations for R_{LT} can be obtained from [12].

To approximate the series resistance R_{CT} of the tank capacitor, we can model the capacitor electrodes as disks of radius R and thickness δ. Further, assume that the electrodes are uniformly charged, which is the case for a high-Q capacitor. Let $i(t)$ is the total current leaving the capacitor. In this case, the radial current density $\mathbf{J}(\mathbf{r}, t)$ in the electrode at the radius r (vector $\mathbf{r}$) from the center is

$$\mathbf{J}(\mathbf{r}, t) = \frac{i(t)\mathbf{r}}{2\pi\delta R^2}, \tag{2.54}$$

The power dissipation density $p(\mathbf{r}, t)$ is

$$p(\mathbf{r}, t) = \frac{\|\mathbf{J}(\mathbf{r}, t)\|^2}{\sigma}. \tag{2.55}$$

The total power dissipated by the capacitor is the integral of $p(r, t)$ over the volume of both capacitor electrodes

$$\begin{aligned} P(t) &= \int_V p(\mathbf{r},t)\,\mathrm{d}V && (2.56)\\ &= 2\int_0^{\delta}\int_0^{2\pi}\int_0^{R} \frac{\|\mathbf{J}(\mathbf{r},t)\|^2}{\sigma}\underbrace{r\,\mathrm{d}r\,\mathrm{d}\theta\,\mathrm{d}z}_{\mathrm{d}V} && (2.57)\\ &= \frac{2}{\sigma}\int_0^{\delta}\mathrm{d}z\int_0^{2\pi}\mathrm{d}\theta\int_0^{R}\left\|\frac{i(t)\mathbf{r}}{2\pi\delta R^2}\right\|^2 r\,\mathrm{d}r && (2.58)\\ &= \frac{2}{\sigma}\cdot\delta\cdot 2\pi\cdot\frac{i(t)^2}{4\pi^2\delta^2 R^4}\int_0^R r^3\,\mathrm{d}r && (2.59)\\ &= \frac{2}{\sigma}\cdot\delta\cdot 2\pi\cdot\frac{i(t)^2}{4\pi^2\delta^2 R^4}\frac{R^4}{4} && (2.60)\\ \longrightarrow\quad P(t) &= \frac{i(t)^2}{4\pi\sigma\delta}. && (2.61)\end{aligned}$$

Setting this equal to $R_{\mathrm{CT}}i(t)^2$, we obtain the series resistance of the tank capacitor. It is

$$R_{\mathrm{CT}} \approx \frac{1}{4\pi\sigma\delta}. \tag{2.62}$$

Note that when δ is a skin depth, then R_{CT} is also a function of frequency. Once again, better approximations for R_{CT} can be obtained from [12].

2.3.3 Physical dimensions

Based on the expressions derived for the capacitance and inductance in terms of the dimensions of the device, we can design those dimensions to achieve the desired resonant frequency. We would also like sizes that are reasonable to fabricate and that adhere to the approximating assumptions made in the electromagnetic analysis. In Appendix A on Page 121, the size specifications for five types of resonators are given. For simplicity of analysis and fabrication, all resonators have a inductor depth of $D = 1000\,\mu$m and a capacitor gap width of $d = 20\,\mu$m. Although devices of all sizes were constructed, the most extensively studied resonator size was Type C, which has a capacitor width of 4 mm and inductor width of 18 mm, resulting in a theoretical resonant frequency of 4.03 GHz.

There is an additional die border width v which forms the bonding surface between the upper and lower wafers. All resonators fabricated used $v = 2.5\,\mathrm{mm}$, which was large enough to provide ample error margin while die-sawing and sufficient bonding area, while small enough so that not too much force is necessary during the bonding process.

2.4 Summary

We discussed general second-order systems and examined the characteristic quantities of resonant frequency and quality factor. The RLC resonator was studied under this framework. We presented the design of a single-cavity KOH-etched silicon resonator that behaves as an RLC resonator and proposed a circuit model of the magnetically-coupled resonator that took into account the resistances due to the capacitor, inductor and the coupling loop. An electromagnetic analysis showed that, with the appropriate approximations, parts of the resonator could be identified as circuit elements and we determined the tank circuit parameters as functions of the physical dimensions.

Chapter 3

Fabrication Design

This chapter describes the fabrication of the resonator and provides background for each of the key steps, including nitride growth, wafer etching, and wafer bonding. It justifies the choice of using KOH-etching of (100) silicon over HF-etching of Pyrex as the central fabrication technology. The process flow is given and its design explained. The design of the various masks is also described, including corner compensation techniques and mask alignment.

3.1 Wafer Etching

3.1.1 Categories of etches

Wafer etch processes are separated in two groups based on the nature of the etching agent: if the etchant is a liquid in which the wafer is immersed, the etch is *wet*, otherwise the etch is *dry*. Etch process are also categorized by the direction in which they remove material from the wafer: if the wafer is etched equally in all directions, the etch is *isotropic*, and if the wafer is etched preferentially in one or more directions, the etch is *anisotropic*. This categorization is not binary, and there is a continuous measure of how isotropic a particular etch is. Both types of categorizations are independent, and Table 3.1 shows diagrams of examples of the profiles from the four possible combinations of etch types.

Two wet etch technologies were considered for device fabrication:

(I) Hydrofluoric (HF)-etching Pyrex glass (isotropic process)

(II) Potassium hydroxide (KOH)-etching (100) silicon (anisotropic process)

HF on Pyrex is an isotropic etch, and any shape of etch cavity as viewed from the wafer surface can be created. KOH on (100) silicon, on the other hand, is an anisotropic etch, and all etch cavity must be shaped as rectangles parallel with the wafer flat as viewed from the wafer surface. Since the choice of etch technology determines the geometry of of the device and mask design, experiments were first performed with each to determine which to use.

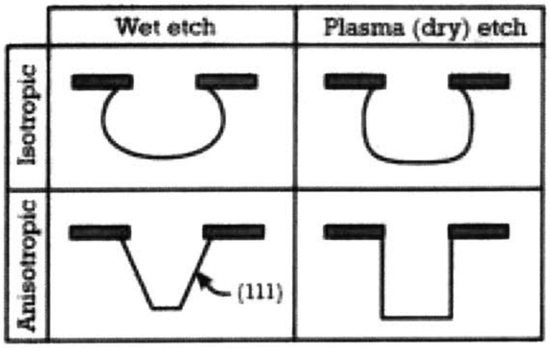

Table 3.1: Diagram of cross-sectional trench profiles resulting from four different types of etch methods. Reproduced from [23].

3.1.2 Pyrex experiments

At first, Pyrex glass was chosen as the primary base material of the cavity resonators. The designed Pyrex LC resonators had two cavities etched in each of two 1 mm thin Pyrex wafers that acted as capacitors and inductors when coated with metal and bonded together. Each were identically etched so that two circularly symmetric cavities were formed: a toroidal inductor on the outside surrounds a circular parallel plate capacitor on the inside. Several methods were examined to etch Pyrex appropriately: 660:140:220 H_2O:HNO_3:HF (0.8 μm/min), buffered oxide etch (BOE), and pure 49% HF:H_2O. I first used BOE, which is a 5:1 mixture of 40% ammonium fluoride (NH_4F) and 49%, and it was found to etch too slowly. Thus, pure hydrofluoric acid was tested instead, but we discovered that standard photoresist could not withstand HF long enough to serve as a mask. Furthermore, replacing photoresist with SU-8 did not solve this problem. Since gold is resistant to HF, it was used as the etch mask, with a layer of the intermediate material bonding chromium deposited between the Pyrex wafer and the gold layer. The full recipe for etching Pyrex is given in Appendix C. The Pyrex wafers are first cleaned with a quick 50:1 HF dip followed by ashing to remove organic residue. This cleaning step is important; without it, the mask is undercut and lifts off. Chromium and gold are then sputtered on the surface. After using standard photolithography with HMDS and positive photoresist, the gold is etched with aqua regia and the chromium is etched with Cr-7 so that Pyrex is exposed.

This recipe was applied to circular Pyrex wafers 100 mm in diameter and 1 mm in thickness. As Table 3.1 suggests, HF undercut the mask to shadow part of the cavity so that a continuous metal layer could not be deposited over the wafer and cavity surfaces. Observation under a microscope confirmed this conclusion and electrical tests showed that no current passed between the metal in the cavity and the metal on the top surface. Thus, silicon etching was considered instead.

3.1.3 Silicon crystal structure

A discussion of the crystal structure of silicon is necessary for understanding KOH etching. Elemental silicon (Si) can exist in crystalline form, which is manufactured as circular wafers of various widths and thicknesses. Crystalline silicon exists in a cubic structure, where a particular cubic pattern of atoms is repeated throughout the wafer. Directions and planar orientations are specified using a notation known as Miller indices. Directions are indicated in brackets $[xyz]$ as if specifying a vector, where x, y and z are the components along those axes and take values of 0 or 1. Because of symmetry, directions with different designations are equivalent, and angle brackets are used to denote a group of such directions. For example, the [100], [010] and [001] directions are called $\langle 100 \rangle$ directions. Likewise, planes are specified using parentheses, where (xyz) specifies the plane normal to the $[xyz]$ direction. Figure 3-1 illustrates the three distinct pairs of directions and planes. Once again from symmetry, planes with different designations are equivalent, and curly brackets are used to denote a group of such planes. For example, the (100), (010) and (001) planes are called {100} planes. The effects of various processes done on the wafers depend on the orientation of the crystal lattice with respect to the wafer plane. The two main types of wafers produced are (111) and (100), where the {111} and {100} planes, respectively, form the wafer surface.

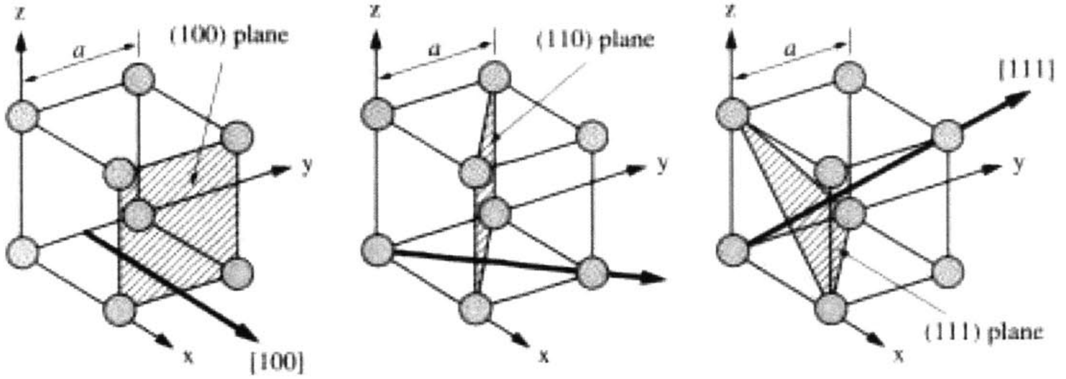

Figure 3-1: Crystal planes and major directions. The shaded planes are the crystal planes and the vector arrow are crystal directions. Reproduced from [29].

3.1.4 Potassium hydroxide etching of (100) silicon

Potassium hydroxide in solution (KOH) etches silicon anisotropically by the redox reaction [23]

$$\mathrm{Si} + 2\mathrm{OH}^- \longrightarrow \mathrm{Si(OH)}_2^{++} + 4\mathrm{e}^-, \qquad \text{(oxidation)} \tag{3.1}$$

$$\mathrm{Si(OH)}_2^{++} + 4\mathrm{e}^- + 4\mathrm{H_2O} \longrightarrow \mathrm{Si(OH)}_6^{--} + 2\mathrm{H}_2. \qquad \text{(reduction)} \tag{3.2}$$

KOH etches {100} planes at a rate about 100 times faster than it etches {111} planes so that the resulting features in the silicon crystal would have faces made up only of {111} planes [23]. When (100) silicon is KOH-etched, the walls of the cavity produced are form a 54.7° angle with the surface plane, and such walls get closer to one another as depth increases, which forms trenches or self-terminating valleys. Furthermore, the shape of the cavity at the surface is always rectangular and bounded by lines in the [100] direction. If the mask used is not bounded as such, the boundaries will grow to the smallest [100]-bounded rectangle that contains the mask. Figure 3-2 shows examples of cavities formed by KOH-etching (100) silicon. If the width of the exposed surface of the wafer is sufficiently small compared to the thickness of the wafer, the etch will self-terminate so that there is effectively no more etching occurring when a V-shaped groove is achieved.

3.1.5 Silicon nitride mask

Silicon nitride (Si_3N_4) can be used a mask for KOH etching and is deposited on silicon by low-pressure chemical vapor deposition (LPCVD). Either of the following reactions can be used [29]:

$$3SiH_2Cl_2 + 4NH_4 \longrightarrow Si_3N + 6HCl + 6H_2 \tag{3.3}$$

$$3SiH_4 + 4NH_4 \longrightarrow Si_3N_4 + 12H_2 \tag{3.4}$$

A very thin layer is sufficient to serve as a mask. In our process, 0.1 μm of nitride can withstand a six-hour KOH etch, which removes 500 μm of silicon. In fact, an unnecessarily thick nitride layer can contribute to thermal stress on the wafer.

3.2 Gold-Gold Thermocompression Bonding

Thermocompression bonding of two metal-coated wafers can be achieved with various metals, but gold is preferred because of resistance to oxidation [36]. It has been demonstrated that standard 4" wafers coated with a 100 Å Ti adhesion layer and 0.8 μm Au bonding layer subjected to relatively low temperatures and pressure, 300° C and 0.5 MPa respectively, successfully bond [36]. This process was adapted for the construction of the resonator cavity. Gold metal layers are deposited onto the cavities etched into two wafers to form conducting surfaces, and these are bonded together by thermocompression.

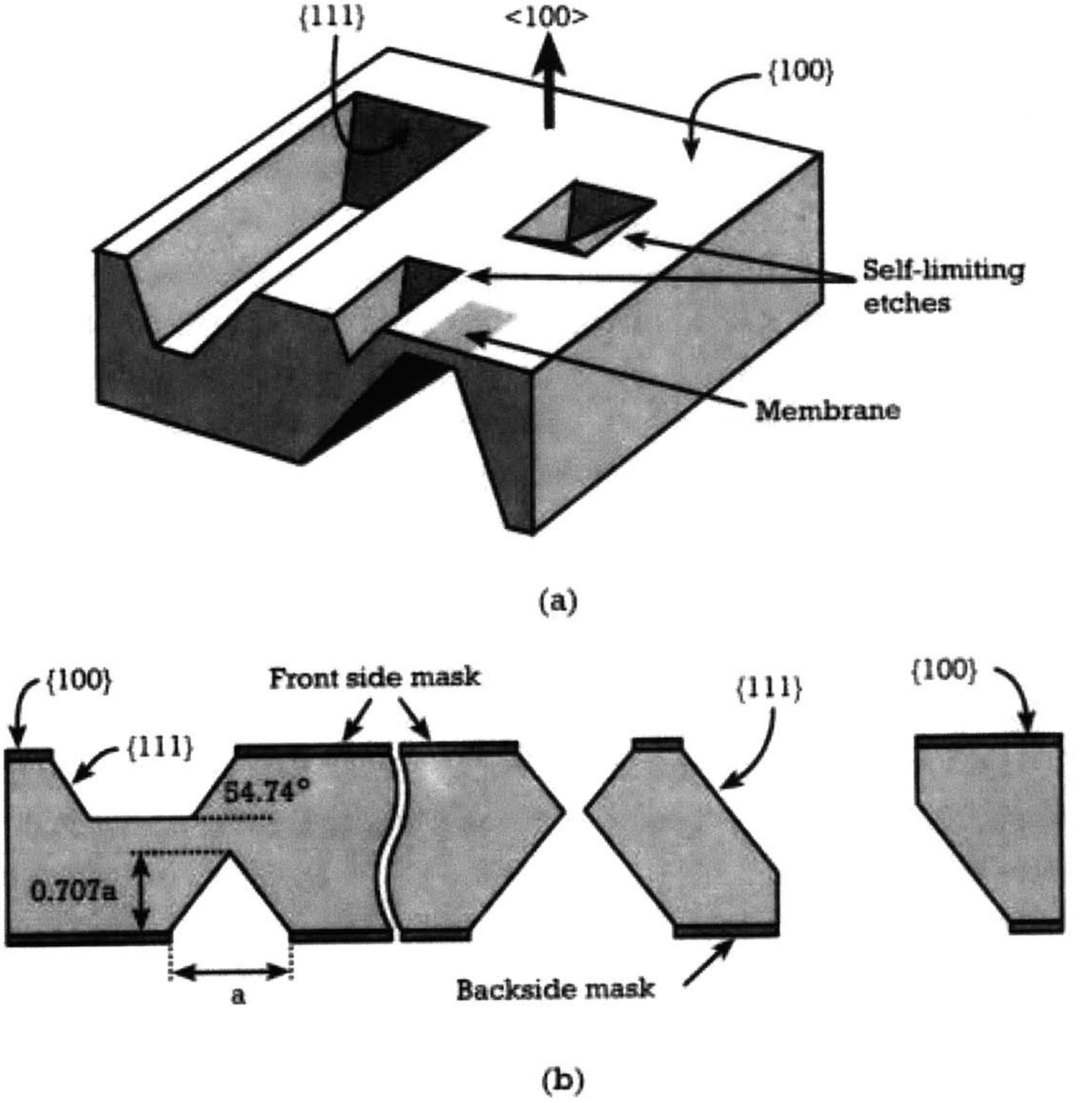

Figure 3-2: Examples of KOH-etching (100) silicon: (a) trenches, self-terminating V-shaped grooves and inverted pyramids; (b) etching from both sides of the wafer. Reproduced from [23].

3.3 Process Design

A timed KOH etch of silicon to form the resonator's inductor cavity is the main step in fabrication. Silicon nitride was selected as the etch mask, and it was prepared with low-pressure chemical vapor deposition (LPCVD) on clean wafers, followed by spinning on standard photoresist and lithography, followed by a reactive ion etch (RIE) of the nitride. Two types of cavities are formed: those with access slits and those without. The wafers with access slits required photolithography from both sides so that KOH would form the slits from the side opposite the cavity.

To construct a 20 μm gap between the two wafers which forms the resonator's capacitor, a short etch is to made in the center plateau of the wafer. The two options considered were RIE and a second KOH etch. RIE was ruled out because the etch removes silicon straight down normal to the wafer plane. Regardless of the area exposed to RIE by a mask, this would have created unwanted walls normal to the capacitor plateau over which a continuous layer of metal could not be deposited. Thus, the second procedure was used instead. The nitride on the plateau is selectively removed by RIE with a mask wafer, which has square holes coinciding with the locations of the capacitor plateaus. To form the mask wafer, silicon wafers goes through the same photolithography (with different chrome masks) as the device wafers and is etched in the same first KOH bath. However, when the device wafers are removed from the bath after a specified period of time, the mask wafers are left in for a least an hour longer so that they would etch all the way through the wafer.

The newly exposed silicon plateau is placed in KOH for a short time (15 minutes) to shave off a thin layer and form a gap. The inductor cavity would also be further etched, but the amount of further etching is very small compared to that already removed; the inductor cavity is 500 μm deep so the additional 20 μm etch would not affect it by much.

The wafers are then cut up by a die saw into individual dies, which are then thoroughly cleaned by ultrasound and piranha to remove microparticles generated during cutting. Chromium adhesion and gold conducting layers are sputtered on the dies. Finally, opposing types of dies are placed face-to-face and individually thermocompressed together to form the resonator device, which is now ready for testing.

3.4 Process Flow

The following is a graphical representation of the process flow for the device wafers that were etched from both sides. The device wafers etched from only side is is similar except there are no slits and step 7 is not used. Only graphics where the wafer shape or layers change are shown. For instance, changes between cleaning steps are not shown. Appendix D beginning on Page 127 contains the complete process chart, specific recipes and descriptions of machines used.

1 RCA clean.

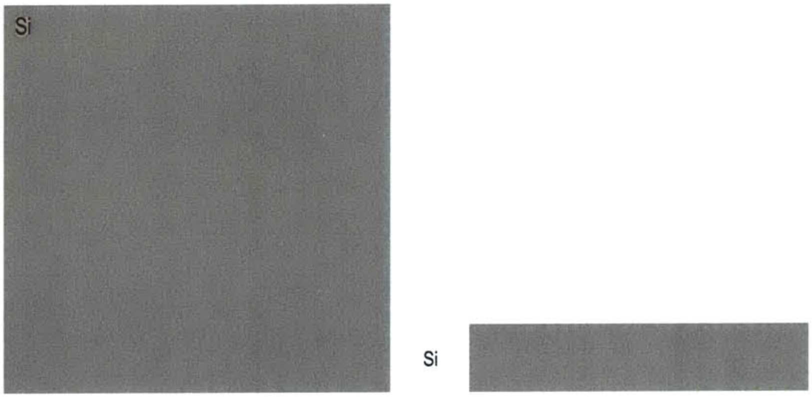

2 Deposit 0.1 μm LPCVD nitride.

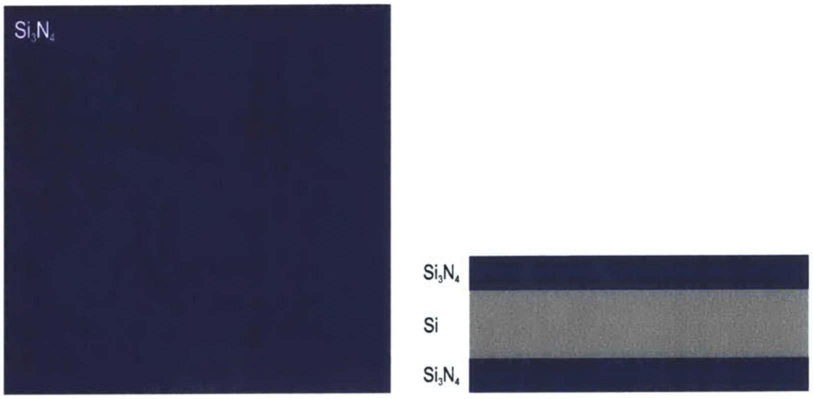

3 Spin PR on front side.

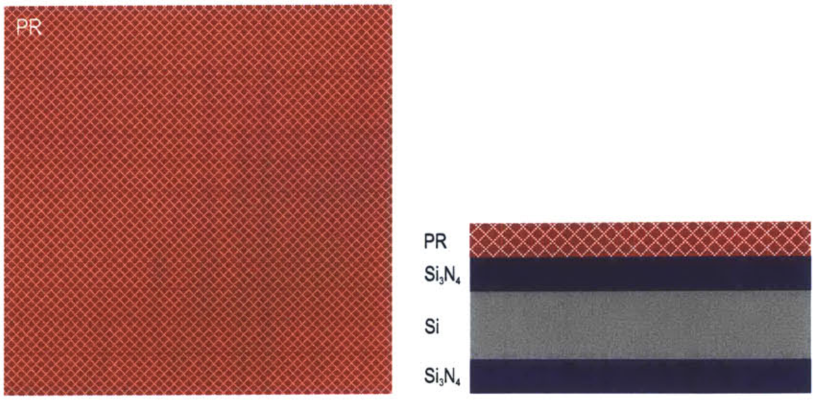

4 Pattern PR.

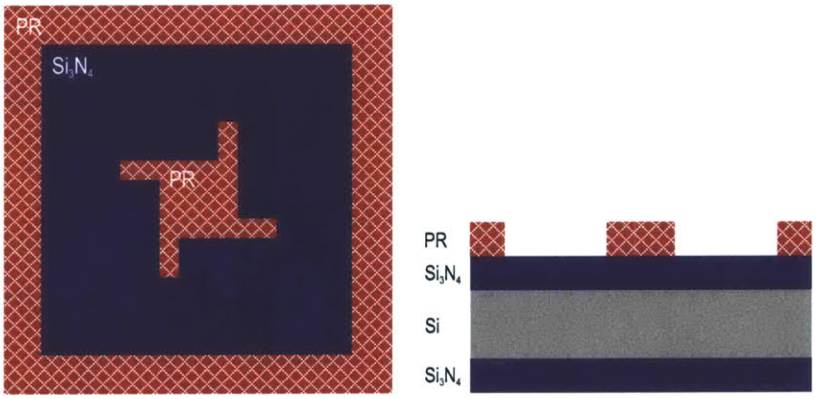

5 RIE etch front side nitride.

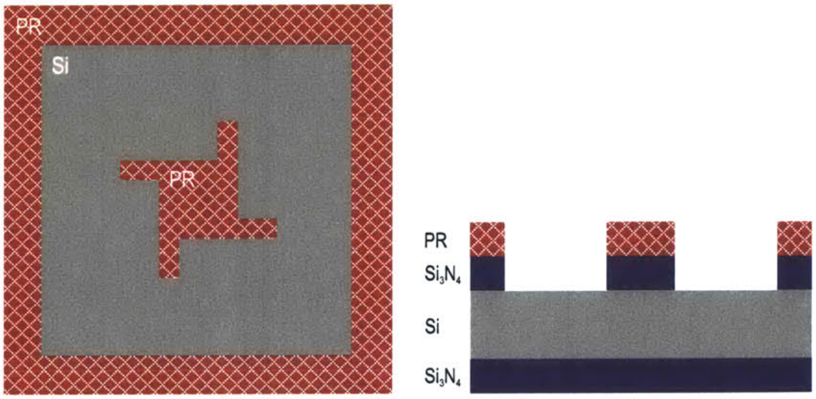

6 Remove PR.

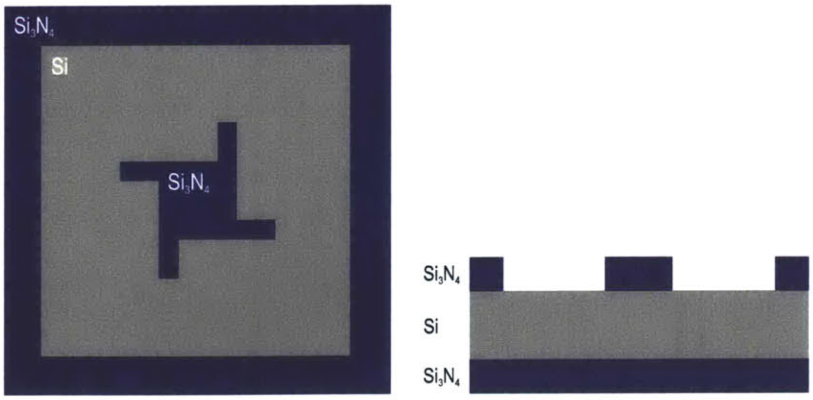

7 Repeat steps 3 – 6 for back side.

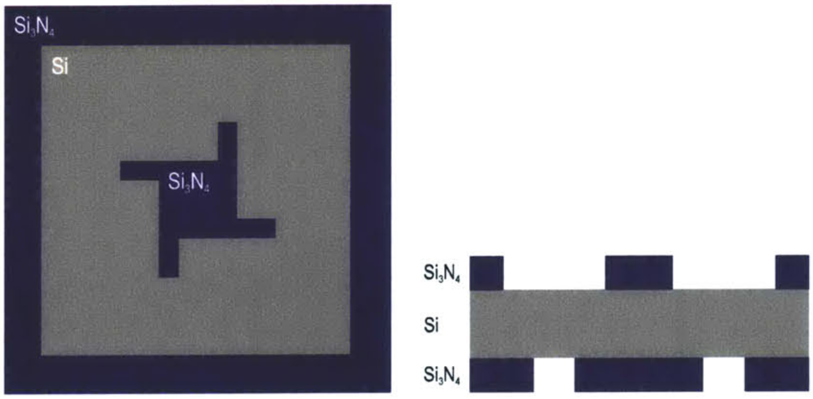

8 & 9 KOH etch & post KOH clean.

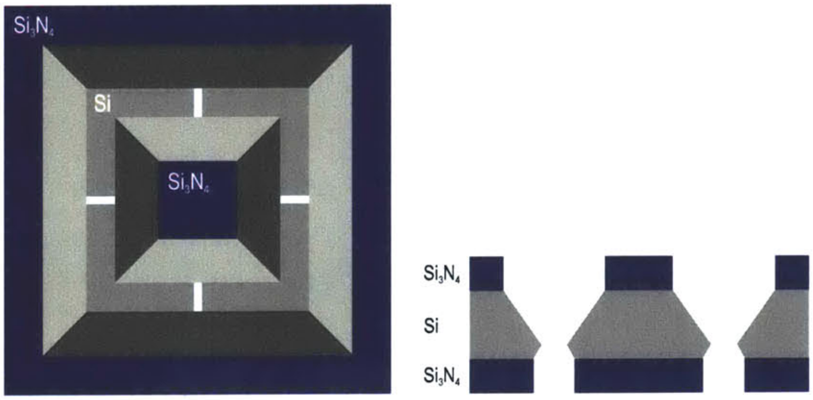

10 RIE etch front side nitride.

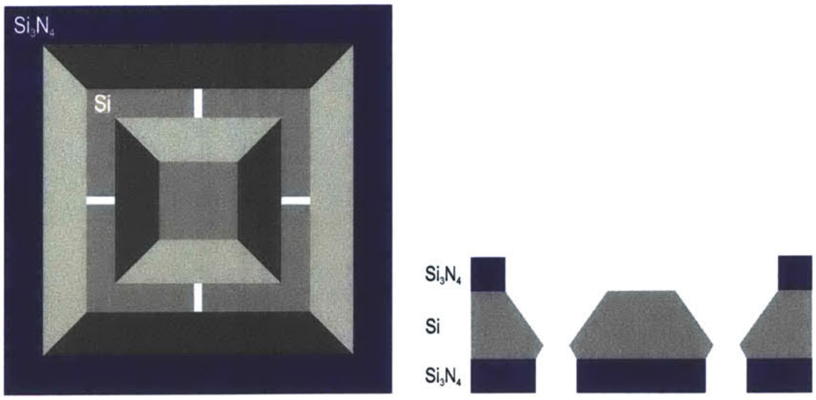

11 & 12 Do another KOH etch & post KOH clean.

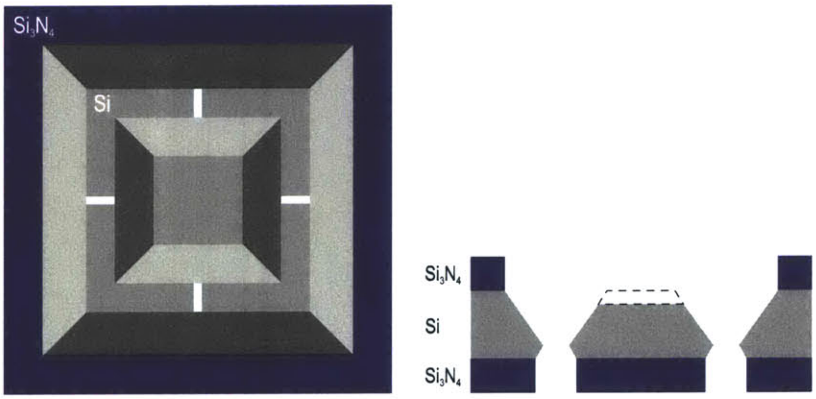

13 Remove nitride.

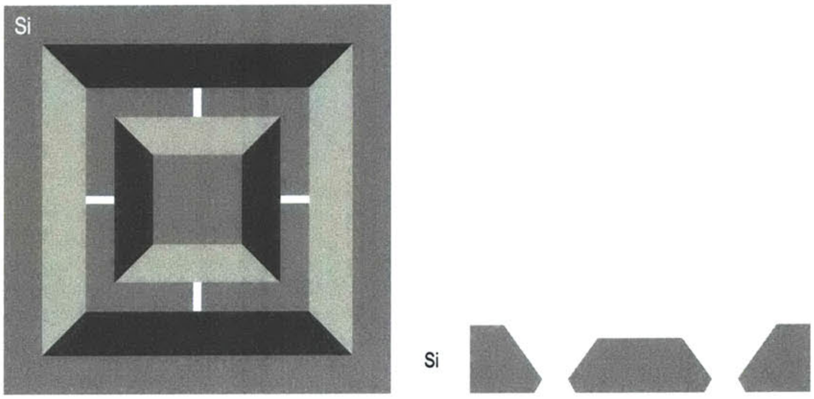

16 Die saw, clean & deposit 0.1 μm Cr & 2 μm Au.

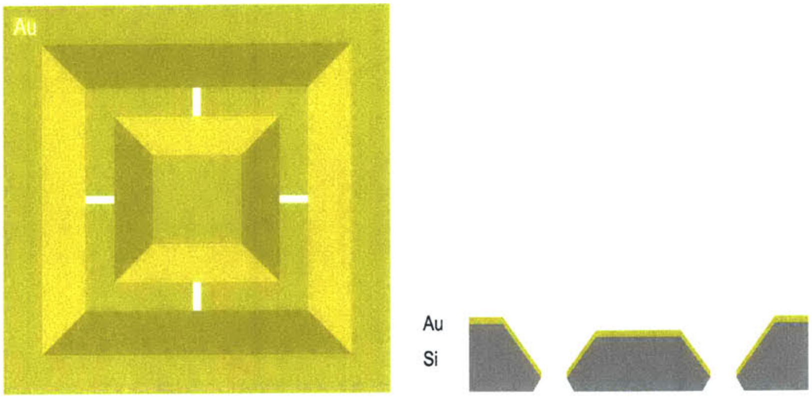

17 Thermocompression bonding.

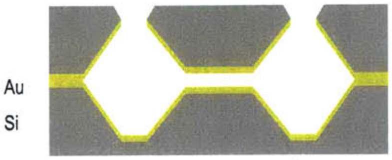

3.5 Mask Design

3.5.1 Number of masks

All masks were drawn using Macromedia Freehand software, printed out on high-quality transparencies, and transferred to 7" chrome masks. Three chrome masks were used in resonator fabrication. Appendix E beginning on Page 129 shows the frontside and backside device masks `wire_loop_resonator_3_mask_a` and `wire_loop_resonator_3_mask_b`, respectively, which create the inductor cavities and slits, respectively. The mask design called `wire_loop_resonator_3_mask_c` was applied to separate wafers to create the wafer mask, which consists of square holes in the wafer.

3.5.2 KOH corner compensation

When KOH etches (100) silicon to form concave corners in the resulting cavities, the deepening sidewalls slope away from the sides and towards the center of the cavity, and the original surface boundaries of the etch are largely unaffected. However, if the mask defines convex corners, then silicon at the corners will get etched away, even at the surface. Figure 3-3 shows an example of this phenomenon. Thus, in order to end up with convex corners in a cavity, the mask must be designed with compensating structures that get etched away just before the desired corner is destroyed. The size and shape of these structures depend on the desired etch depth and the relative etch rates of KOH on different planes of silicon.

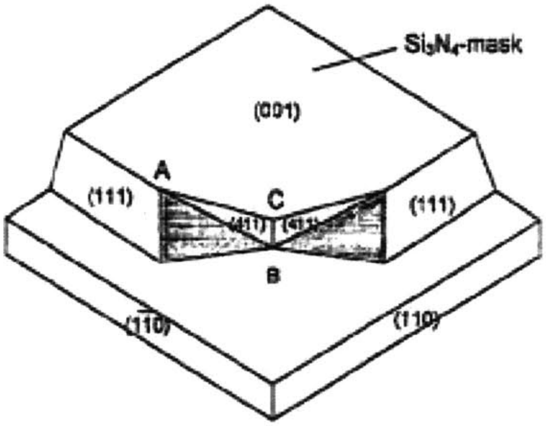

Figure 3-3: The result of KOH-etching (100) silicon when the mask has a convex corner. Reproduced from [44].

The resonator cavity has convex corners, so compensation structures had to be used. There are several such candidate structures from the literature. The simplest consists a rectangular spoke added to the convex corner so that the corner is now protected. Figure 3-4 shows an example of this kind of corner compensation.

When the etch begins, the convex corners of the structure are attacked first. As the etch progresses, portions of the structure are etched away beginning at the tip and this etch front moves toward the desired corner. Beyond this point, the corner begins to get etched away. In order for this etch front to end at the desired location, the size of the rectangle must be of the appropriate dimensions based on information about the desired etch depth and the ratio $\frac{R_{\{411\}}}{R_{\{100\}}}$ of etch rates of the $\{411\}$ planes and that of the $\{100\}$ planes, which

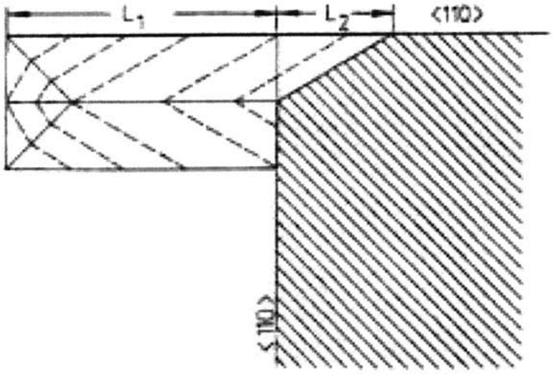

Figure 3-4: Simple rectangular compensation structure for KOH etching a convex corner. The dashed lines indicate the boundary of the surface as the etch progresses in time. Reproduced from [30].

depends on the KOH concentration. In particular, we need [30]

$$L_1 = 2H\frac{R_{\{411\}}}{R_{\{100\}}} \tag{3.5}$$

$$L_2 = \frac{B_{\langle 110\rangle}}{2\tan(30.96^\circ)} \tag{3.6}$$

$$\tag{3.7}$$

where

H : Desired etch depth, (3.8)

$B_{\langle 110\rangle}$: Width of the $\langle 110\rangle$-oriented beam, (3.9)

$\tan(30.96^\circ)$: Geometry factor. (3.10)

Although this is a very simple structure, it has a disadvantage. Because the etch front is never parallel to the boundaries that make up the convex corner, it is impossible to obtain a perfect right angle at the surface at the desired location. If the etch time is slightly short, a triangular portion of the compensating structure protrudes from the corner. If the etch time is slightly too long, the corner is partially etched away.

There are other structures that not only achieve a perfect convex corner but are also compact [44], [9]. These consist of spokes that are at 45 degrees to the convex corner boundaries. Figure 3-5 shows an example of such a structure and Figure 3-6 shows the result.

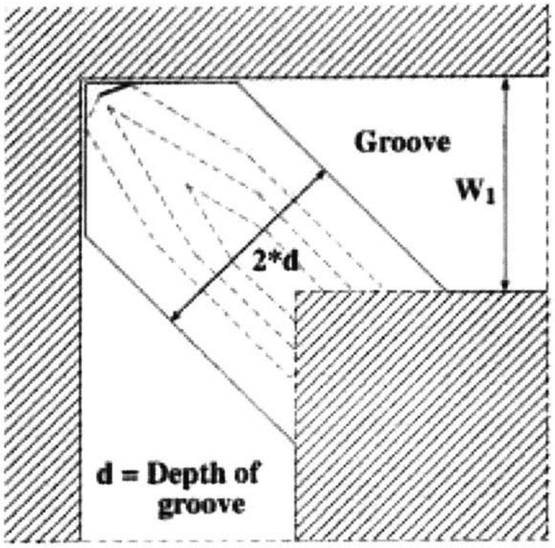

Figure 3-5: A conventional corner compensating structure that results in a perfect corner. Reproduced from [9].

The discussion on compensating structures is relevant for the capacitor of the resonator, which is in the shape of a square. However, the widths of these squares designed, which range from 2.5 mm to 8 mm, are much larger than the etch depth, which is 0.5 mm. Thus, any imperfections resulting from any compensating structure would not be large compared to the rest of the device and would not impact the device model too much. So, for the resonator process design, the simple compensating structure consisting of rectangular spokes was used.

3.5.3 Bonding area

The two dies bonded front-to-front to form devices only touch at the margin around the rim of the inductor. This rim is 2.5 mm wide so that a 25 mm wide die would have a total

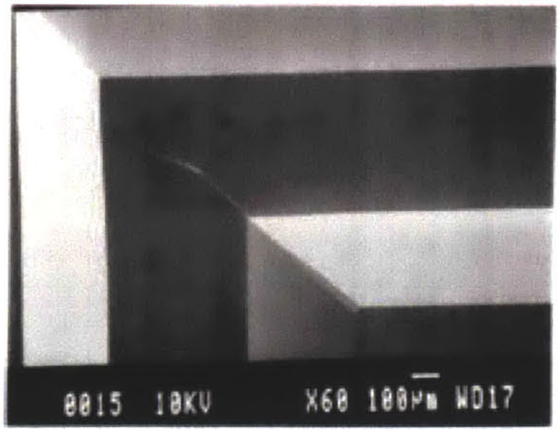

Figure 3-6: SEM photo of the result of a conventional corner compensating structure. Note that the desired corner is achieved. Reproduced from [9].

bond area of approximately 250 mm^2. To produce 0.5 MPa of pressure, a 12 kg mass would be placed on top of the wafers, which is a reasonable amount to apply without the aid of machines. A narrower bonding area would reduce the margin of error in die sawing and a wider bonding area would require more weight to be applied during the bonding process, so 2.5 mm is a good compromise.

3.5.4 Mask alignment

There are three steps in the process flow that require mask alignment, and all for different reasons: Step 4 (frontside photolithography), Step 7 (backside photolithography) and Step 10 (RIE etch nitride to expose capacitor plateau).

KOH-etching (100) silicon produces rectangular features parallel to the wafer flat. Thus, when the frontside of the wafer is patterned in Step 4, it is important that the mask features are aligned correctly. A slight tilt would result in features that are larger than the intended sizes. As can be seen in Appendix E beginning on Page 129, all masks have horizontal bars near the bottom with which the wafer flat can be aligned with the aid of optical instruments.

The second alignment is in Step 7, when photolithography is done on the backside of the wafer after being applied to the frontside. The backside processing produces the slits

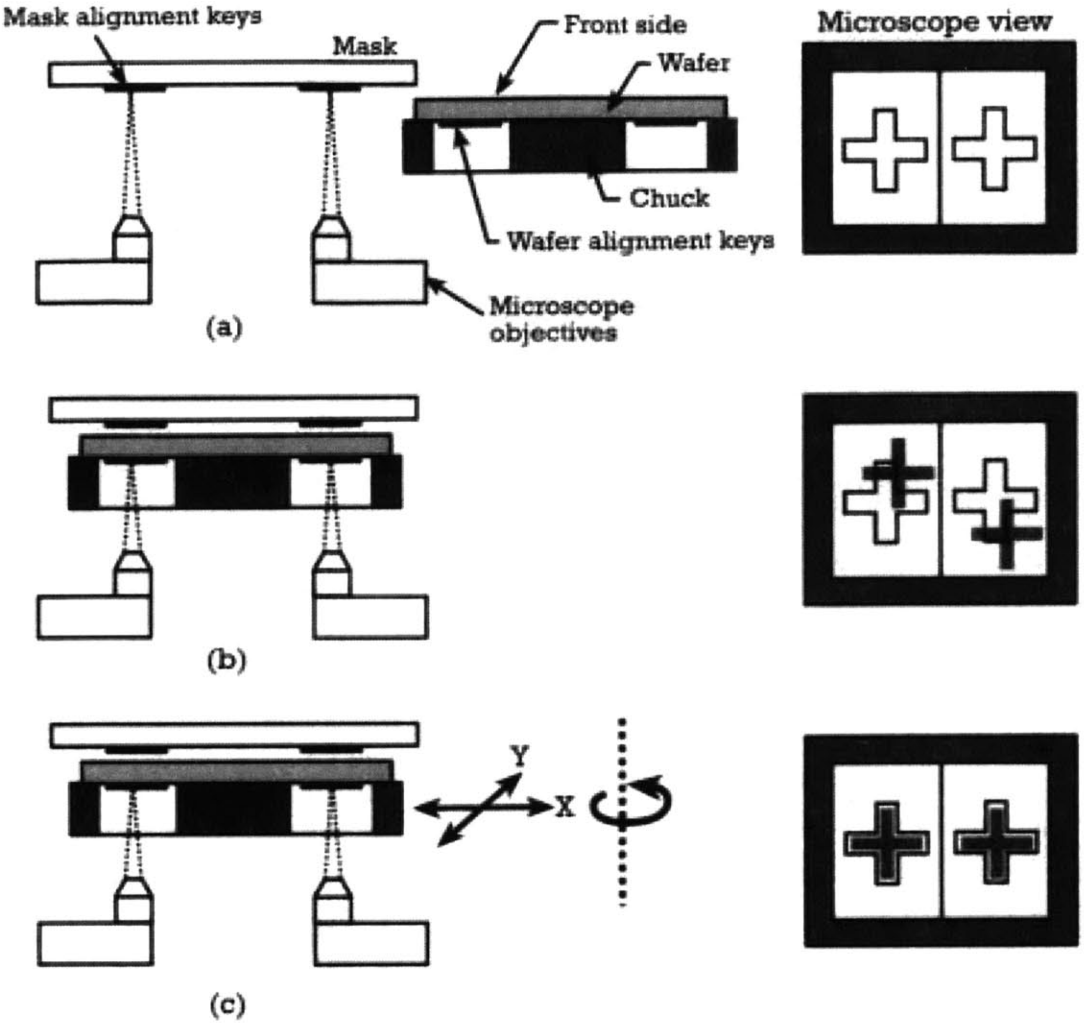

Figure 3-7: Two-sided alignment mechanism. The diagrams on the left-hand side show the side view of the mask, wafer, chuck and optical system, and the diagrams on the right-hand side show the view on the computer monitor. (a) The image of the mask alignment marks is read and projected on the computer monitor. (b) The alignment marks on the bottomside of the wafer are also projected on the monitor. (c) The position of the wafer is adjusted by translation and rotation until the two images match acceptably well. Reproduced from [23]

in the inductor wall for the wire loop, so precise alignment is critical. Figure 3-7 shows the alignment mechanism using EV1 in MTL TRL.

All masks have alignment marks placed at identical locations. When the backside mask is placed in EV1, the optical sensors are focused on those marks, which are locked onto the computer monitor. The marks from the frontside mask have been marked into the frontside of the wafers. The wafer is placed face down into the chuck, and an image of the wafer marks are superimposed on the computer monitor. The position of the wafer is then adjusted so that they match.

The alignment marks used in the masks for the resonator consist of vertically centered half-crosses on the left and right sides of the wafers. In the center of a cross, there is a much smaller cross. Thus, once alignment is reasonably good a viewed with the large crosses, the view is zoomed in to the small crosses so that the wafer position can be fine tuned.

Finally, the third time mask alignment is used in Step 10 when nitride is removed from the capacitor plateau using RIE. In this case, another wafer is used as a mask. As described earlier, this wafer consists of square holes. When placed over the other wafers, the capacitor plateau is exposed and the rest of the top surface is not. It is acceptable for the inductor cavity to lie exposed since an RIE etch programmed to remove 0.1 μ of nitride would remove even less bare silicon. Thus, to maximize alignment flexibility, the size of the square hole is halfway between that of the capacitor plateau and the inductor cavity. The safety margin is large enough so that alignment can be done by hand and unaided eye.

3.6 Summary

We discussed wafer etching and silicon structure. HF-etching Pyrex did not produce a sufficiently smooth surface for a continuous metal layer to be deposited, and thus we used KOH to etch (100) silicon anisotropically as the main fabrication technology. The device process flow and mask design were provided. The capacitor gap was created by a second KOH etch after the main inductor cavity was formed as the other option, RIE, would produce a non-continuous surface. The choice of KOH required corner compensation structures to be incorporated into the mask design, though the feature sizes did not unequivocally demand that the structures be perfect. KOH requires that wafers be aligned properly against the wafer flat. Perfect mask alignment for the capacitor gap etch was not as critical.

Chapter 4

Fabrication Measurements

This chapter contains the results of fabrication experiments, including tests with corner compensation, measurements of the conducting gold layer, pictures of gold coverage over sidewalls, and measurements of the conductivity of gold over the sidewalls. An experimental wafer was etched in KOH to produce characteristic trenches and gold was deposited. Tests were done to determine whether the gold layer was acceptable for use in the resonator. The wafer passed all the critical tests: the gold was sufficiently thick, and both visual and electrical tests confirmed that the gold forms a conducting layer across the trench.

4.1 Experimental Mask

The mask in Figure E-4 in Appendix E on Page 133 was applied to a single wafer to create KOH-etched cavities. After gold was sputtered, all the aforementioned experiments were performed on this wafer. The top of the mask contains rectangles of different widths, which produces KOH-etched trenches, some of which are self-terminating. The middle horizontal third of the mask contains cavities that have convex corners with compensation structures of various sizes. There is a solid thick horizontal stripe across the mask so that after the wafer is etched, it can be cleaved easily into two parts. The lower part of the wafer contains rectangles large enough so that the etch reaches the other side and creates rectangular through-holes. These holes are used as shadow masks. Then, the lower part of the wafer is placed over the upper part of the wafer as a mask and chromium and gold are sputtered. The result is strips of gold over a series of trenches.

The circles on the lower part of the mask are present to demonstrate that the final resulting features will always be rectangular regardless of the starting shape. This is in fact confirmed.

4.2 Corner Compensation

As described in the previous section, the middle horizontal third of the experimental mask contains square cavities that have convex corners with compensation structures of various sizes. All the cavities are 8 mm wide and are implementations of the simple rectangular structures shown in Figure 3-4 on Page 58. As explained in at the end of Subsection 3.5.2 on Page 59, well-designed corner compensation structures are not necessary. Thus, the experiments simply served to demonstrate the effect of convex corners being cut off and to confirm that the resulting (possibly imperfect) corners can be covered with a continuous layer of gold.

Figure 4-1 shows photograph of a corner compensation experiment; four cavities are shown. The upper photograph is the wafer just prior to KOH-etching; the blue regions make up the silicon nitride mask and the white regions are silicon. The lower photograph is the same part of the wafer after KOH-etching and gold deposition. The leftmost cavity has long compensation structures, and much of these remain. The second and fourth cavities have no compensation structures and so the corners are cut in the same manner as shown in Figure 3-3 on Page 57. The third cavity from the left has smaller structures than the first, and the results are closer to the desired shape; only small triangular protrusions remain.

Figure 4-2 is similar to Figure 4-1, but the photographs were taken for another part of the wafer. The center squares are smaller than those in the previous figure. Note that the center square in the leftmost cavity, which has no compensation structures, is completely etched away. The second and fourth cavities have significant amounts of compensation left, as the original structures are quite long. The third cavity from the left has no structures, and the corners are significantly truncated.

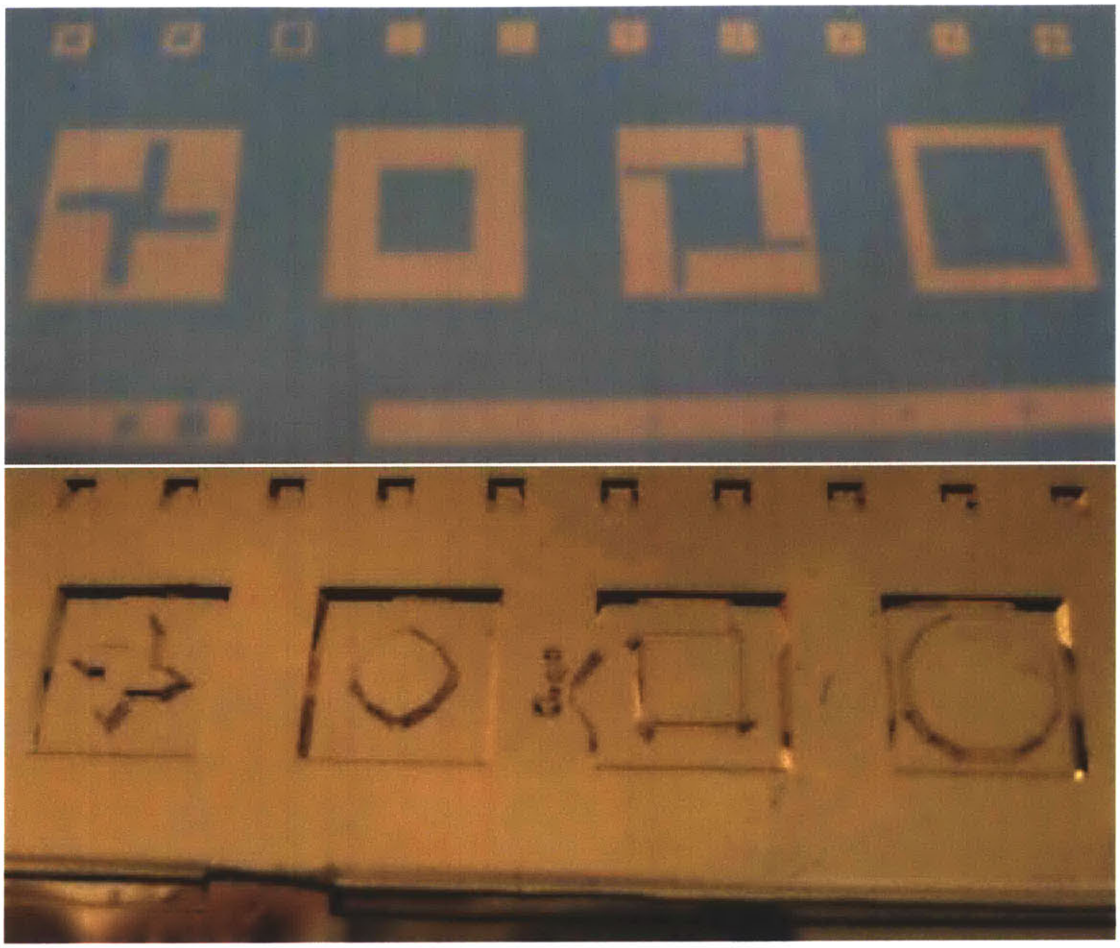

Figure 4-1: Corner compensation experiment (I). (Upper) Nitride mask. (Lower) Resulting gold-lined etched cavities.

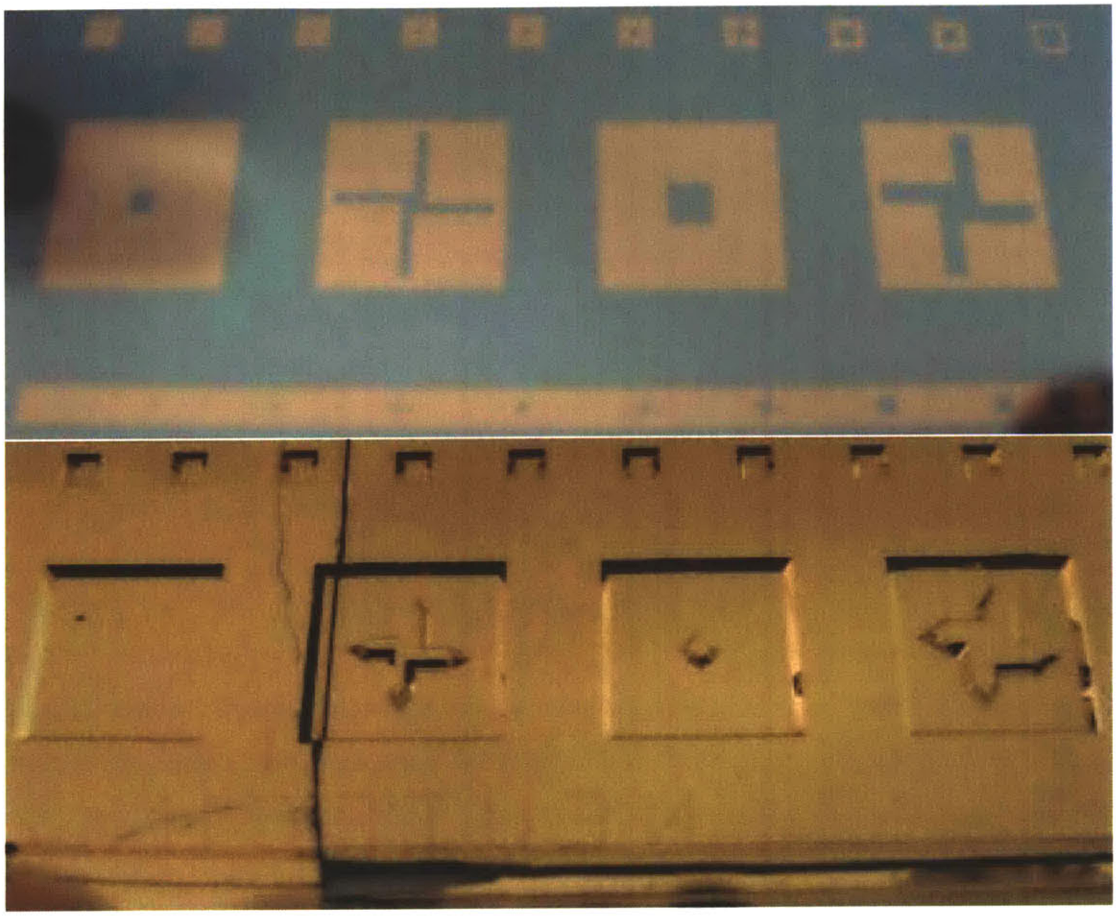

Figure 4-2: Corner compensation experiment (II). (Upper) Nitride mask. (Lower) Resulting gold-lined etched cavities.

4.3 Gold Thickness

To determine whether the gold deposition rate in the EML sputterer is around 1 μm per hour, gold is deposited as strips using a wafer as a mask on separate wafers for 50 minutes and for two hours. The depths of the silicon and gold are then measured using the EML Dektak. Figure 4-3 shows the results of these measurements. In both cases, the transition between a full gold layer and bare silicon is less than 100 μm wide, which is narrow. Furthermore, the deposition rate is approximately constant, so the process is reliable for producing the conducting layer.

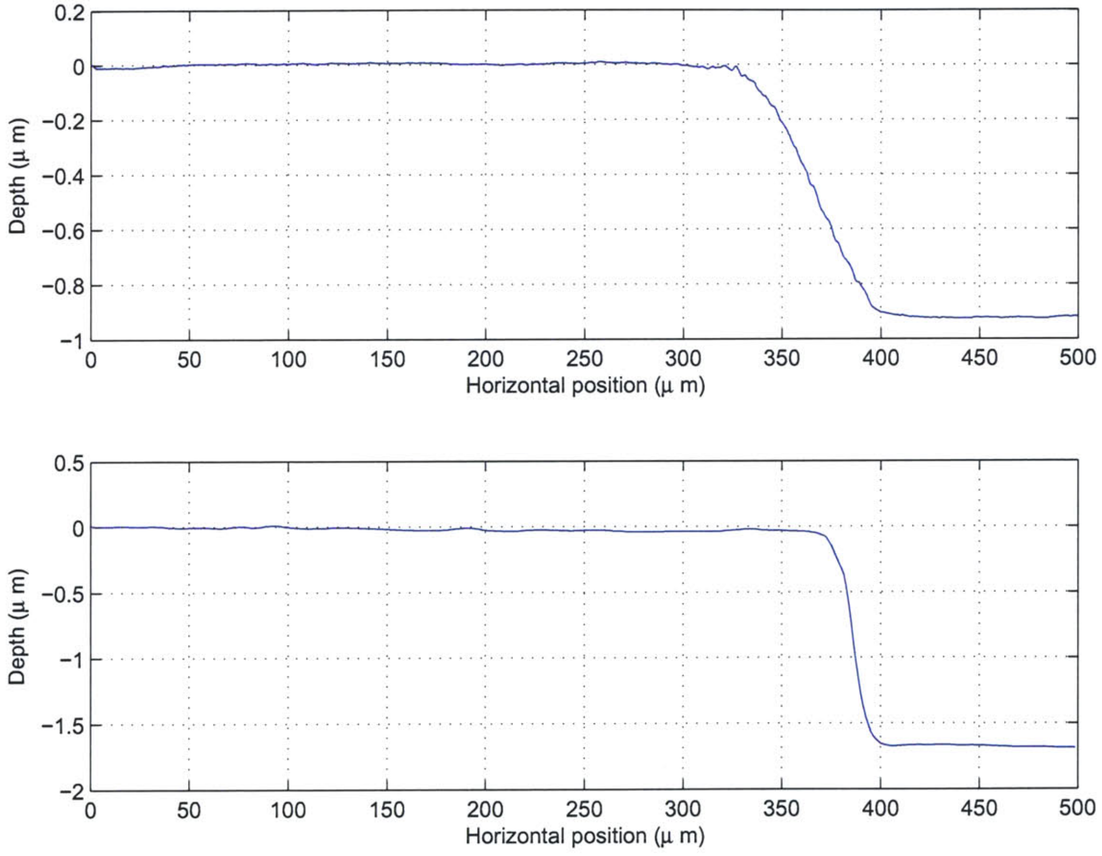

Figure 4-3: Dektak measurement of gold thickness. The left side of the graph is the depth of the top of the gold layer and the the right side is the depth of the top of the bare silicon wafer. The upper plot is for a 50-minute sputter and the lower plot is for a two-hour sputter.

4.4 Gold Coverage Over Sidewalls

4.4.1 Microscope photographs

Figure 4-4 shows a photograph of KOH-etched convex corner after gold deposition as seen from a microscope. The white regions are the surfaces parallel to the wafer face. They appear white because light from the microscope is reflected directly from those regions into the lens. The sloped side walls, on the other hand, appear gray because light is reflected away from the microscope aperture.

In Figure 4-5, the wafer is tilted so that the side wall is normal to the microscope line of side. Thus, the side wall now appears white and the other surfaces appear dark gray. Upon visual inspection, we note that the surface is smooth. There are some thick dark lines, which are steps in the surface. These result from imperfect wafer alignment with the mask. Fortunately, these are vertical in orientation and thus should not too adversely affect the conductivity of the gold layer from the top of the trench to the bottom.

Figure 4-4: Microscope photograph of KOH-etched convex corner after gold deposition.

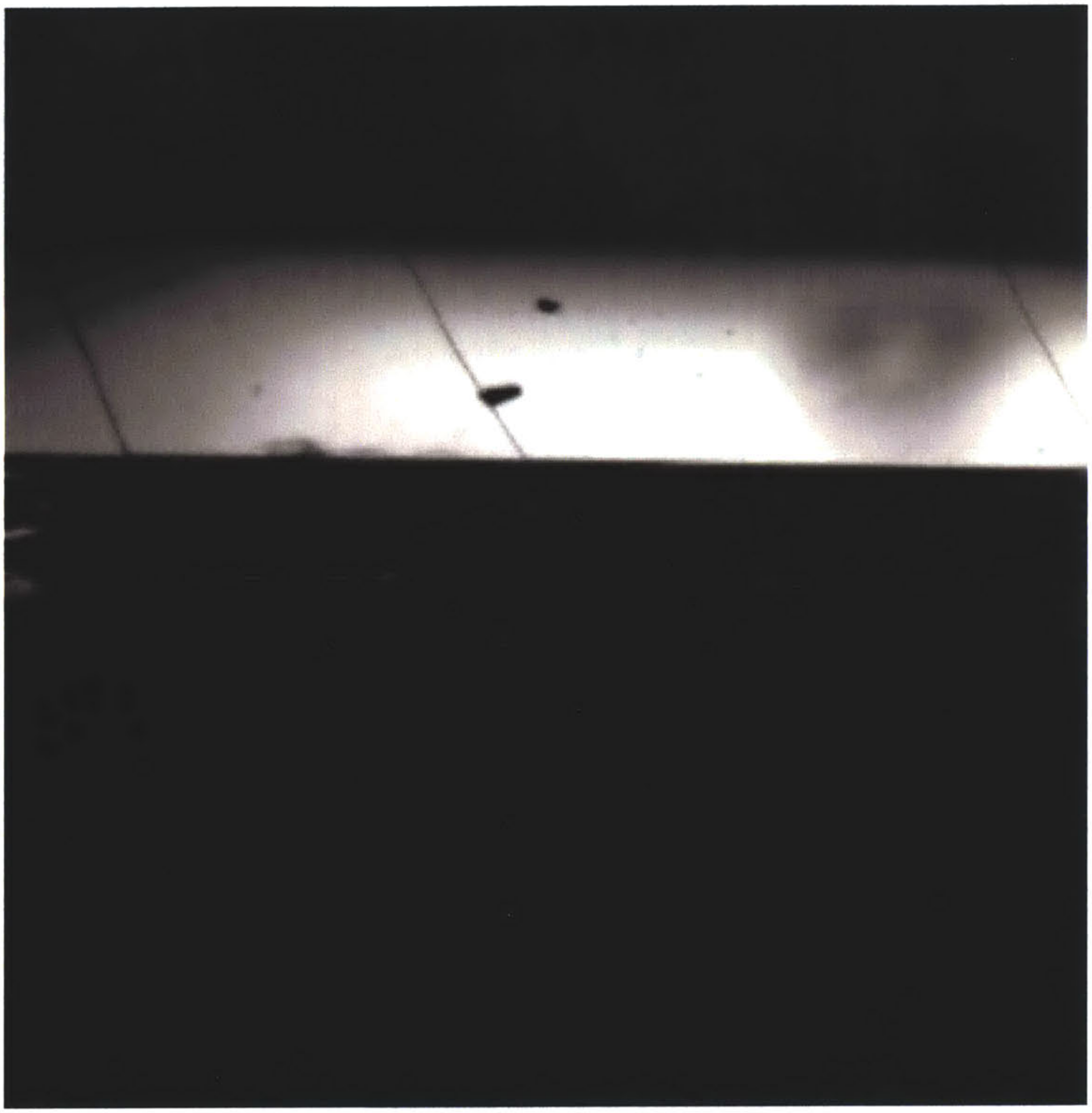

Figure 4-5: Microscope photograph of KOH-etched side walls after gold deposition.

4.4.2 SEM images

The wafer was placed in a scanning electron microscope (SEM)[1] to examine the etch surface more closely. Figure 4-6 shows an SEM image of a the edge of a KOH-etched trench without gold; the width of the trench is approximately 200 μm. At this resolution, the walls appear smooth. There is a noticeable piece of debris at the bottom.

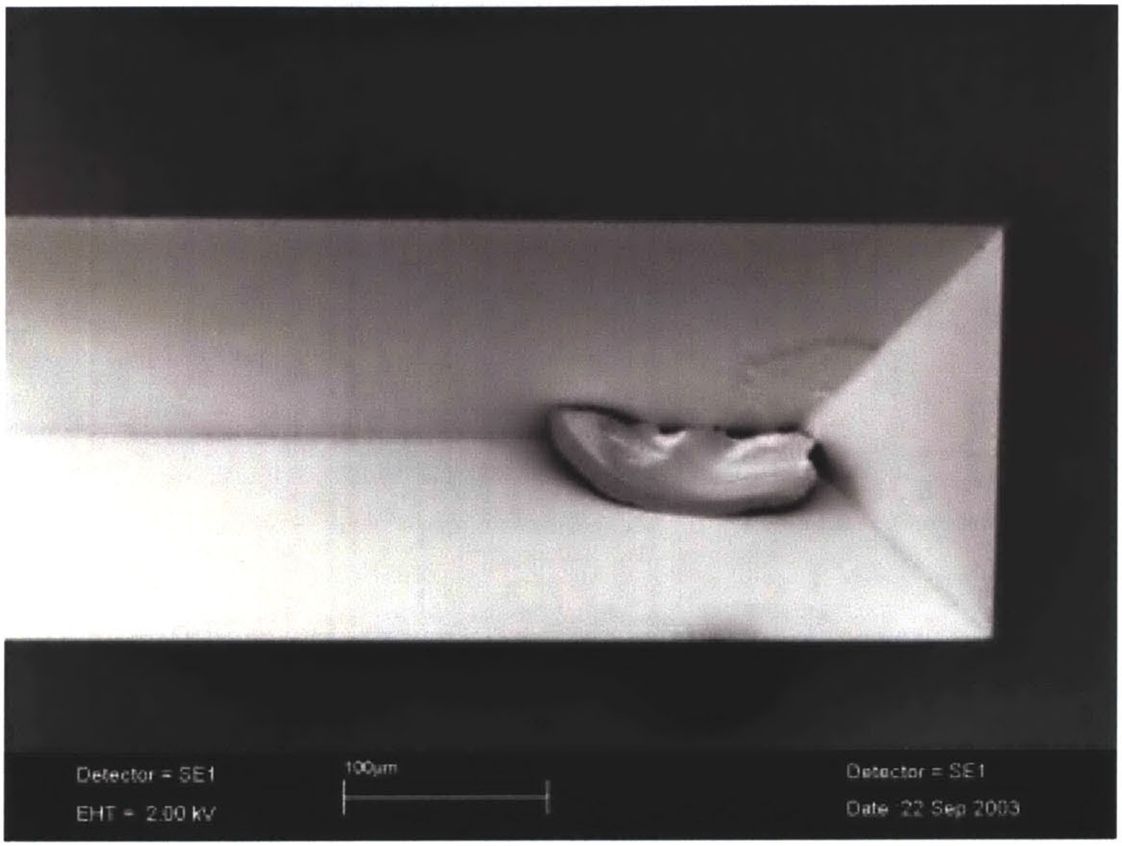

Figure 4-6: SEM image of the edge of a KOH-etched trench without gold.

---

[1] Located in MIT room 4-141.

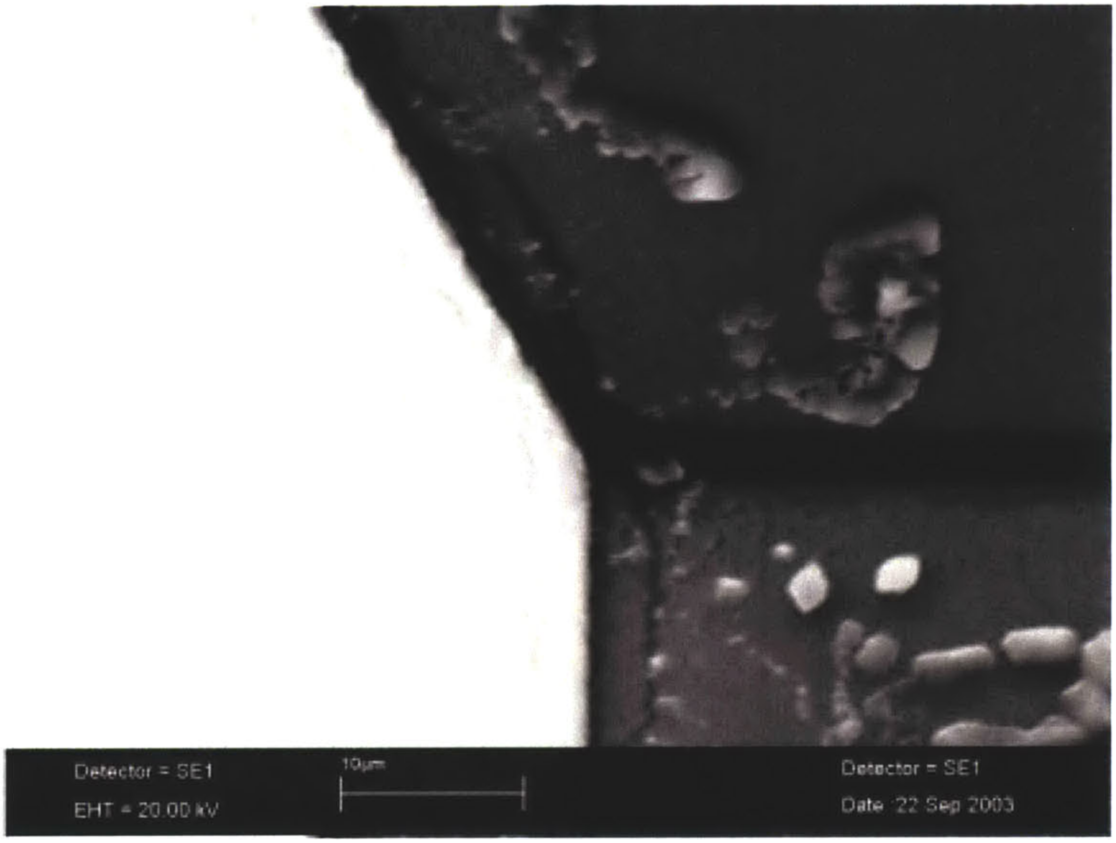

Figure 4-7: SEM image of the intersection of two sidewalls and the bottom surface of a KOH-etched trench.

Figure 4-7 shows an SEM image of the intersection of two sidewalls and the bottom surface of a KOH-etched trench without gold at high resolution. The walls are smooth and the junction is sharp, but there is debris in that region.

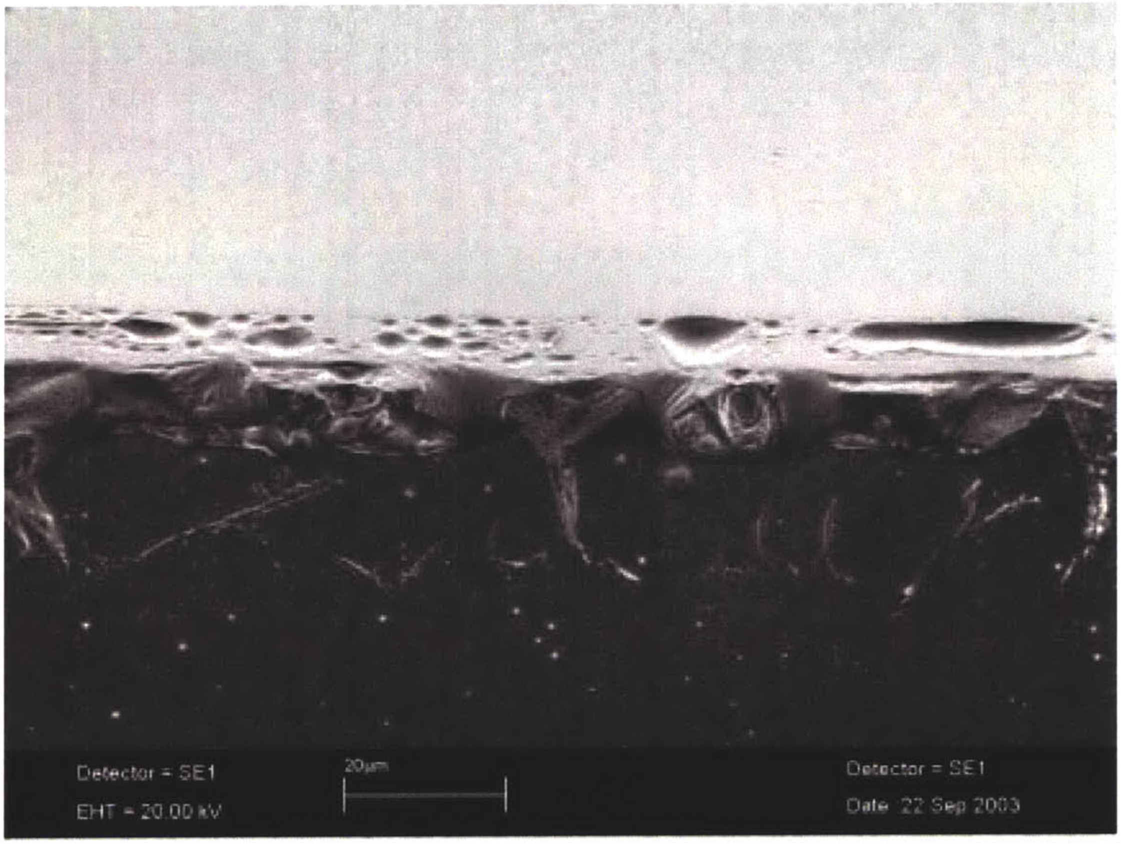

Figure 4-8: SEM image of the bottom edge of a gold-covered KOH-etched trench.

Figure 4-8 shows an SEM image of the bottom edge of a gold-covered KOH-etched trench. The light-colored upper half is the sidewall and the dark-colored lower half is the bottom trench surface. Note that there are some irregularities at the edge.

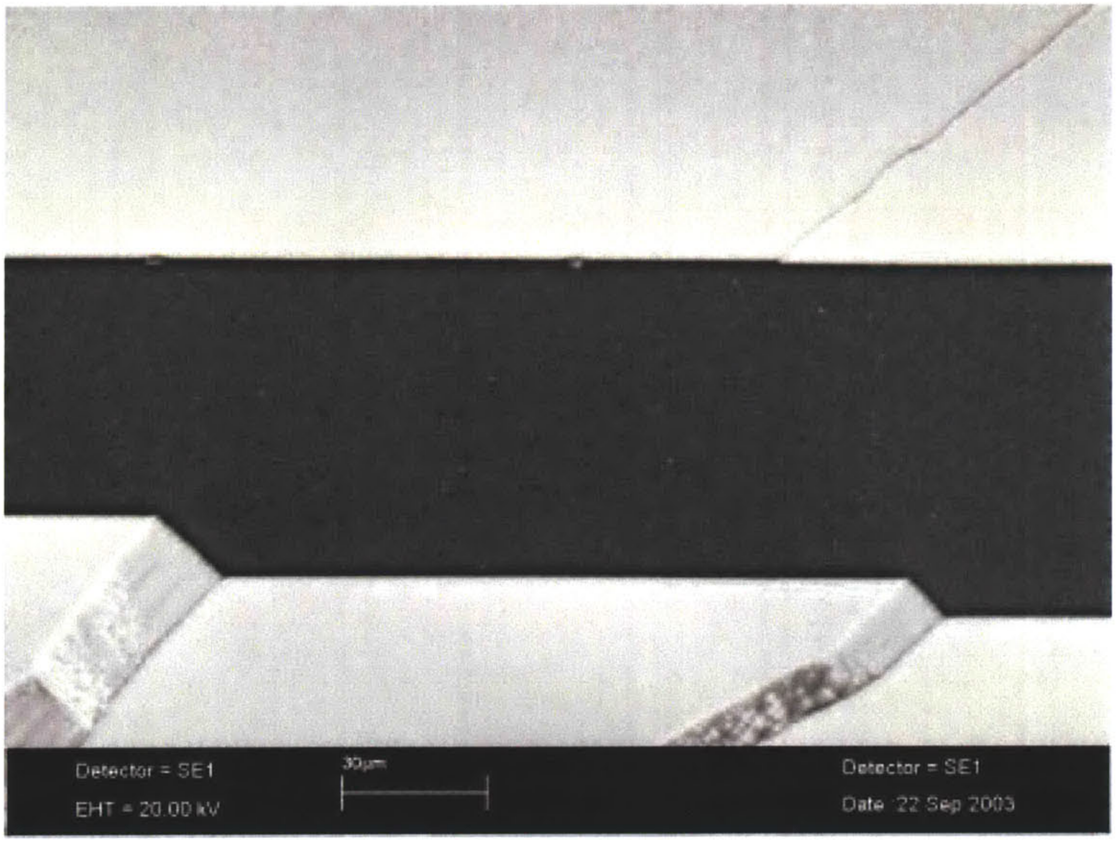

Figure 4-9: SEM image of the bottom of a gold-covered KOH-etched trench with non-uniform sidewalls.

Figure 4-9 shows an SEM image of the bottom of a gold-covered KOH-etched trench with non-uniform sidewalls. The light upper and lower thirds are opposing sidewalls and the middle third is the bottom trench surface. Note that the sidewall is not straight, but has a jagged surface. This is a result of the mask not being perfectly aligned with wafer flat. With perfect alignment, silicon planes come off in slices as KOH etches away. However, when the walls are not parallel to the crystal planes, some parts of a particular plane are removed earlier than other parts of the same plane, which produces the profile shown above.

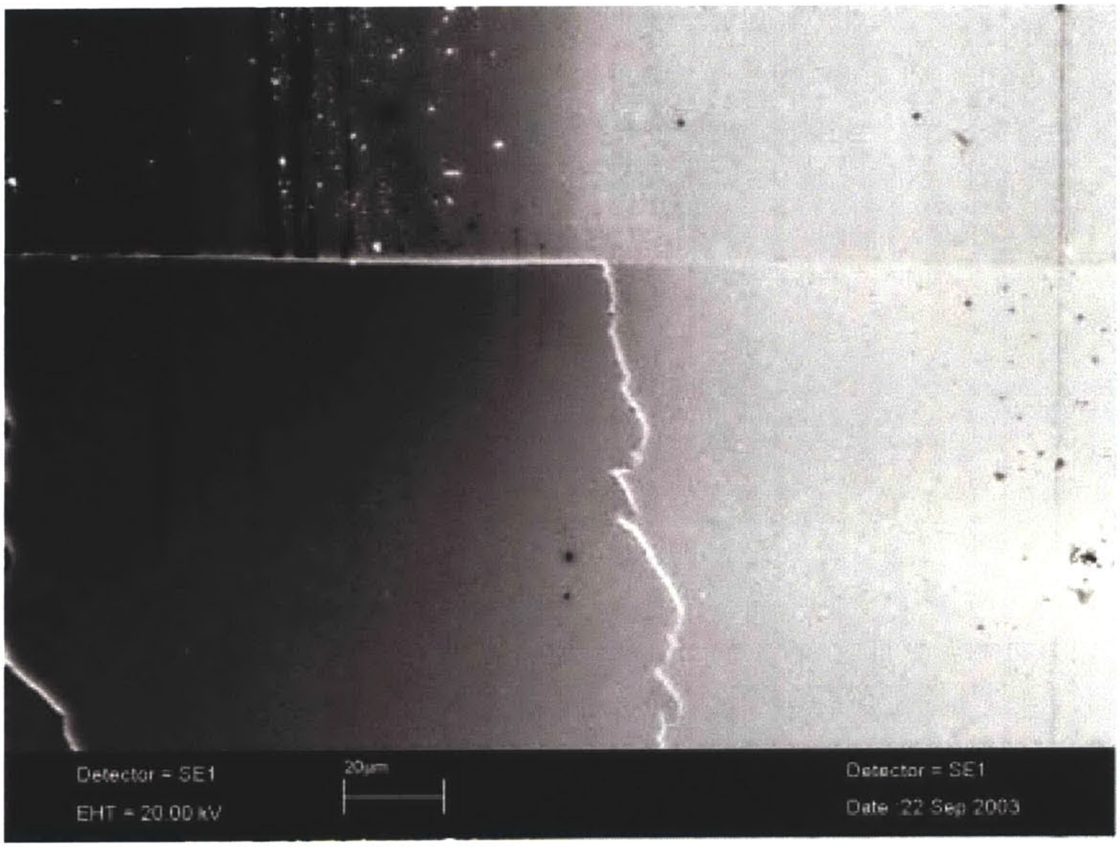

Figure 4-10: SEM image of the a gold strip edge cutting across a KOH-etched trench edge.

Figure 4-10 shows an SEM image of the a gold strip edge cutting across a KOH-etched trench edge. The upper half is the top surface of the wafer, and the lower half is a sidewall. The left half is silicon that was blocked from gold deposition, and the right right is a gold strip deposited on silicon. The Si-Au boundary is visually sharp, given the resolution of the image.

4.4.3 EDX scans

After SEM images were taken, an analysis of the composition of the surfaces at various locations is done using an energy-dispersive X-ray (EDX) system, which uses X-rays emitted from the sample and correlates the emission energies to elemental composition. The electron beam excites the specimen, and X-rays are emitted as the states decay. These measurements were taken with the help of A. John Hart and Jaime Werkmeister. There are a number of finer points – separating combination peaks, resolution, and spot size – that we didn't pay attention to and as a result the quantitative data is not completely reliable. However, in terms of relative compositions of gold and silicon, our results are reasonably accurate.

In Figures 4-11, 4-12 and 4-13, the plots are the measured intensities of Si and Au as functions of distance along some path. Figure 4-13 shows the EDX scan is across the edge of a gold strip on a sidewall of a KOH-etched trench. We see clearly that as we move to the right, the amount of gold on the wafer surface increases and the amount of silicon decreases. Figure 4-11 shows the same thing, but on the top wafer surface instead of the sidewall. The result is similar. Figure 4-12 shows the scan across a top surface-sidewall trench. Although the data is noisy, there is no clear difference in the Si-Au composition across the trench, as expected.

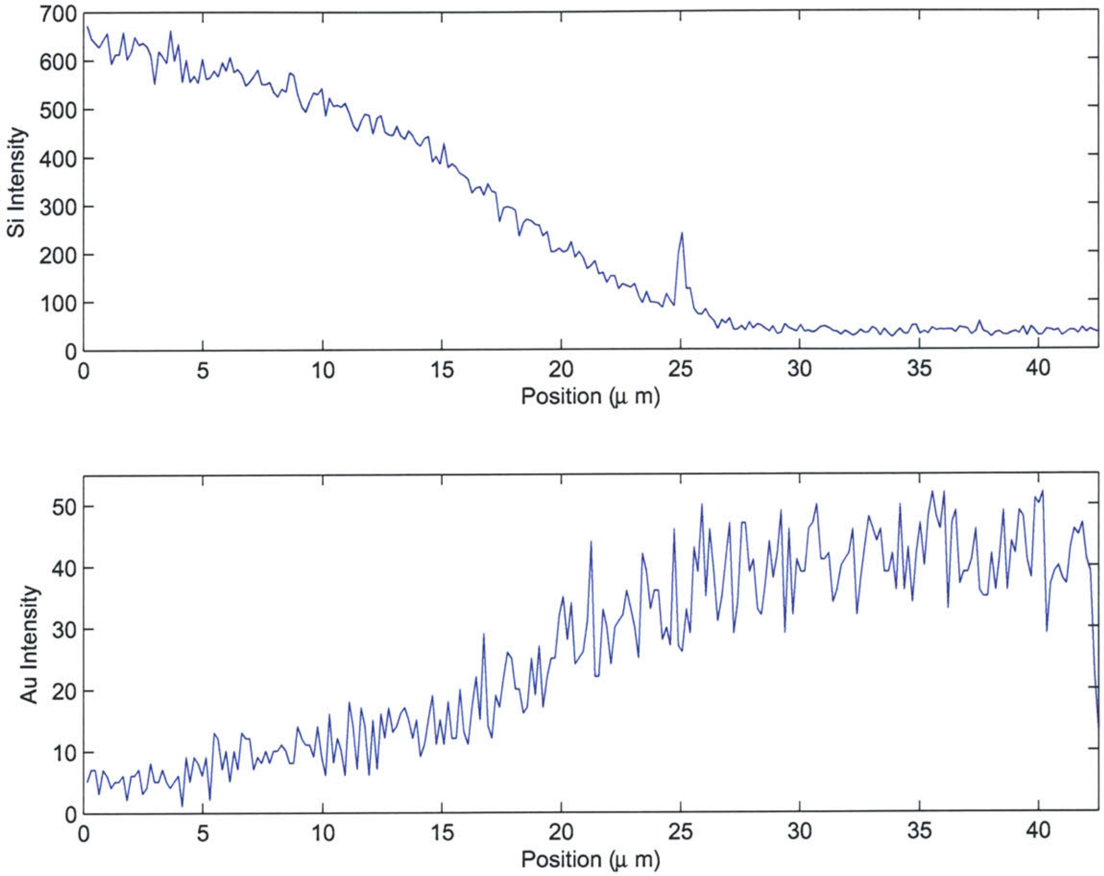

Figure 4-11: EDX scan of Si-Au composition across the gold strip edge on a sidewall of a KOH-etched trench.

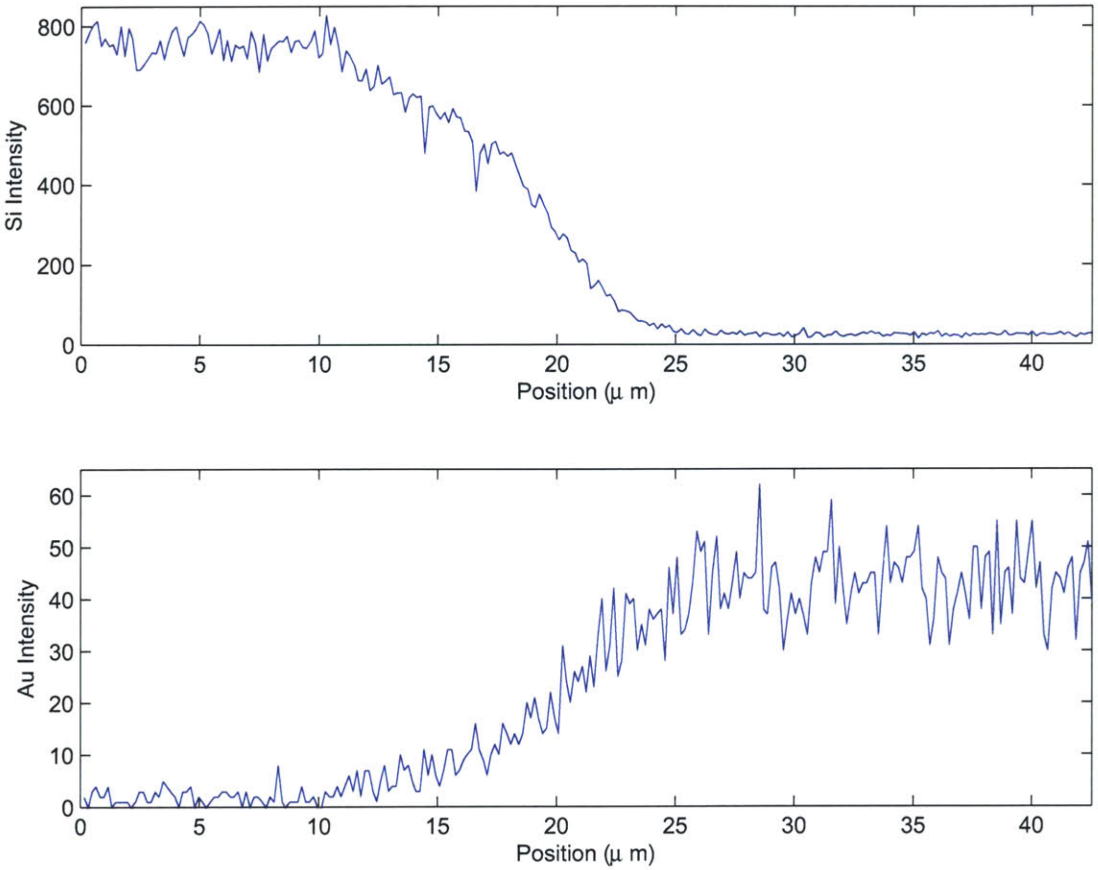

Figure 4-12: EDX scan of Si-Au composition across the gold strip edge on the top wafer surface.

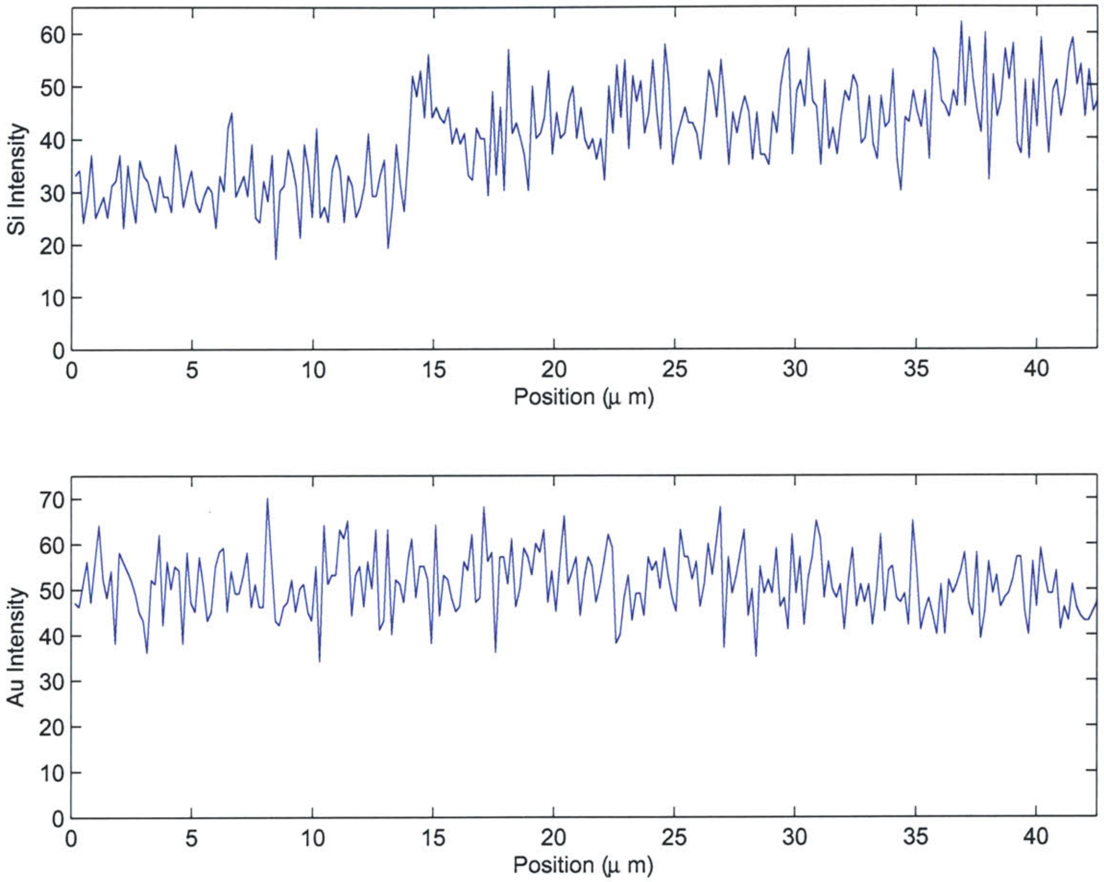

Figure 4-13: EDX scan of Si-Au composition of a gold strip across a top surface-sidewall edge of a KOH-etched trench.

4.4.4 Spectral analysis

Along with EDX scans, spectral analysis of the elemental composition of the gold strip on the wafer surface at various locations is performed. Figure 4-14 shows this analysis at a gold location. As expected, gold is the element with the highest detection intensity. Similarly, Figure 4-15 shows this analysis at a silicon location with silicon as the most abundant element detected. Figure 4-16 shows this analysis at a Si-Au junction on the sidewall, which resulted in silicon and gold being detected in roughly equal amounts.

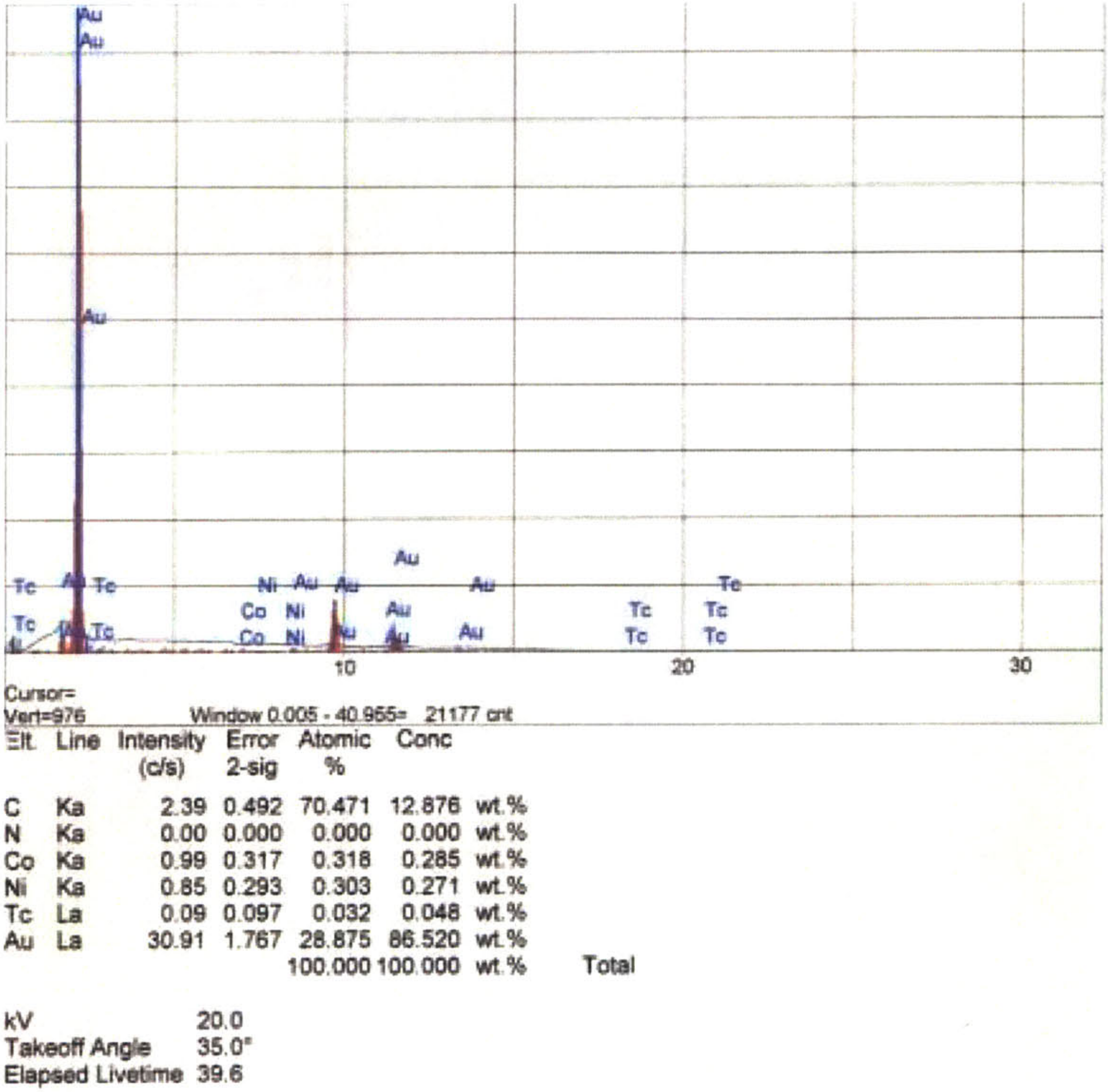

Cursor=
Vert=976 Window 0.005 - 40.955= 21177 cnt

Elt.	Line	Intensity (c/s)	Error 2-sig	Atomic %	Conc		
C	Ka	2.39	0.492	70.471	12.876	wt.%	
N	Ka	0.00	0.000	0.000	0.000	wt.%	
Co	Ka	0.99	0.317	0.318	0.285	wt.%	
Ni	Ka	0.85	0.293	0.303	0.271	wt.%	
Tc	La	0.09	0.097	0.032	0.048	wt.%	
Au	La	30.91	1.767	28.875	86.520	wt.%	
				100.000	100.000	wt.%	Total

kV	20.0
Takeoff Angle	35.0°
Elapsed Livetime	39.6

Figure 4-14: Spectral analysis of the elemental composition of the gold section of a gold strip on the wafer surface.

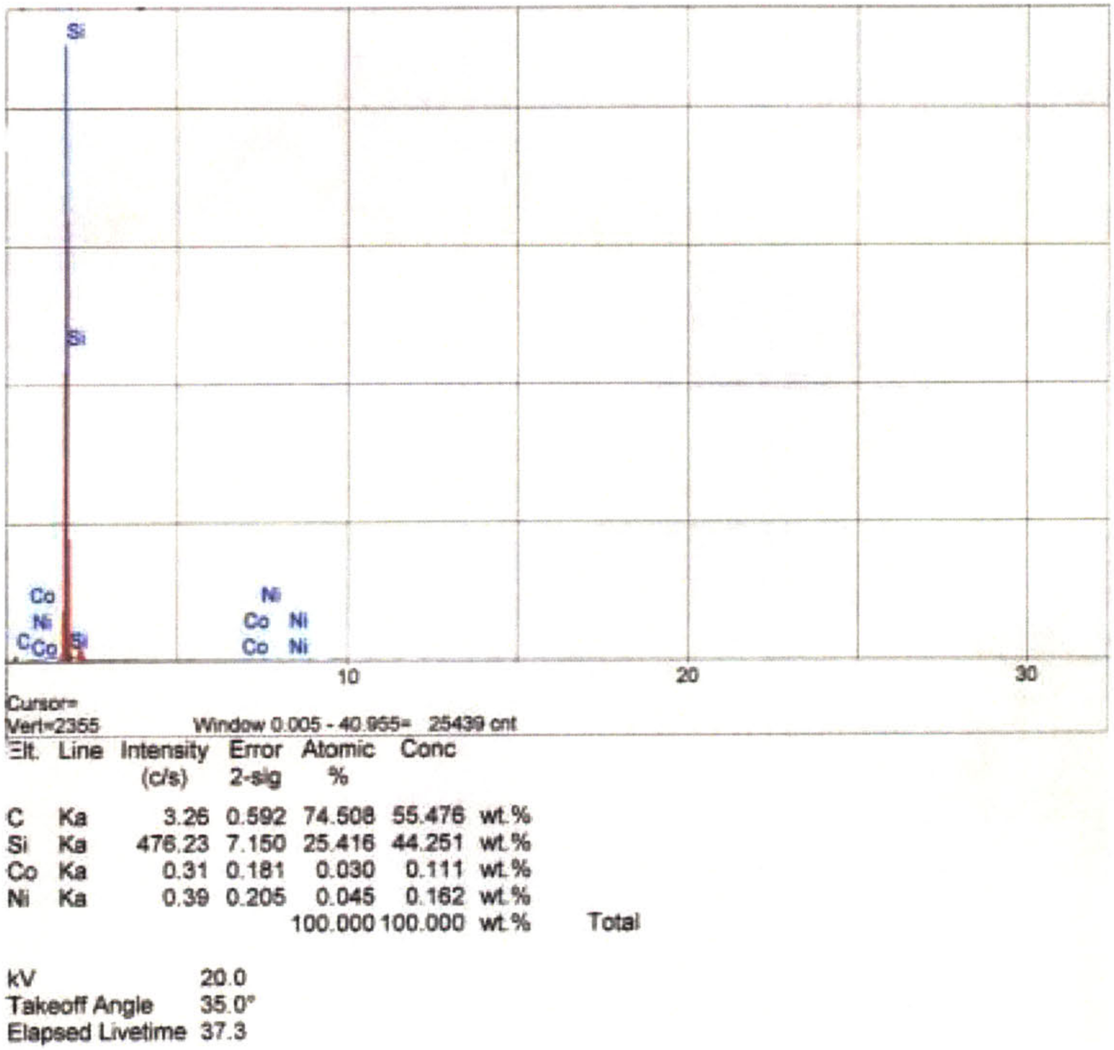

```
Cursor=
Vert=2355          Window 0.005 - 40.955=   25439 cnt
Elt. Line Intensity Error  Atomic  Conc
           (c/s)    2-sig    %

C    Ka      3.26  0.592  74.508  55.476  wt.%
Si   Ka    476.23  7.150  25.416  44.251  wt.%
Co   Ka      0.31  0.181   0.030   0.111  wt.%
Ni   Ka      0.39  0.205   0.045   0.162  wt.%
                         100.000 100.000  wt.%      Total

kV                 20.0
Takeoff Angle      35.0°
Elapsed Livetime   37.3
```

Figure 4-15: Spectral analysis of the elemental composition of the bare silicon section of the wafer surface.

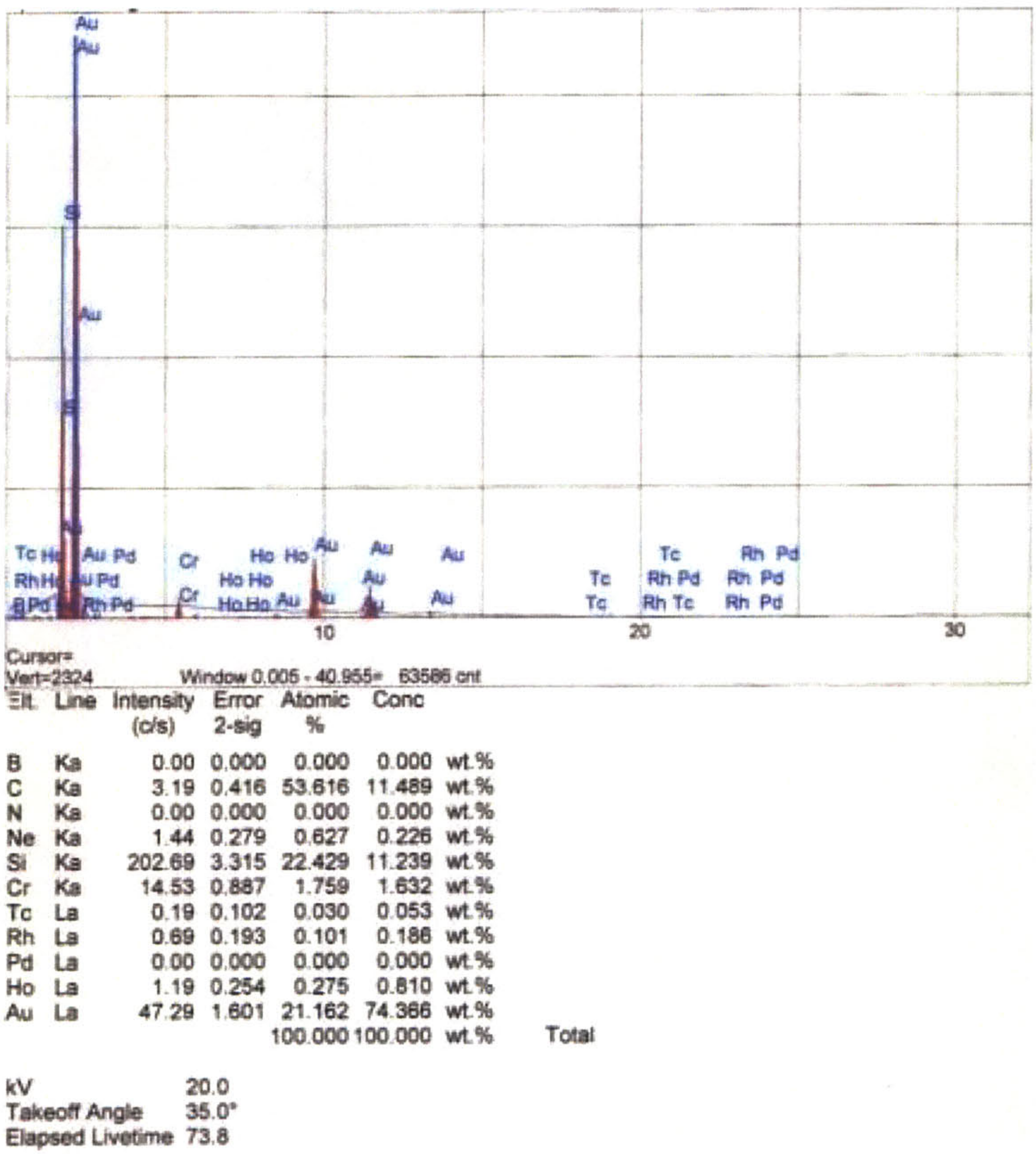

```
Cursor=
Vert=2324          Window 0.005 - 40.955=   63586 cnt
Elt. Line Intensity Error  Atomic  Conc
          (c/s)     2-sig  %

B    Ka     0.00  0.000   0.000   0.000 wt.%
C    Ka     3.19  0.416  53.616  11.489 wt.%
N    Ka     0.00  0.000   0.000   0.000 wt.%
Ne   Ka     1.44  0.279   0.627   0.226 wt.%
Si   Ka   202.69  3.315  22.429  11.239 wt.%
Cr   Ka    14.53  0.887   1.759   1.632 wt.%
Tc   La     0.19  0.102   0.030   0.053 wt.%
Rh   La     0.69  0.193   0.101   0.186 wt.%
Pd   La     0.00  0.000   0.000   0.000 wt.%
Ho   La     1.19  0.254   0.275   0.810 wt.%
Au   La    47.29  1.601  21.162  74.366 wt.%
                        100.000 100.000 wt.%      Total

kV                20.0
Takeoff Angle     35.0°
Elapsed Livetime  73.8
```

Figure 4-16: Spectral analysis of the elemental composition of the silicon-gold junction on the sidewall of a KOH-etched trench.

4.5 Electrical Conductivity Over Sidewalls

The most critical step in determining the viability of KOH-etched silicon as the substrate for the resonator is to measure the electrical conductivity of metal deposited over the sidewalls of etched silicon. To test this, 1-mm wide strips of 0.2 μm thick layer of chromium bonding layer followed by a 1 μm thick layer of gold are sputtered onto a series of five trenches that are approximately 500 μm deep. The upper part of Figure 4-3 in Section 4.3 on Page 67 confirms the thickness of the gold layer.[2] The five trenches are 16000 μm, 800 μm, 400 μm, 200 μm and 100 μm wide. The four smallest trenches are self-terminating, and thus have V-shaped profiles. The largest trench is not self-terminating and has the same depth as the 800-μm wide trench. Visual inspection suggests that the gold layer is continuous. A current of 0.5 A is applied across the strip and a four-point probe test is performed at various points along the gold strip. One point near the largest trench is the reference point for the voltage difference, and voltage is measured at 18 locations along a gold strip. Figure 4-17 shows a diagram of this test across the largest trench. Figure 4-18 is a profile of the trench that was examined.

The length of the strip between the probes is calculated from the known geometric structure of the trenches. From these measurements and the resistivity of gold, which is [18]

$$\rho_{\mathrm{Au}} \quad = \quad 2.2 \times 10^{-8}\,\Omega \cdot \mathrm{m}, \tag{4.1}$$

the theoretical voltage is calculated. The plot of measured and theoretical voltages against the distance along the strip is shown in Figure 4-19. Section F.1 beginning on Page 135 contains the MATLAB code that performed the calculations and produced Figure 4-19. The theoretical curve (green squares) is about half that of the measured one (blue stars), so the theoretical one is scaled by 1.8 (red triangles) for easy comparison. The black vertical lines and circles represent the edges between the flat region on top and the trenches. For both the measured and the theoretical curves, voltage in the trenches rises faster than it

---

[2] Since the chromium layer is five times thinner than the gold layer and has a resistivity that is six times greater, gold is the dominant component of the overall resistance, which is the inverse sum from the individual components. Thus, the contribution from chromium can be ignored.

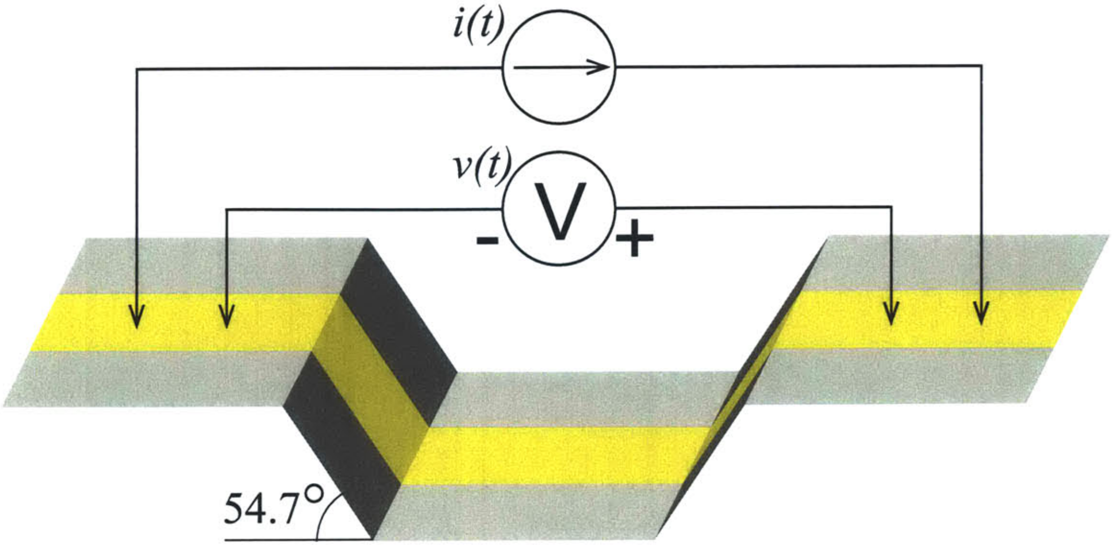

Figure 4-17: Diagram of four-point probe test of gold strip conductivity on KOH-etched trenches.

does on the surface of the wafer. Our model takes into account a thinner gold coverage on the trench walls due to non-perpendicular gold deposition (hence higher resistance).

There are no unexpectedly large rises in resistance in the trench, so there is probably adequate gold coverage on the angled edges. We confirmed the thickness of the gold, so the need to scale by 1.8 indicates that the grains are discontinuous. Fortunately, 1.8 is a small enough factor so that a high-Q resonator can be constructed.

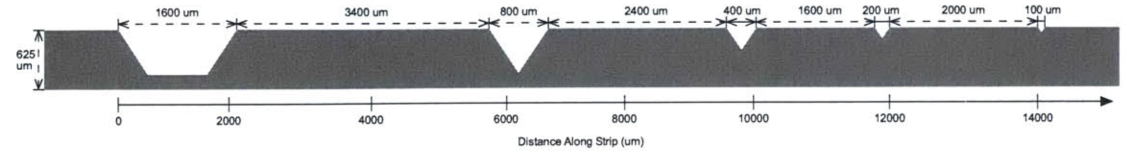

Figure 4-18: Profile of KOH-etched trenches for gold conductivity test. Note that the axis "distance along strip" takes into account additional length due to the sloped walls.

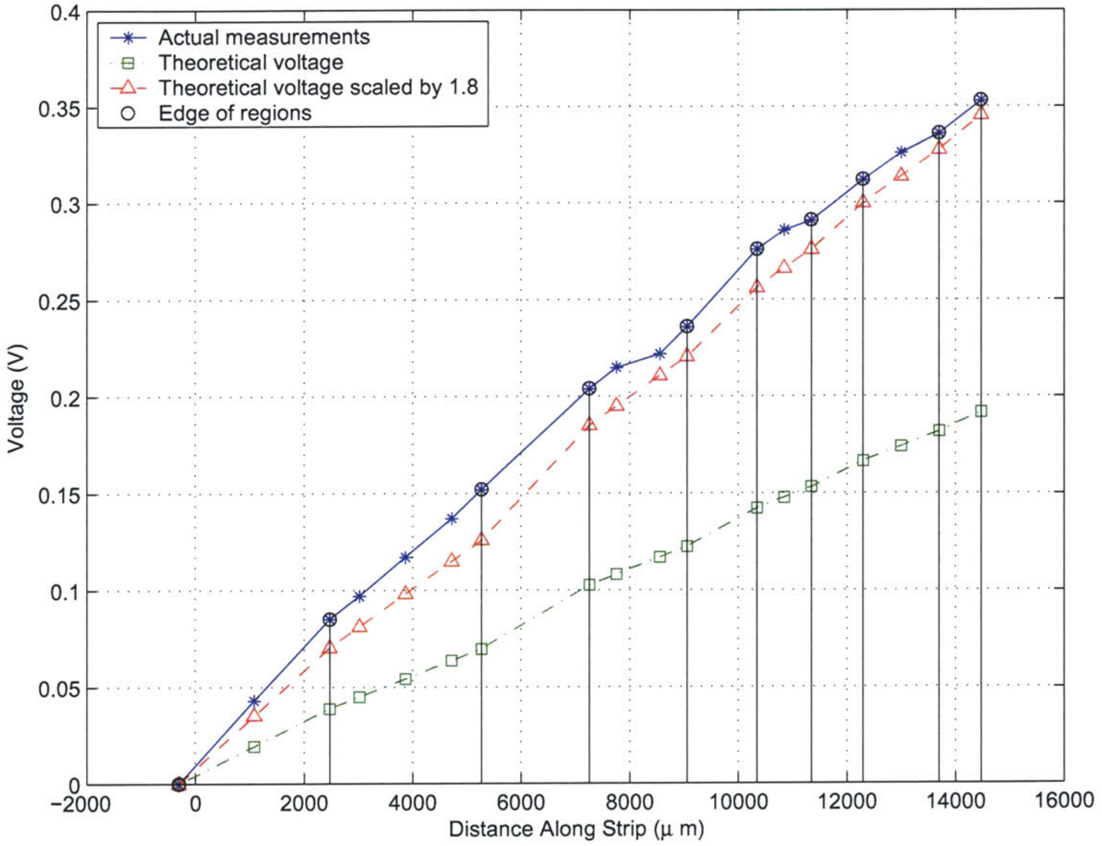

Figure 4-19: Voltage vs. distance along gold strip with 0.5 A current.

4.6 Photographs of Device During Fabrication

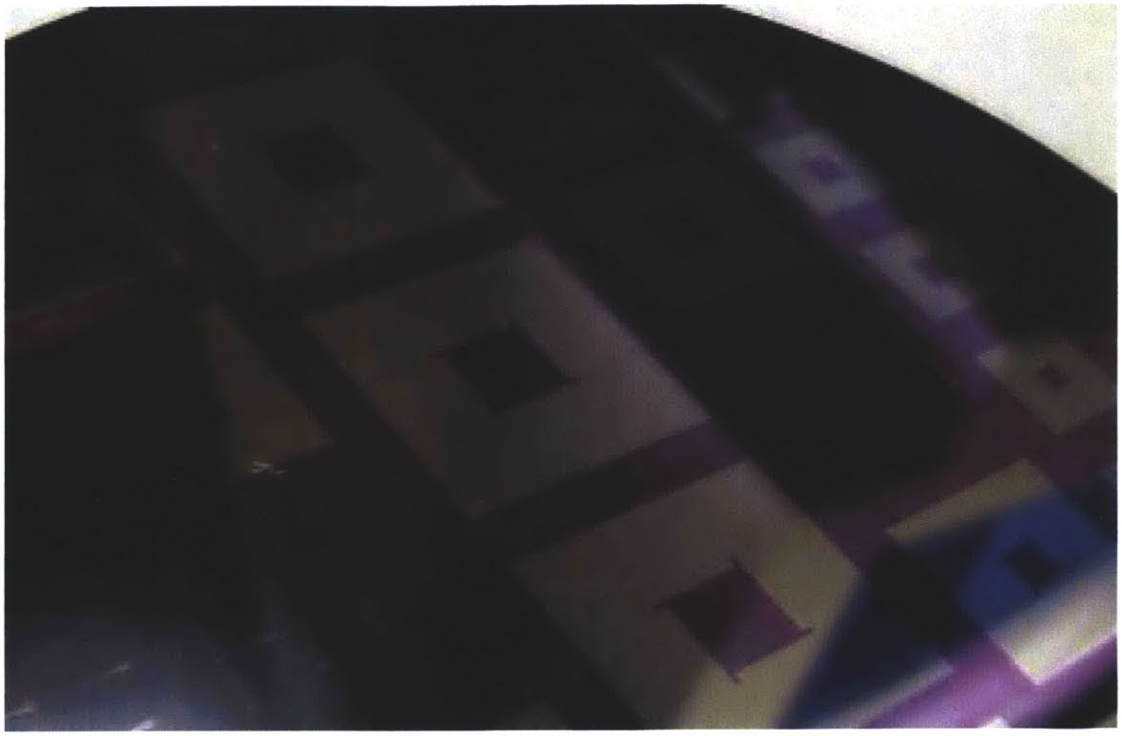

Figure 4-20: Photograph of device wafer after nitride etch and before photoresist removal.

Figure 4-20 is a photograph of a device wafer after the nitride mask is etched and before the photoresist is removed. The red-violet regions are the photoresist and the white regions are silicon. Note the small rectangular compensation structures.

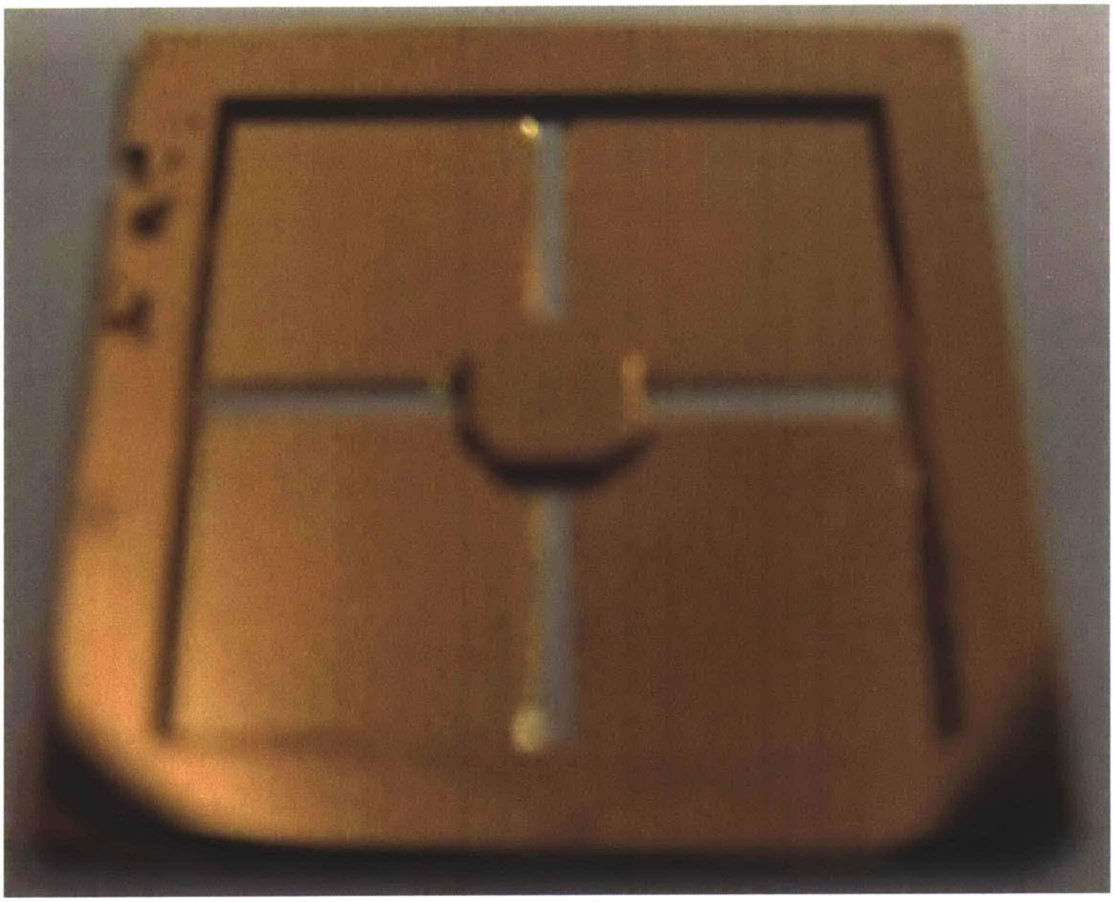

Figure 4-21: Photograph of one half-cavity die (Type C; 23 mm wide) with slits for a wire loop after gold deposition.

Figure 4-21 is a photograph of a one half-cavity die of Type C, which is 23 mm wide, with slits for a wire loop after gold deposition. The convex corners are slightly truncated, which will reduce the area of the capacitor plates, which in turn reduces capacitance and increases the resonant frequency of the resonator. There are some imperfections in the 2.5-mm-wide rim in the upper part of the left side. This may affect the ability of two dies to bond successfully.

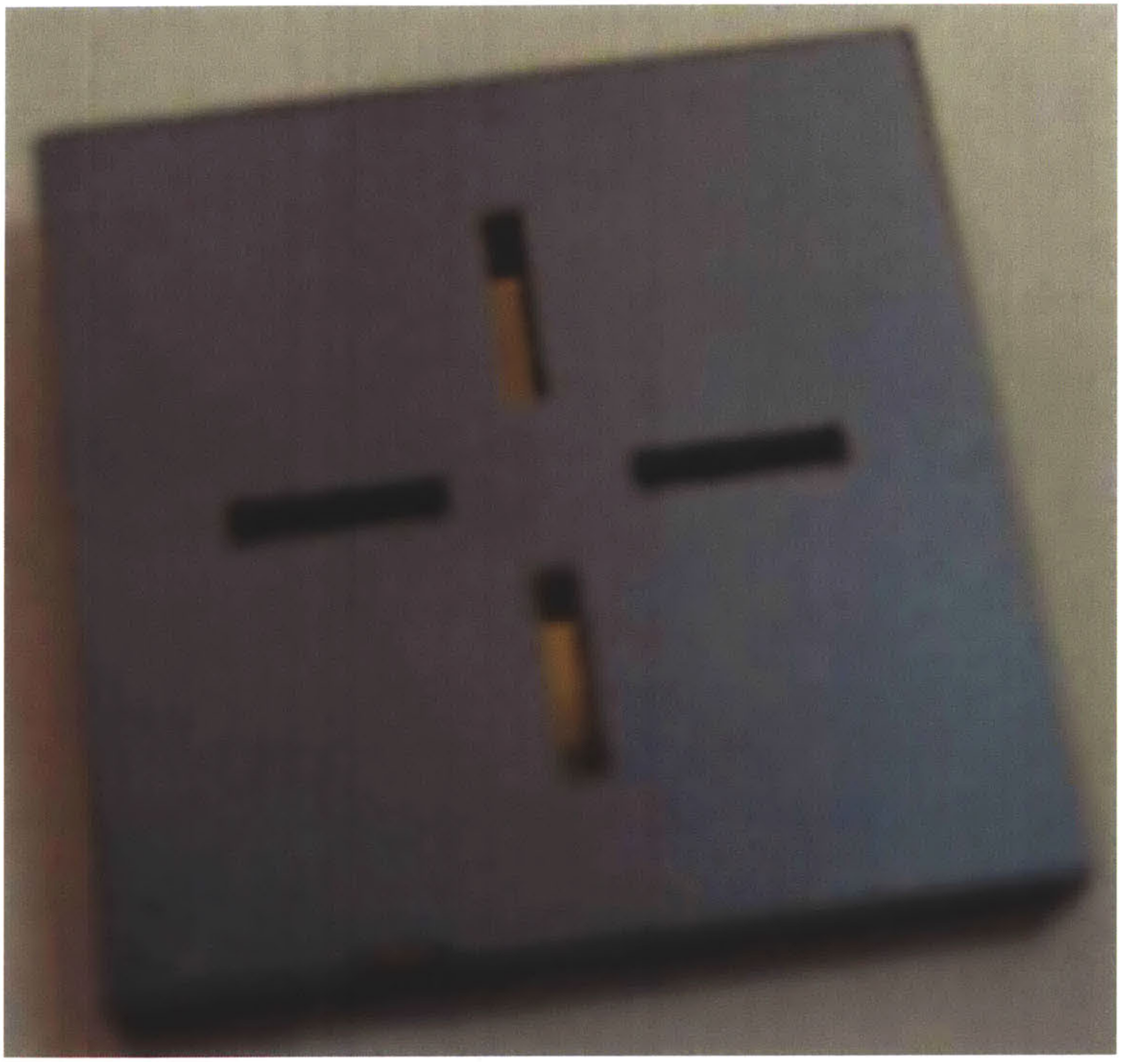

Figure 4-22: Photograph of a resonator (Type E; 16 mm wide) after wafer bonding without piezoelectric actuator as viewed from side with wire slits.

Figure 4-22 shows a photograph of a resonator of Type E, which is 16 mm wide, after wafer bonding without an piezoelectric actuator as viewed from the side with wire slits. The gray region is silicon. Through the slits, we can see the gold-lined interior cavity.

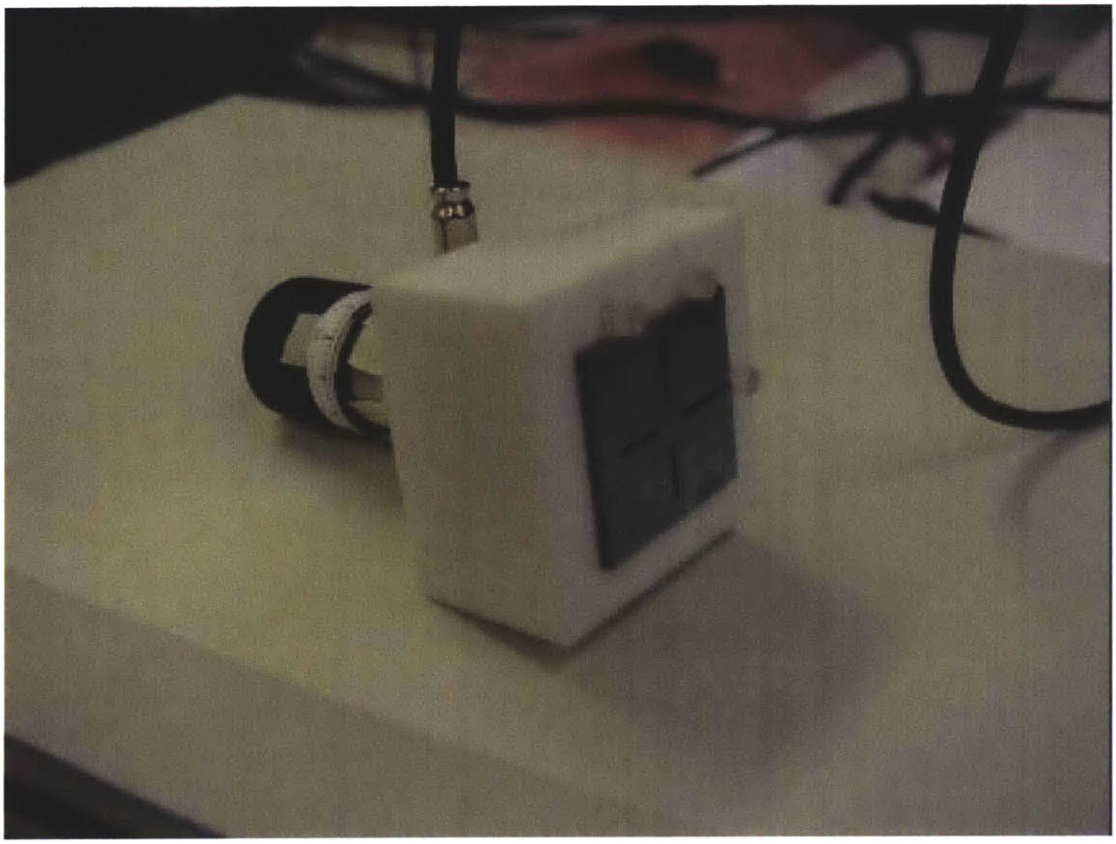

Figure 4-23: Photograph of a resonator (Type C; 23 mm wide) mounted on a Teflon block with a piezoelectric actuator.

Figure 4-23 shows a photograph of a resonator of Type C, which is 23 mm wide, mounted on a Teflon block with a piezoelectric actuator. The resonator is glued onto the block, and the protruding posts align the resonator in the center of the block. The block has a cavity drilled through so that a round piezoactuator can fit neatly from the other side. When voltage is applied via the black wire shown, the actuator depressed the capacitor gap and tunes the resonator.

4.7 Summary

This chapter presented the results of fabrication experiments. Corner compensation structures for KOH-etching silicon behaved as expected. The gold deposition rate of the EML sputterer was confirmed to operate at around 1 μm per hour. SEM images of gold coverage over sidewalls showed smooth surfaces, but there is debris on the wafer. EDX scans and spectral analysis showed that there is a distinct boundary between silicon and gold across the edge of a gold strip. A four-point probe test of the conductivity of gold over the sidewalls showed that the gold forms a conducting layer across the trench. Thus, sputtering gold on KOH-etched silicon is an acceptable method of creating conducting cavities.

Chapter 5

Device Model and Measurements

This chapter contains the measurements of tested devices and provides an analysis of an electrical model. The capacitor gap width is first determined indirectly by a measurement of the etch depth. The coupling wire loops and experimental setup are described. The frequency response of the resonator as the capacitor gap is reduced is shown and demonstrates that the resonator is tunable. A refined experimental circuit model is proposed and the data strongly supports the model. Finally, a photograph of an integrated resonator is shown.

5.1 Determining the Etch Depth for the Capacitor Gap Width

The most sensitive physical dimension of the resonator is the capacitor gap width. The gap is designed to be only 20 μm, so a variation by only a few microns can affect the capacitance dramatically. The EML Dektak was used to measure the depth of KOH-etched silicon over a step. This step region was bare silicon on one side of the line and nitride-protected on the other. As this test region is part of the device wafer and is etched at the same time as the capacitor gaps, it is a reliable measurement of the capacitor gaps.

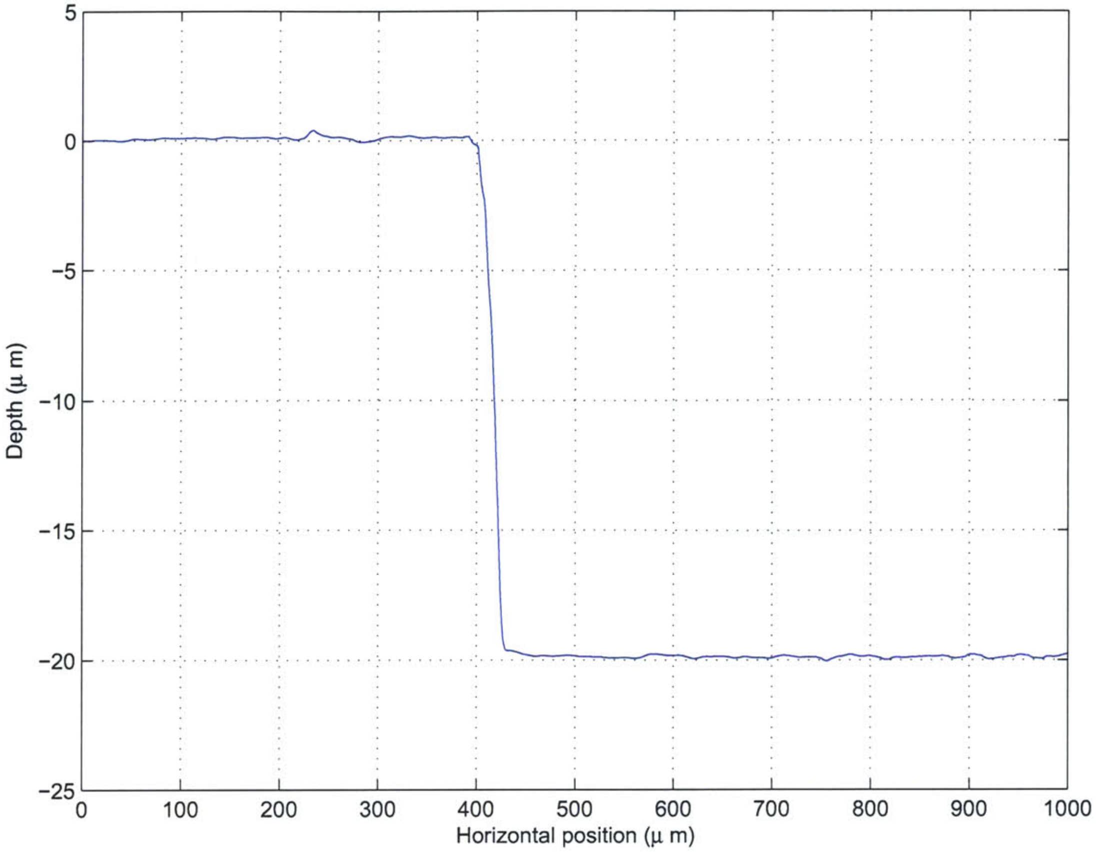

Figure 5-1: Dektak measurement of the depth of 15-minute etch in 20% KOH.

Figure 5-1 shows a Dektak measurement of the depth of KOH-etched silicon denoting the capacitor gap width. The left side of the graph is the depth of the top of the unetched portion of the wafer and the the right side is the depth of the top of the etched portion. This was a 15-minute etch in 20% KOH. It is almost exactly 20 μm, as needed.

However, the bonding surfaces between two dies will not be perfect. There may be microscopic particles embedded in the bond or the surfaces may not be completely smooth. Thus, the actual capacitor is expected to be slightly greater than the measured etch depth of 20 μm. In Section 5.4 beginning on Page 103, a more refined measurement of the capacitor gap width is determined using measurements of the resonant frequency as a function of gap width reduction.

5.2 Experimental Apparatus and Setup

The resonator is mounted on a block, and we insert the magnetic-coupling wire loop into the cavity. The wire loop is kept away from the cavity walls to minimize the induction of parasitic eddy currents and losses in the walls. The wire loop connects to an Agilent E8362B PNA series network analyzer through an SMA connector. The Smith chart in real-time is displayed with 16001 data points in the frequency range from the hundreds of MHz to around 8 GHz. Finally, impedance is measured as a calibrated piezoelectric actuator pushes on the resonator through a hole in the block to compress the cavity, thereby closing the capacitor gap and tuning the resonator.

5.2.1 Wire loops

A difficulty encountered during device testing was designing and building the wire loops. The first wire loop connector is simply a loop of 36 gauge copper wire soldered onto the leads of an SMA connector. However, it soon became apparent that the wire loop was too long and thus contributed adversely to the losses in the device. Later, the legs of the SMA connector were cut off and a much shorter wire was attached. All data presented below were done with the shorter loop. Figure 5-2 shows photographs of the first and last wire loop connectors used to measure the resonator frequency response.

5.2.2 Setup

The resonator and the wire loop connector are mounted separately. The position of the resonator relative to the lab table is fixed, and the connector is on a mount whose position in all three spatial dimensions can be adjusted by manually turning knobs. These parameters are fined-tuned until the frequency response, which are viewed in real time on the display of a network analyzer, exhibited a good resonance. Great care is taken to ensure that the loop does not get distorted as it moves within the resonator. Many times during testing, the loop had to be reshaped into a ring. Figure 5-3 shows a photograph of the experimental setup with a wire loop connector suspended in the resonator.

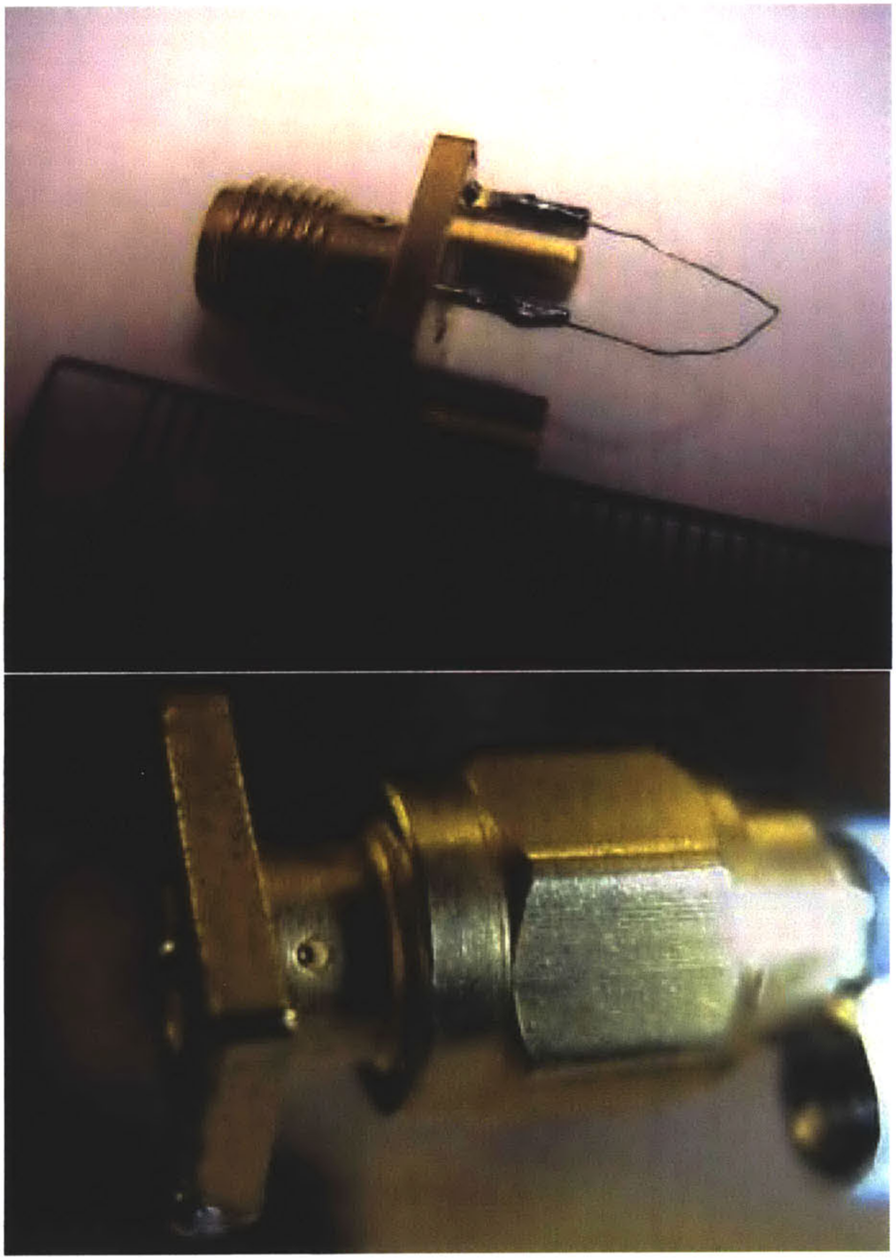

Figure 5-2: Photographs of the first (upper) and last (lower) wire loop connectors used.

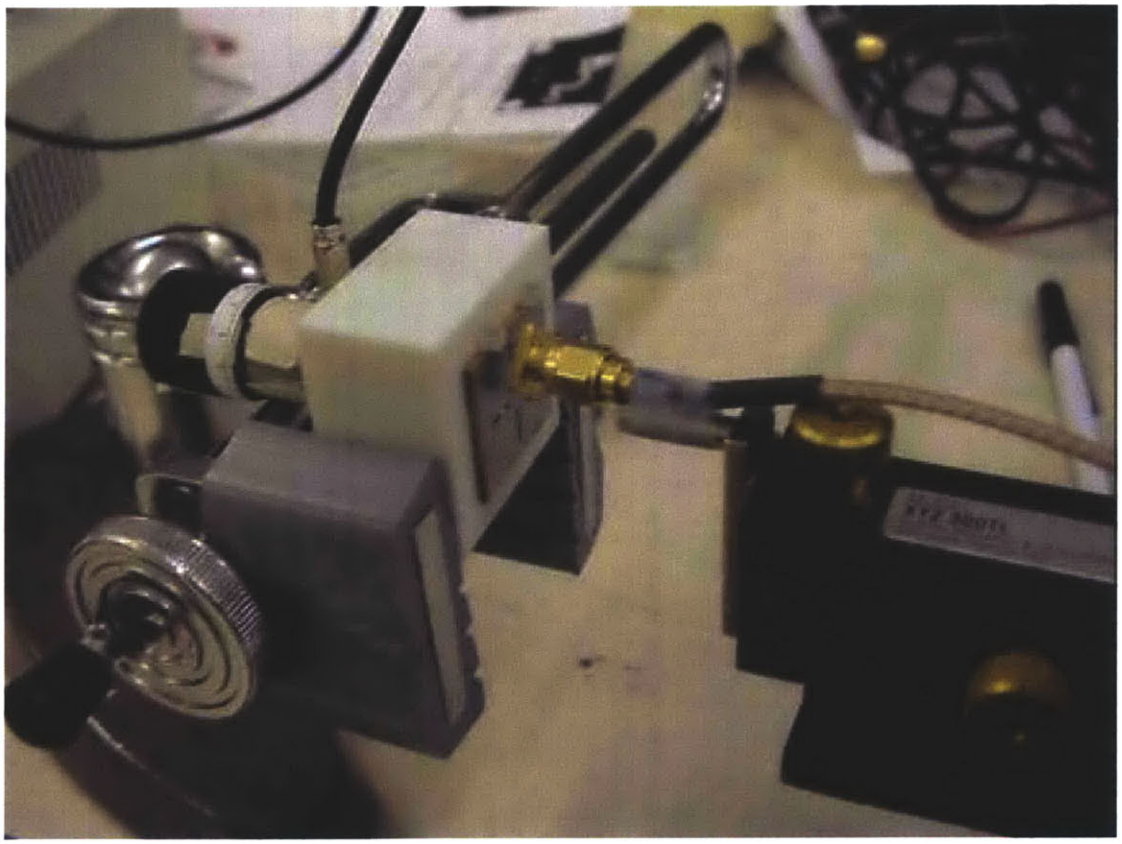

Figure 5-3: Photograph of the experimental setup with the wire loop connector suspended in the resonator.

5.2.3 Network analyzer

Figure 5-4: Photograph of the Agilent network analyzer with a Smith chart of the resonator impedance on the display.

Figure 5-4 shows a photograph of the Agilent network analyzer with a Smith chart of the resonator impedance on the display. Note the small loop in the trace. This denotes the location of the resonant peak.

5.3 Frequency Response

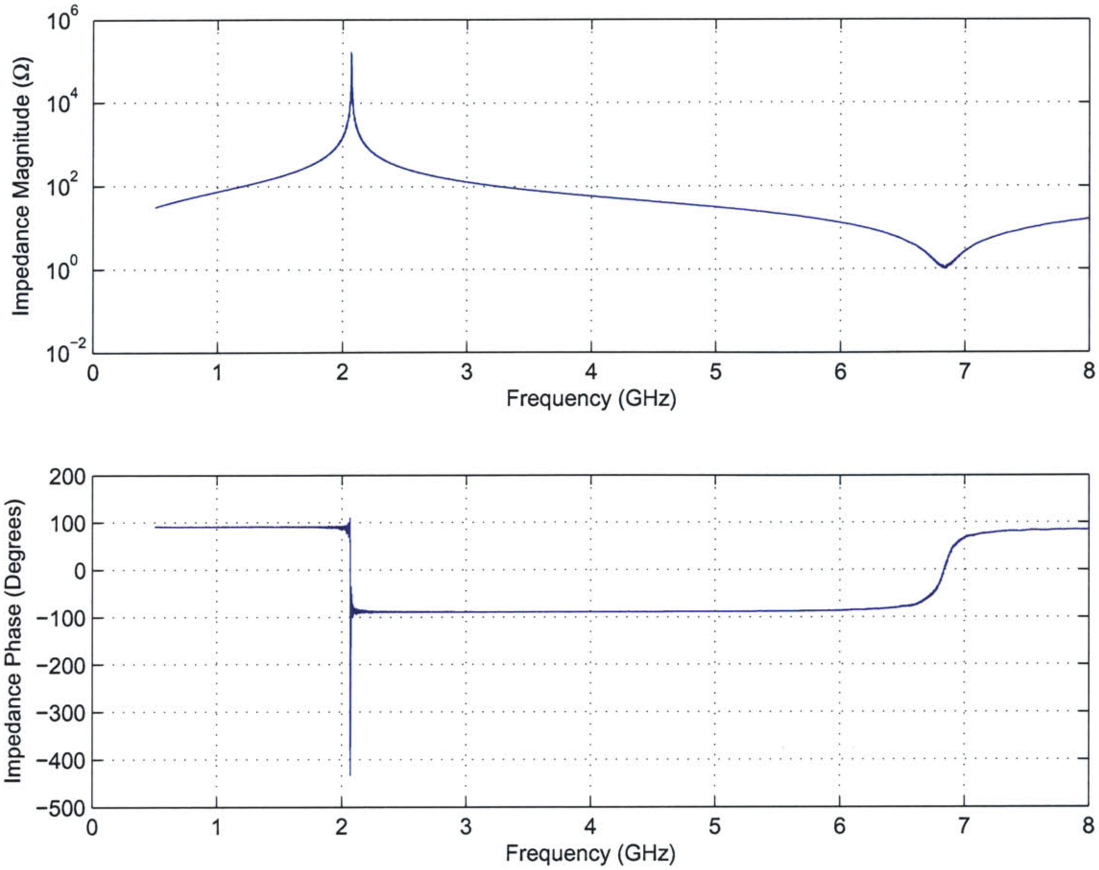

Figure 5-5: Impedance as a function of frequency for the last wire loop.

For all frequency response measurements, the maximum resolution of 16001 points is used. Figure 5-5 shows the impedance has a function of frequency for the latest wire loop alone. There is a sharp resonant peak at around 2 GHz. Appendix F beginning on Page 141 contains the MATLAB script `C1_and_loop_plot_freqresp.m` that produced the frequency response plots pertaining to the loop and device C1 presented in Figures 5-5, 5-6, 5-7 and 5-8. This code also calculated the resonant frequencies and the corresponding Q's at 15 different gap changes with the auxiliary function `bdwidth_win.m` whose code is given in Appendix F beginning on Page 140.

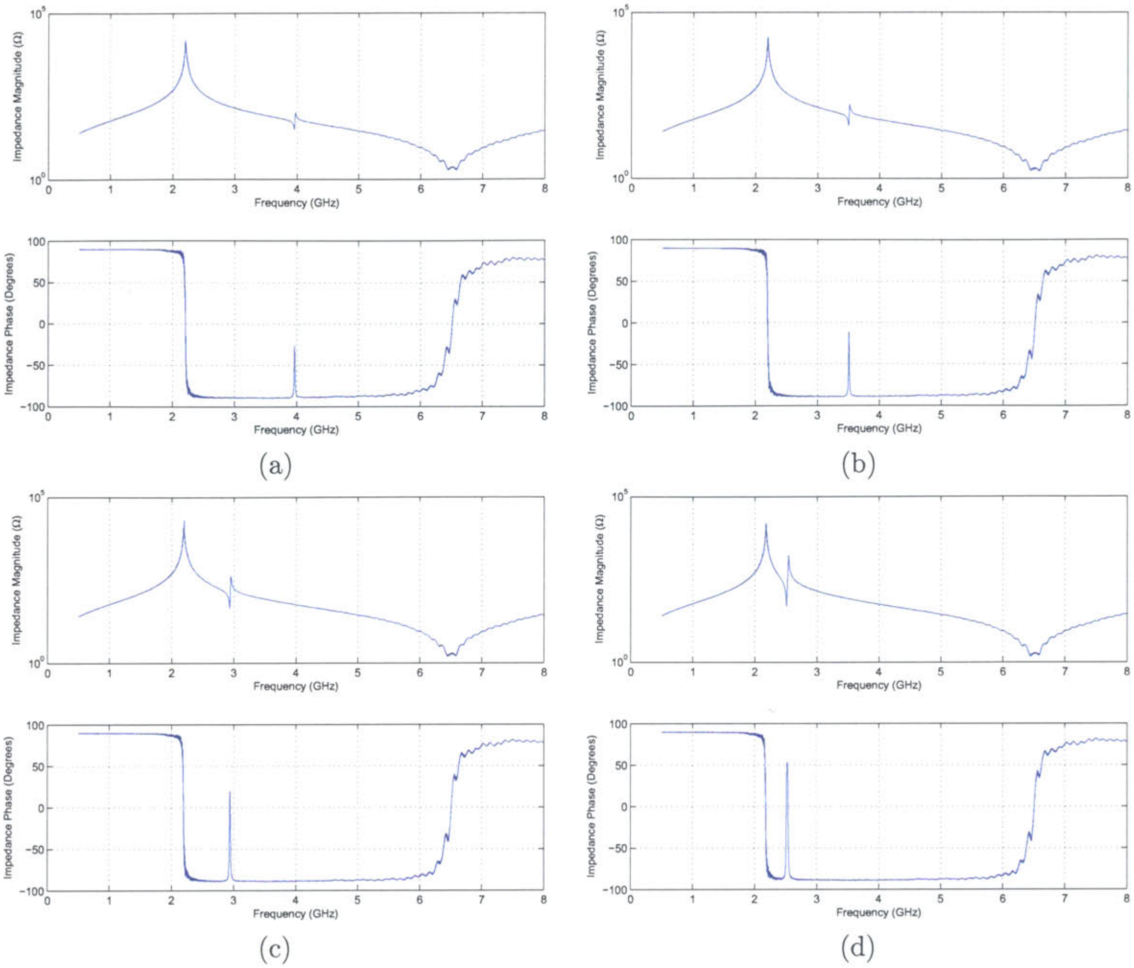

(a) (b)

(c) (d)

Figure 5-6: Impedance as a function of frequency (device C1) when the capacitor gap is reduced by (a) 0 μm, (b) 5 μm, (c) 10 μm, (d) 13.9 μm.

Figure 5-6 shows impedance as a function of frequency when the capacitor gap is reduced by 0 μm, 5 μm, 10 μm and 13.9 μm, for a device of type C. As it is the first device of this size that we fabricated, it is known as "C1." We see that there is a persistent peak at around 2.2 GHz. As this is nearly independent of the tank capacitance and is present in the frequency response of the loop alone, it is due to an inherent resonance in the wire loop. More importantly, there is a smaller peak at higher frequencies whose location is controlled by the amount of actuation. This is the bandpass filter that this thesis describes.

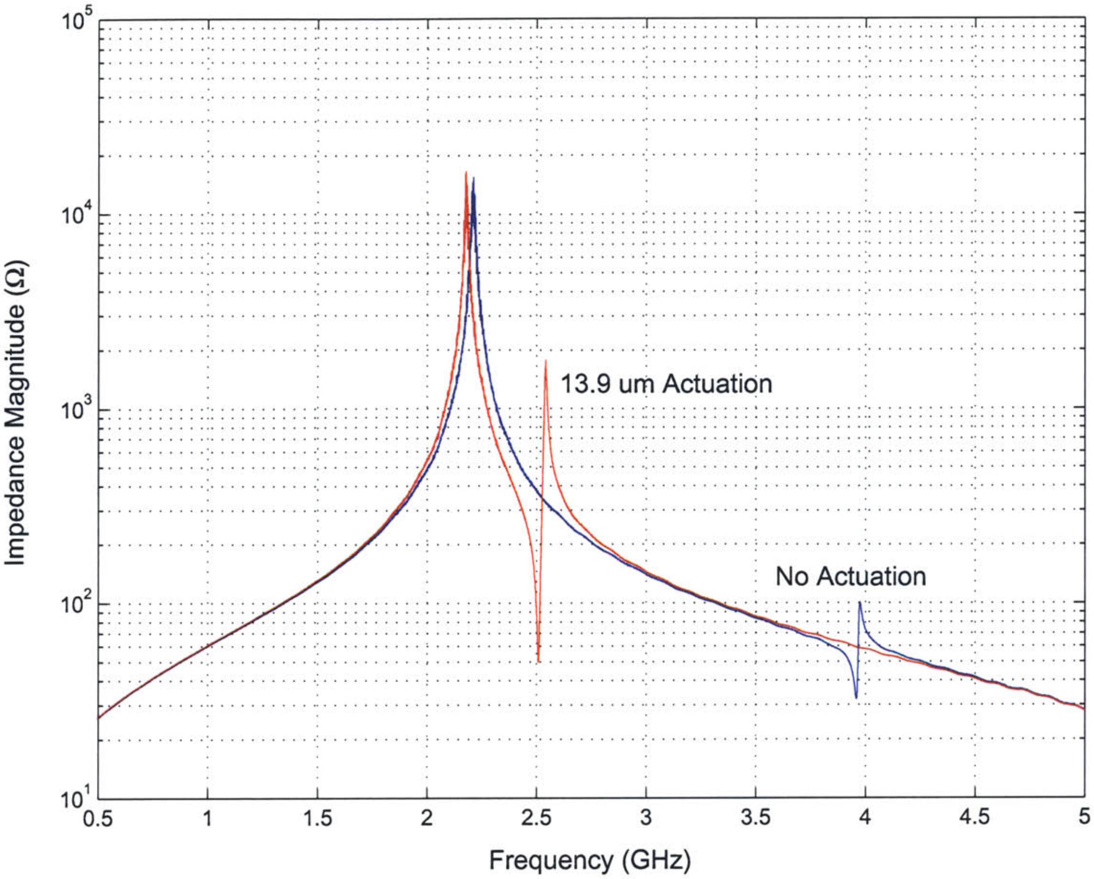

Figure 5-7: Resonator impedance magnitude as a function of frequency for 0-μm and 13.9-μm capacitor gap compression (device C1).

Figure 5-7 shows the resonator impedance magnitude as a function of frequency for 0-μm and 13.9-μm capacitor gap compression superimposed.

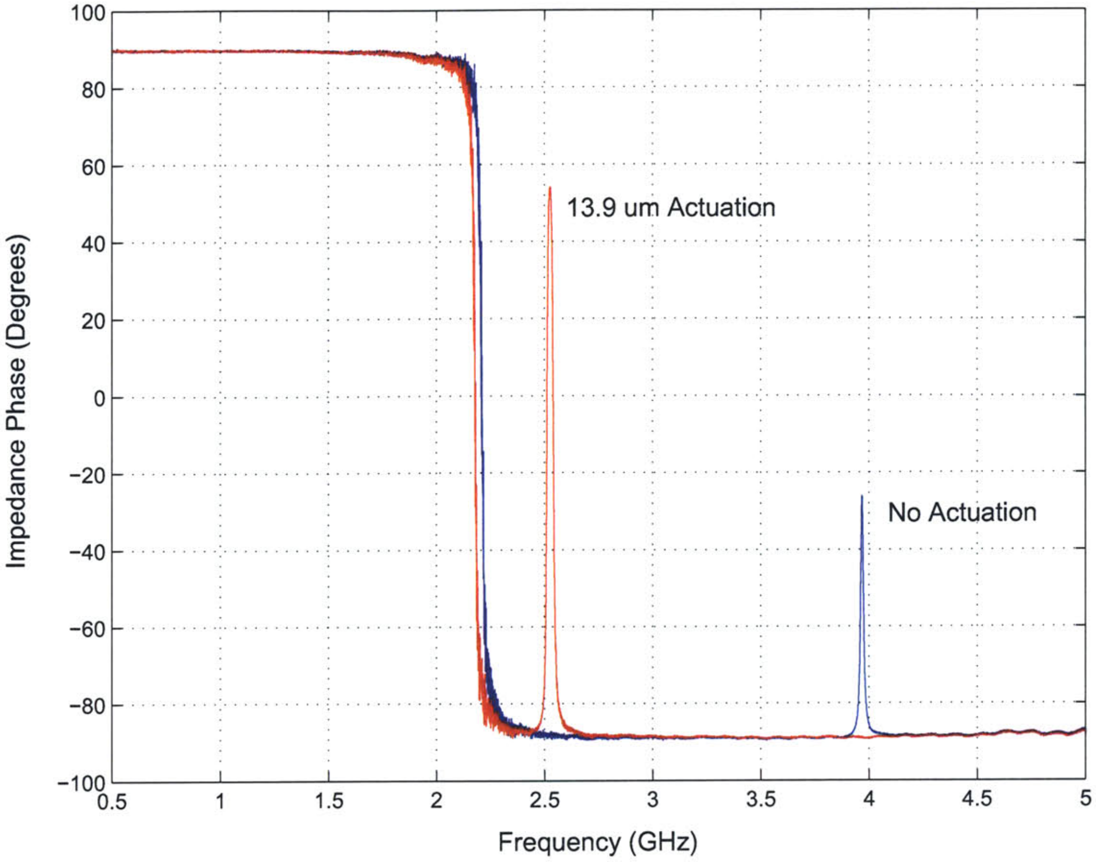

Figure 5-8: Resonator impedance phase as a function of frequency for 0-μm and 13.9-μm capacitor gap compression (device C1).

Figure 5-8 shows the resonator impedance phase as a function of frequency for 0-μm and 13.9-μm capacitor gap compression for a device of type C. There are likewise large phase changes at the similar locations as in the previous figure for the impedance magnitude.

5.4 Refining the Measurement of the Capacitor Gap Width

In Section 5.1 beginning on Page 93, we found that the KOH shaved off almost exactly 20 μm of the capacitor plateau to form the capacitor gap. In this section, a more refined measurement of the capacitor gap width is determined using measurements of the resonant frequency as a function of gap width reduction. From Equation 2.5 in Section 2.1.1 on Page 22, Equation 2.34 in Section 2.3.2 on Page 39, and the conversion from cyclic frequency f to angular frequency $\omega = 2\pi f$, we get

$$\begin{aligned} f_\circ &= \frac{\omega_\circ}{2\pi} = \frac{1}{2\pi\sqrt{LC}} && (5.1) \\ &= \frac{1}{2\pi\sqrt{L\frac{\epsilon_\circ w^2}{d}}} && (5.2) \\ \longrightarrow \quad f_\circ &= K\sqrt{d}. && (5.3) \end{aligned}$$

So, the resonant frequency $f_\circ$ is proportional to the square root of the capacitor gap width d where the constant of proportionality in terms of the free space permittivity $\epsilon_\circ$, inductance L and the capacitor plate width w is

$$K \equiv \frac{1}{2\pi w\sqrt{L\epsilon_\circ}}. \qquad (5.4)$$

If we denote the unactuated capacitor gap width as $d_\circ$ and the amount of gap reduction as Δd so that $d = d_\circ - \Delta d$, then the resonant frequency as a function of the gap reduction is

$$f_\circ = K\sqrt{d_\circ - \Delta d}. \qquad (5.5)$$

We can experimentally determine $d_\circ$ by measuring and plotting the resonant frequency against the gap reduction to produce some N points and finding the values of K and $d_\circ$ that minimize the mean-square error (MSE) between the calculated and measured values of $f_\circ$. Specifically, let Δd_i and $f_{\circ,i}$ where $i = 1, \ldots, N$ be the capacitor gap reduction and the corresponding resonant frequency, respectively, for the i^{th} data point. Then, the MSE estimates $\hat{K}$ and $\hat{d}_\text{o}$ for K and d_o are

$$(\hat{K}, \hat{d}_\text{o}) = \arg \min_{(K,d_\text{o})} \sum_{i=1}^{N} \left| f_{\text{o},i} - K\sqrt{d_\text{o} - \Delta d_i} \right|^2 . \tag{5.6}$$

Figure 5-9 shows the resonant frequency against the capacitor gap width reduction and along with the least-squares fit. The MATLAB function `lsqcurvefit` was used to determine the fit. Appendix F beginning on Page 146 contains the MATLAB script `C1_capgap.m` that produced Figure 5-9 and the corresponding diary on Page 147 give the values of the MSE estimates

$$\hat{K} = 0.819\,\text{GHz}/(\mu\text{m})^{1/2}, \tag{5.7}$$

$$\hat{d}_\text{o} = 23.2\,\mu\text{m}. \tag{5.8}$$

Thus, our estimate for the unactuated capacitor gap width is 23.2 μm. This estimate will be used from now on.

5.5 Experimental Circuit Model of Magnetically-Coupled Resonator

The frequency response measurements of actual device suggests the more refined experimental circuit model of the magnetically-coupled resonator in Figure 5-10. This is a correction from the ideal circuit model given in Figure 2-15 in from Section 2.3 on Page 38.

As before, denote C_T as the tunable tank capacitance, L_T as the fixed tank inductance and R_T as the sum of the series resistance of the tank inductor R_LT and that of the capacitor R_CT. The wire loop and the toroidal tank inductor form a transformer, where α is the ratio of the loop cross-sectional area to the tank inductor cross-sectional area. In the refined model, however, we have a resistance R_P to model eddy currents induced by the loop in the inductor walls. The leakage inductance L_L of the loop is divided into two parts: L_L1 is the component in parallel with R_P and L_L2 is the component that is not. As the wire loop

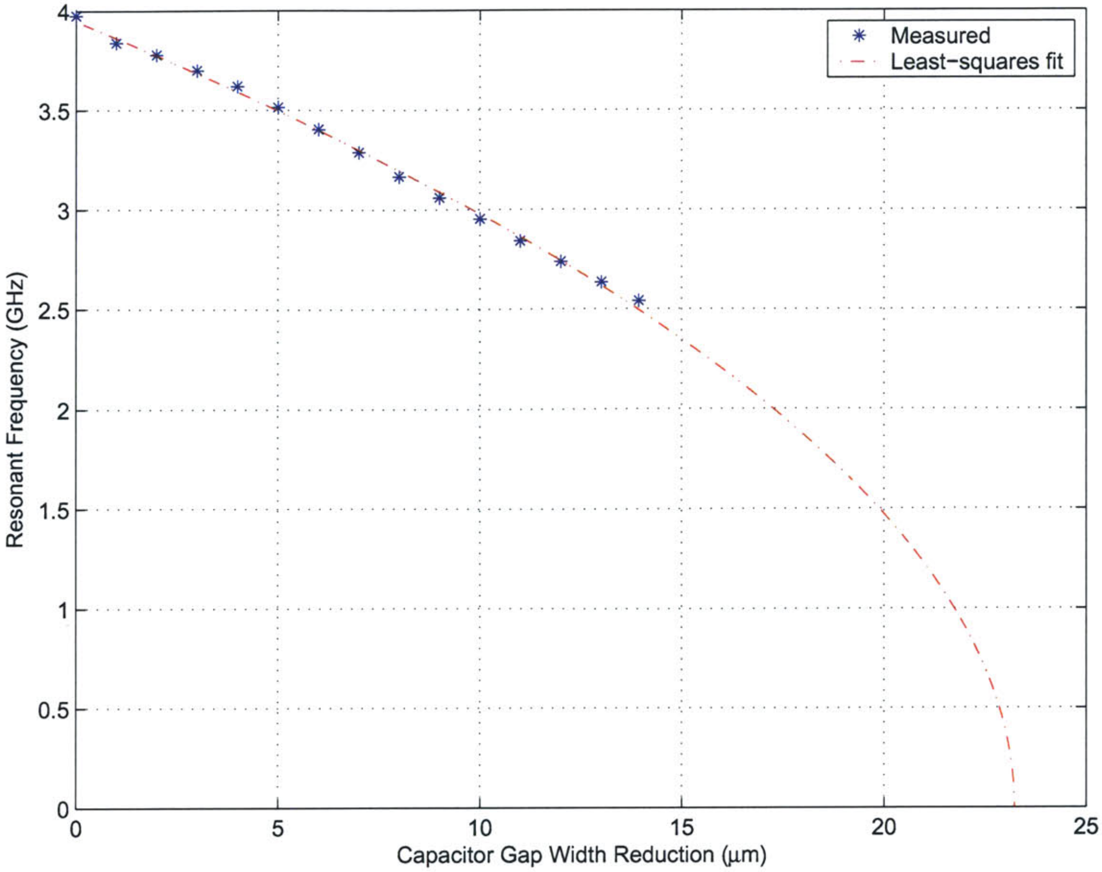

Figure 5-9: Resonant frequency as a function of capacitor gap width reduction and least-squares fit.

alone has a sharp resonance, it also has a distributed parasitic capacitance, which we will call C_{P}.

Applying conventional analysis to this is too tedious. Since the losses resistors in the experimental circuit model are relatively small so that the resonator has high Q, we can ease computation and gain insight by simplifying the experimental circuit model so that $R_{\mathrm{T}} = 0$ and $R_{\mathrm{P}} \to \infty$. Furthermore, not all the parameters can be uniquely determined from the transfer function, so without loss of generality, we can set $\alpha = 1$. The resulting lossless circuit model is shown in Figure 5-11.

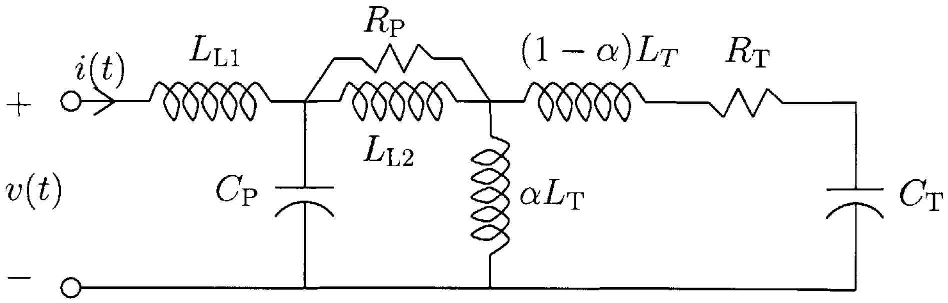

Figure 5-10: Experimental circuit model of magnetically-coupled resonator.

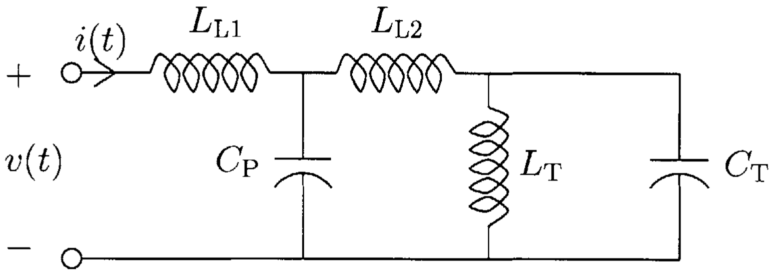

Figure 5-11: Lossless experimental circuit model of magnetically-coupled resonator.

The transfer function of the lossless experimental circuit model is

$$\begin{aligned}
H_{\text{lossless}}(s) &= sL_{L1} + \left(\frac{1}{sC_P} \| \left(sL_{L2} + \left(sL_T \| \frac{1}{sC_T}\right)\right)\right) && (5.9)\\
&= sL_{L1} + \left(\frac{1}{sC_P} \| \left(sL_{L2} + \frac{\frac{L_T}{C_T}}{sL_T + \frac{1}{sC_T}}\right)\right) && (5.10)\\
&= sL_{L1} + \left(\frac{1}{sC_P} \| \left(sL_{L2} + \frac{sL_T}{s^2L_TC_T + 1}\right)\right) && (5.11)\\
&= sL_{L1} + \left(\frac{1}{sC_P} \| \frac{sL_{L2}(s^2L_TC_T + 1) + sL_T}{s^2L_TC_T + 1}\right) && (5.12)\\
&= sL_{L1} + \frac{\frac{1}{sC_P} \cdot \frac{sL_{L2}(s^2L_TC_T+1)+sL_T}{s^2L_TC_T+1}}{\frac{1}{sC_P} + \frac{sL_{L2}(s^2L_TC_T+1)+sL_T}{s^2L_TC_T+1}} && (5.13)\\
&= sL_{L1} + \frac{sL_{L2}(s^2L_TC_T + 1) + sL_T}{s^2L_TC_T + 1 + sC_P(sL_{L2}(s^2L_TC_T + 1) + sL_T)}, && (5.14)
\end{aligned}$$

which placed under a common denominator becomes

$$\begin{aligned} H_{\text{lossless}}(s) &= \left[s^4 L_{\text{T}} C_{\text{T}} L_{\text{L2}} C_{\text{P}} + s^2(L_{\text{T}} C_{\text{T}} + L_{\text{L2}} C_{\text{P}} + L_{\text{T}} C_{\text{P}}) + 1\right]^{-1} \cdot && (5.15) \\ & \left[s L_{\text{L1}}(s^4 L_{\text{T}} C_{\text{T}} L_{\text{L2}} C_{\text{P}} + s^2(L_{\text{T}} C_{\text{T}} + L_{\text{L2}} C_{\text{P}} + L_{\text{T}} C_{\text{P}}) + 1)\right. && (5.16) \\ & \left. + s L_{\text{L2}}(s^2 L_{\text{T}} C_{\text{T}} + 1) + s L_{\text{T}}\right], && (5.17) \end{aligned}$$

which becomes

$$H_{\text{lossless}}(s) = s \frac{\begin{bmatrix} s^4 L_{\text{L1}} L_{\text{L2}} C_{\text{P}} L_{\text{T}} C_{\text{T}} \\ + s^2(L_{\text{L1}}(L_{\text{T}} C_{\text{T}} + L_{\text{L2}} C_{\text{P}} + L_{\text{T}} C_{\text{P}}) + L_{\text{L2}} L_{\text{T}} C_{\text{T}}) \\ + (L_{\text{L1}} + L_{\text{L2}} + L_{\text{T}}) \end{bmatrix}}{s^4 L_{\text{T}} C_{\text{T}} L_{\text{L2}} C_{\text{P}} + s^2(L_{\text{T}} C_{\text{T}} + L_{\text{L2}} C_{\text{P}} + L_{\text{T}} C_{\text{P}}) + 1}. \tag{5.18}$$

To write this in a form that can be used to determine parameters from the experimental frequency response, let's define auxiliary parameters

$$\begin{aligned} &M_1 = L_{\text{L1}}, \quad M_2 = L_{\text{L2}}, \quad M_3 = 1 + \tfrac{L_{\text{T}}}{L_{\text{L2}}}, \\ &M_4 = L_{\text{T}} C_{\text{T}}, \quad M_5 = L_{\text{L2}} C_{\text{P}}. \end{aligned} \tag{5.19}$$

Then, the transfer function can be rewritten as

$$H_{\text{lossless}}(s) = s \frac{s^4(M_1 M_4 M_5) + s^2(M_1 M_4 + M_1 M_3 M_5 + M_2 M_4) + (M_1 + M_2 M_3)}{s^4(M_4 M_5) + s^2(M_4 + M_3 M_5) + 1}. \tag{5.20}$$

This must be matched to the measured transfer function, which has two pairs of conjugate poles and two pairs of conjugate zeros. Let these poles occur at $\pm j/\tau_{\text{p1}}$ and $\pm j/\tau_{\text{p2}}$, and the zeros occur at $\pm j/\tau_{\text{z1}}$ and $\pm j/\tau_{\text{z2}}$. Thus, the measured transfer function takes the form

$$H_{\text{lossless}}(s) = sG \frac{(1 + s^2 \tau_{\text{z1}}^2)(1 + s^2 \tau_{\text{z2}}^2)}{(1 + s^2 \tau_{\text{p1}}^2)(1 + s^2 \tau_{\text{p2}}^2)}. \tag{5.21}$$

To match this with Equation 5.20, let's multiply out the terms in Equation 5.21 to get

$$H_{\text{lossless}}(s) = s \frac{s^4(\tau_{\text{z1}}^2 \tau_{\text{z2}}^2 G) + s^2(\tau_{\text{z1}}^2 + \tau_{\text{z2}}^2)G + G}{s^4(\tau_{\text{p1}}^2 \tau_{\text{p2}}^2) + s^2(\tau_{\text{p1}}^2 + \tau_{\text{p2}}^2) + 1}. \tag{5.22}$$

By matching the terms in Equations 5.20 and 5.22, we obtain the following expressions for M_i in terms of τ_{zi}, τ_{pi} and G:

$$M_1 = \frac{\tau_{z1}^2 \tau_{z2}^2 G}{\tau_{p1}^2 \tau_{p2}^2}, \tag{5.23}$$

$$M_4 = \tau_{p1}^2 + \tau_{p2}^2 - \frac{(G - M_1)(\tau_{p1}^2 \tau_{p2}^2)}{G(\tau_{z1}^2 + \tau_{z2}^2) - M_1(\tau_{p1}^2 + \tau_{p2}^2)}, \tag{5.24}$$

$$M_5 = \frac{\tau_{p1}^2 \tau_{p2}^2}{M_4}, \tag{5.25}$$

$$M_3 = \frac{\tau_{p1}^2 + \tau_{p2}^2 - M_4}{M_5}, \tag{5.26}$$

$$M_2 = \frac{G - M_1}{M_3}. \tag{5.27}$$

Finally, the original circuit parameters can be recovered from the M values as follows.

$$L_{L1} = M_1, \tag{5.28}$$

$$L_{L2} = M_2, \tag{5.29}$$

$$L_T = M_2(M_3 - 1), \tag{5.30}$$

$$C_T = \frac{M_4}{M_2(M_3 - 1)} = \frac{M_4}{L_T}, \tag{5.31}$$

$$C_P = \frac{M_5}{M_2} = \frac{M_5}{L_{L2}}. \tag{5.32}$$

5.6 Device Parameters

For device C1, $W = 18$ mm, $w = 4$ mm, $D = 1$ mm, and $d = 23.2\,\mu$m, as fabricated for an uncompressed resonator. From Equations 2.5, 2.34 and 2.48, we expect that $C_T = 6.11$ pF, $L_T = 220$ pH, and $\omega_T/2\pi = 4.34$ GHz. At this frequency, the skin depth of gold is $\delta = 1.19\,\mu$m. From Equations 2.26, 2.27, 2.28, 2.53 and 2.62, we expect that $R_{LT} = 26.0\,\text{m}\Omega$, $R_{CT} = 1.63\,\text{m}\Omega$, $Q_{CT} = 3680$, $Q_{LT} = 231$, and $Q_T = 217$. In general, the inductor is always more lossy than the capacitor.

Let's apply the analysis in the previous section to the no actuation case in Figure 5-6. The two peaks occur at

$$1/\tau_{\mathrm{p1}} = 2.2080\,\mathrm{GHz}, \tag{5.33}$$

$$1/\tau_{\mathrm{p2}} = 3.9695\,\mathrm{GHz}, \tag{5.34}$$

and the two dips occur at

$$1/\tau_{\mathrm{z1}} = 3.9610\,\mathrm{GHz}, \tag{5.35}$$

$$1/\tau_{\mathrm{z2}} = 7.0000\,\mathrm{GHz}.^{1} \tag{5.36}$$

The slope of the low-frequency is the scale factor G

$$G = 7.70 \times 10^{-9}\,\Omega. \tag{5.37}$$

Appendix F contains the MATLAB script `C1_model.m` beginning on Page 148 that runs the above analysis on these experimental values and produces Figures 5-12 and 5-13. The corresponding diary begins on Page 150. This produces the values

$$L_{\mathrm{L1}} = 769\,\mathrm{pH}, \tag{5.38}$$

$$L_{\mathrm{L2}} = 6.88\,\mathrm{nH}, \tag{5.39}$$

$$C_{\mathrm{P}} = 747\,\mathrm{fF}. \tag{5.40}$$

From terminal impedance measurements alone, it is not possible to uniquely determine α, L_{T}, C_{T}, L_{L2}, and $R_{\mathrm{T}} \equiv R_{\mathrm{LT}} + R_{\mathrm{CT}}$. Therefore, C_{T} will be taken to be 6.11 pF, as given by Equation 2.34 for the as-fabricated dimensions. It follows from the resonant frequency that we should let $L_{\mathrm{T}} = 266$ pH. We guess values for α, R_{LT}, R_{CT} and R_{P} and plot the resulting frequency response. The values are adjusted until the fit is a good as possible. Thus, the

---

[1] This value was tweaked until the lower-frequency impedance matched. It was not possible to match the high-frequency impedance.

rest of the model parameters are determined to be

$$\alpha = 0.431, \tag{5.41}$$

$$R_{\mathrm{T}} = 22.4\,\mathrm{m}\Omega, \tag{5.42}$$

$$R_{\mathrm{P}} = 11\,\mathrm{k}\Omega. \tag{5.43}$$

The tank quality factor for these parameters is

$$Q_{\mathrm{T}} = 295. \tag{5.44}$$

These parameters are very close to those predicted at the beginning of this section. As we can see in Figures 5-12 and 5-13, the match between the modeled and measured impedance is extremely good up to and beyond 5 GHz, with less than a 1% error in magnitude and phase. At frequencies above 6 GHz, the modeled and measured impedance diverges, most likely due to distributed wire loop dynamics that is not captured by the lumped-parameter model of Figure 5-10. Note that to compute the modeled resistances, the frequency-dependent skin depth of gold was used in Equations 2.53 and 2.62.

With a capacitor gap compression of 13.9 μm, Equation 2.34 predicts a tuned C_{T} of 15.2 pF. With only this change to its parameters, the model of Figure 5-10 predicts the tuned impedance shown in Figure Figure 5-6(d) with the same level of accuracy as it does the untuned impedance. Similar tests can be repeated for all capacitor gap compressions from 1 μm to 13 μm in 1 μm steps with identical results. Thus, it can be concluded that the resonator behaves as predicted.

Figure 5-14 shows the measured tank resonant frequencies that result from each 1-μm step in capacitor gap compression, together with a theoretical prediction based upon Equations 2.34 and 2.5, and the fitted value of L_{T}, 266 pH. The good match underscores the validity of the earlier theoretical analysis. Figure 5-15 shows the corresponding measured Q of the resonator, and the estimated Q of the tank alone based on Equation 2.28 and the fitted parameters of the model in Figure 5-10. Note that the Q of the tank is generally higher than that of the complete resonator owing to the losses induced by the wire loop.

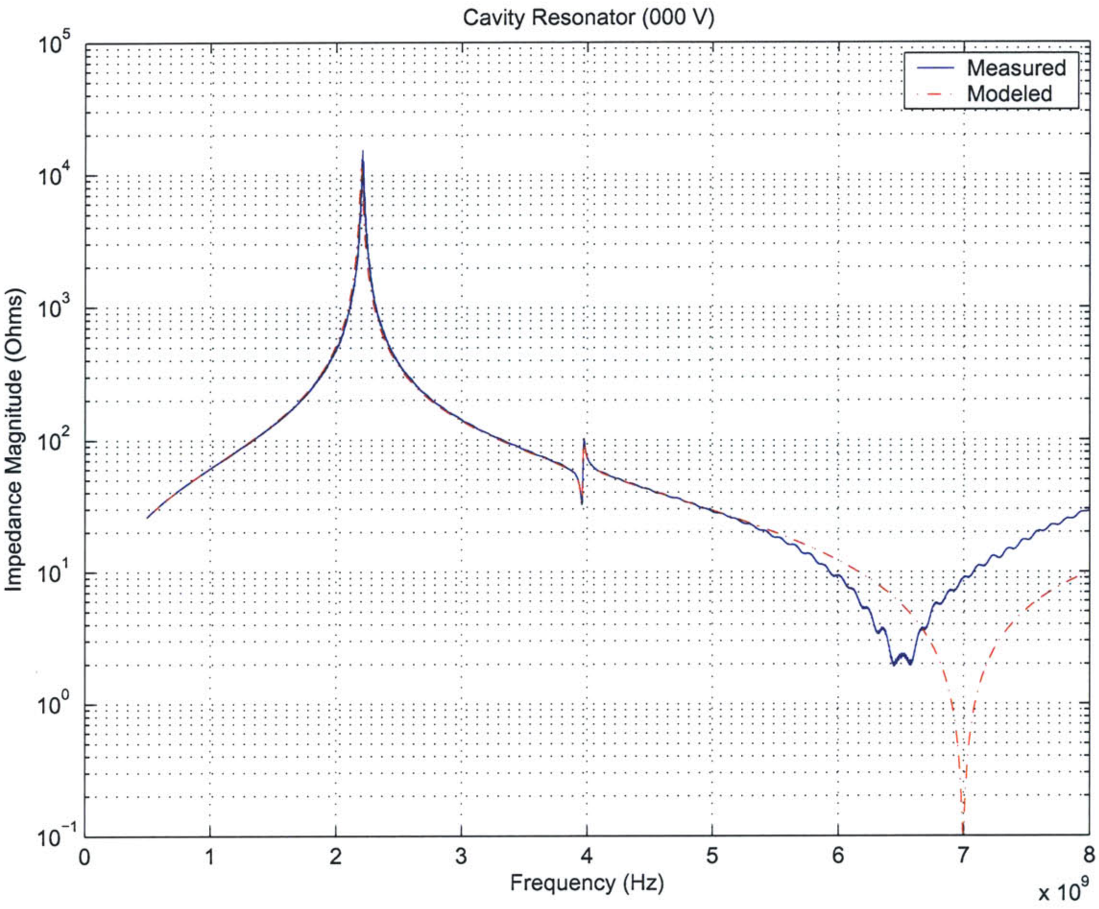

Figure 5-12: Measured and modeled resonator impedance magnitude as a function of frequency.

It is not, however, as high as predicted. Appendix F beginning on Page 151 contains the script `C1_plot_resfreq_q.m` that produced the figures.

5.7 Summary

This chapter showed the experimental setup used to test the devices and presented the measurements of tested devices. Although the capacitor etch gap was measured to be 20 μm, electrical measurements showed that it was 23.2 μm. A network analyzer was used to measure the impedance of the resonator as a function of frequency, and there was a clear

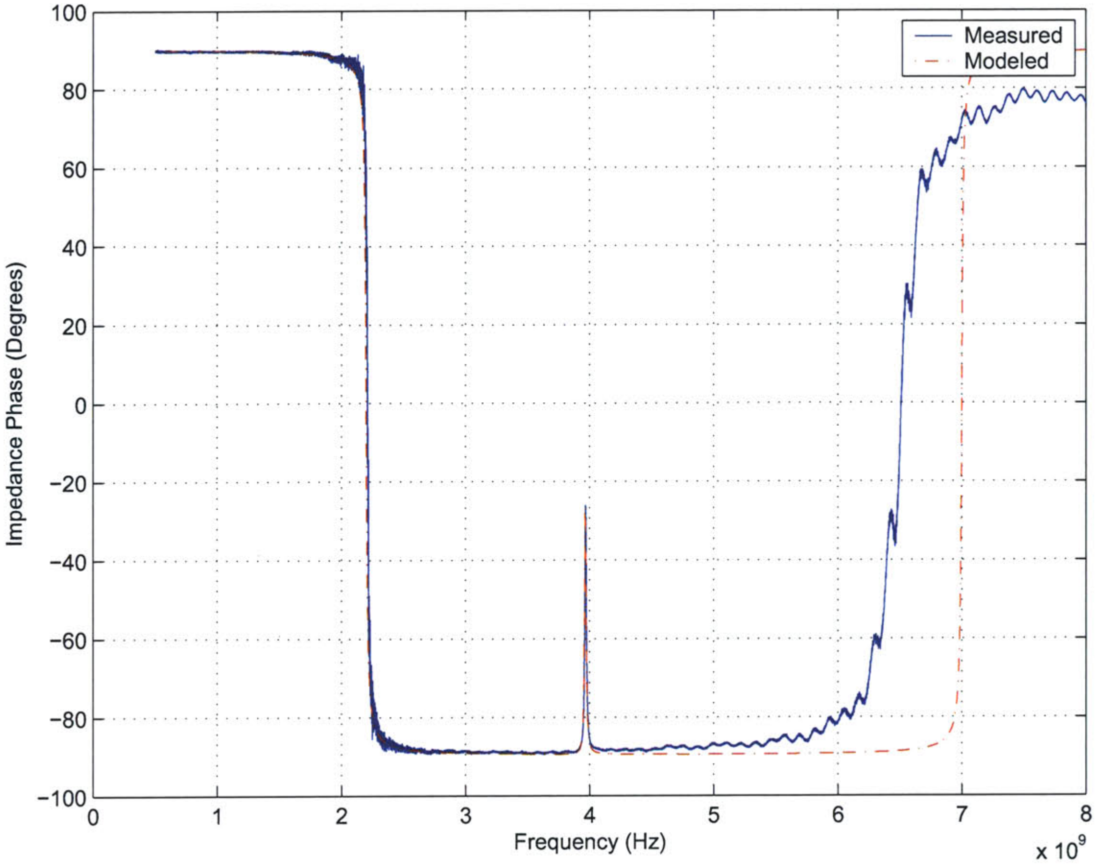

Figure 5-13: Measured and modeled resonator impedance phase as a function of frequency.

resonant peak that could be tuned as the capacitor gap is reduced. A refined experimental circuit model was proposed and the data strongly supported the model. Circuit parameters calculated from the measured impedance agreed with the theoretical values and produced an impedance that matched the measured impedance to within 1% in both magnitude and phase up to 5 GHz. Although the measured values of Q weren't as high as the predicted values, it is still good for a widely-tunable resonator in the gigahertz range.

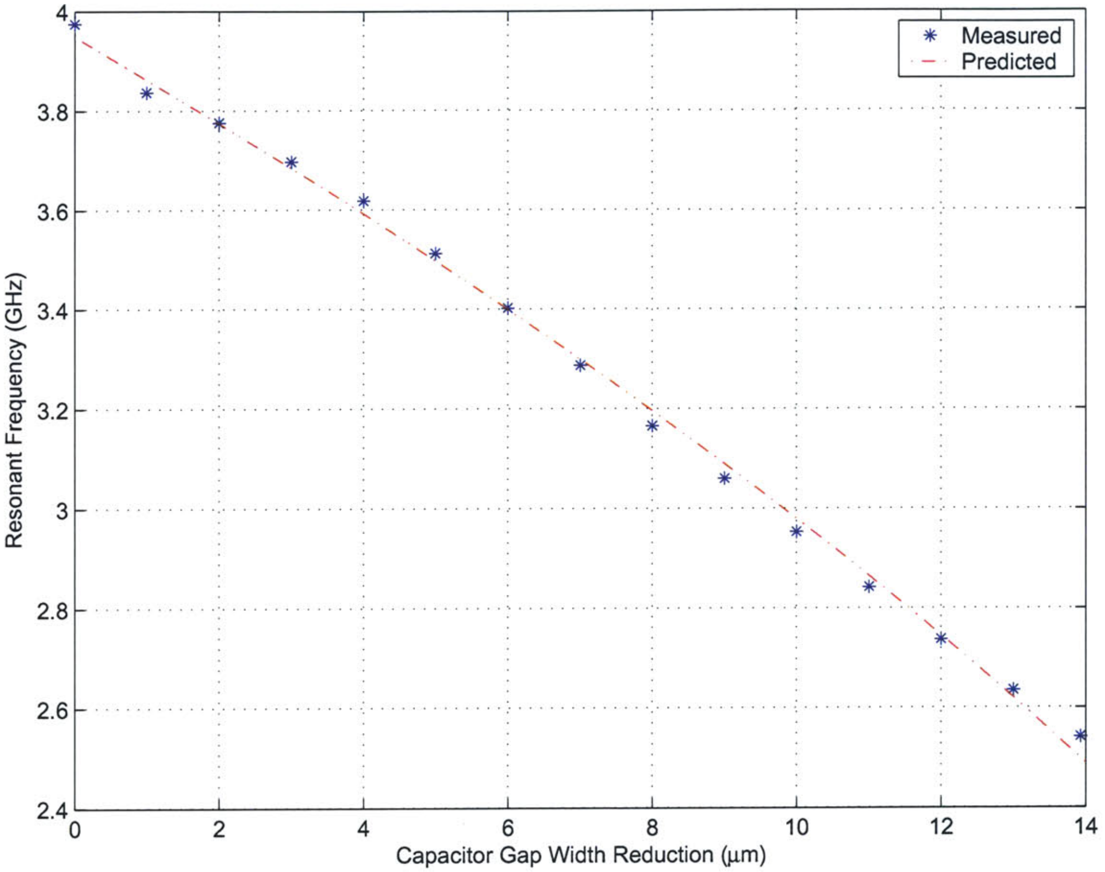

Figure 5-14: Measured and predicted tank resonant frequency ω_T as a function of the decrease in capacitor gap.

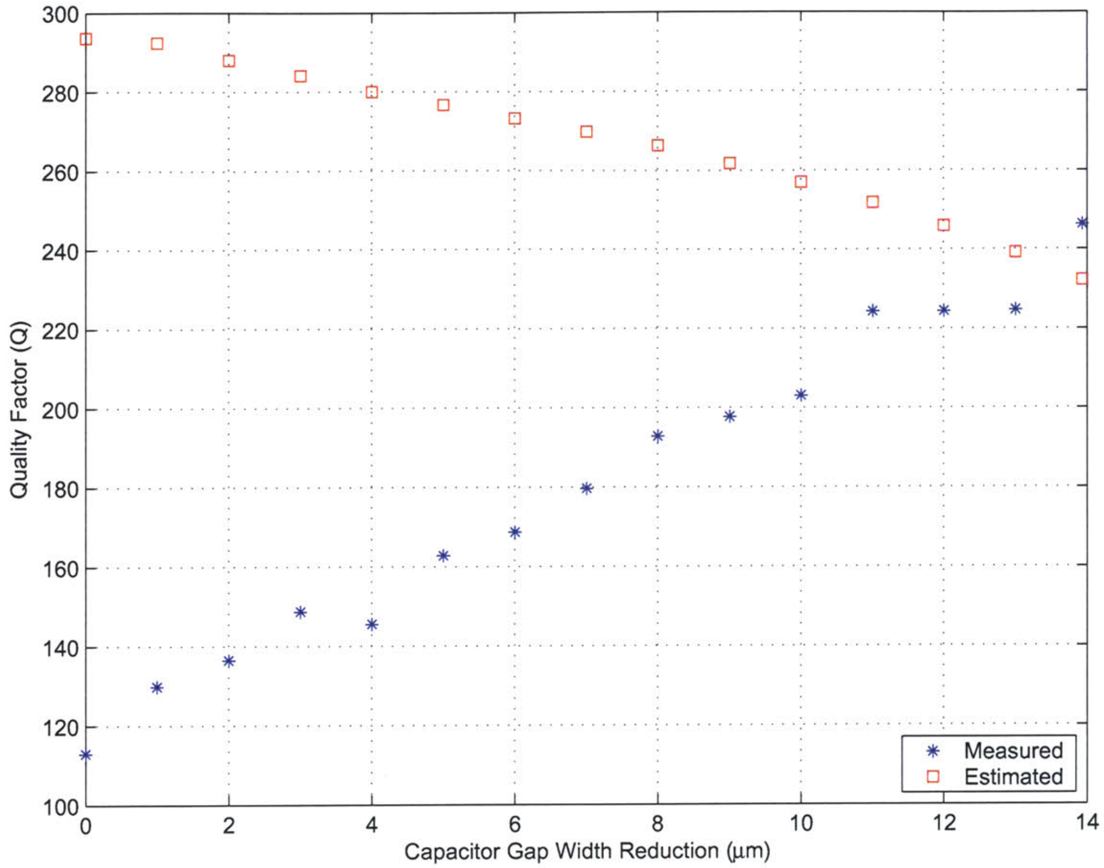

Figure 5-15: Measured resonator and estimated tank quality factors at the resonance of ω_{T} as functions of the decrease in capacitor gap.

Chapter 6

Summary, Conclusions and Future Work

This chapter has three parts. The summary provides a overview of this thesis. The conclusions contains the results of this work and lessons learned. The final section lists suggestions for future work and explains how weaknesses can be improved.

6.1 Summary

This thesis presented the design, fabrication and testing of a electromagnetic cavity resonator that has been demonstrated to be widely-tunable in the range of 2.5 GHz to 4.0 GHz and to exhibit high Q near 200. Parameters were successfully fitted to an experimental circuit model and the resulting modeled impedance matched the measured impedance up to 5 GHz with less than 1% error in magnitude and phase. These results are detailed in Chapter 5.

The resonator is fabricated using standard MEMS technologies and consists of a gold-lined capacitor and toroidal inductor cavity formed by etching silicon in potassium hydroxide. Frequency tuning is performed by compressing the cavity to close the capacitor gap. Testing was done with a piezoelectric actuator for this task. An electromagnetic analysis of the device and the design of its physical dimensions was discussed in Chapter 2. Chapter 3 explained fabrication design, including corner compensation, mask alignment, wafer etching and wafer bonding. A detailed process flow is given in Appendix D beginning on Page 127. Experiments shown in Chapter 4 confirmed that a gold layer deposition on KOH-etched silicon produces an adequate conducting layer for the resonator. Microscope photographs and SEM scans showed that the sidewalls are smooth and metal over the edges are continuous. Section 4.5 contains the results of a four-point probe test that proved the electrical conductivity of gold strips across several KOH-etched trenches.

6.2 Conclusions

The primary conclusion of this thesis is that a cavity resonator can exhibit both high-Q, around 200, and a wide high-frequency tuning range. We found that piezoelectrics are good actuators to perform the task of tuning. Furthermore, these resonators can be relatively simple to fabricate. In order to become acceptable to most applications, however, two modifications to the resonator as presented here must be made. First, direct electrical coupling to the capacitor should replace the magnetic coupling through a wire loop. As discussed in Chapter 5, the leakage inductance, and parasitic capacitance and resistance, of the wire loop appear to be generally too high. Second, the cavity structure must be made less rigid so as to permit tuning with lesser mechanical effort.

One of the earlier lessons learned was that HF-etching glass is not good for resonators and for coating cavities with metal in general. Subsection 3.1.2 showed that metal deposited on HF-etched Pyrex was discontinuous due to wafer undercutting, so HF etching of glass was rejected as the main fabrication technology.

6.3 Future Work

There are several directions that future work on these cavity resonators could take. The complete tunable resonator shown in this thesis consisted of a silicon device attached to a bulky block and a large cylindrical piezoactuator. To make the resonator more portable and smaller, we can integrate the tuning actuator directly into the silicon device. We did in fact experiment with a 100 μm thin piezoelectric actuator pasted onto the silicon wafer. A first pass demonstrated a tuning range of 2 GHz to 5 GHz on a different device. Most notably, it was possible to move the tunable resonant peak to a frequency below that of the loop resonant peak. As of the writing of this thesis, no more experiments were performed. Continued work would be worth pursuing. Certainly, actuators other than those that are driven by piezoelectric materials can be used as well.

We can move beyond the actuator and include the a feedback loop. Currently, all tuning is done manually; the experimenter adjusts the capacitor gap width until the desired resonant frequency is attained. In order for the resonator to be useful in electronic systems, automatic tuning would be needed. Thus, there is a strong motivation to design integrated circuits that can determine the resonant frequency and control an actuator to move it to some desired frequency. Then, the resonator could be fully integrated into systems such as local oscillators or bandpass filters.

Although the large size of the silicon structures make precise corner compensation unnecessary, irregular convex corners affect the tank capacitance. Thus, in order to achieve a better match between theory and experiment, more sophisticated corner compensation techniques should be used.

In addition to the fabrication techniques described in this thesis, other technologies can be explored as well to lower fabrication cost and improve device reliability. For instance, instead of sputtering metal, we may consider metal stamping. Or, rather than using a wet etch to remove silicon to obtain a desired cavity, we may mold plastics or other materials to conform to the same cavity. We may look into novel processes such as printed electronics.

Finally, we may look into other tank designs and packaging techniques. As explained earlier in Section 2.2 beginning on Page 30, the presented model is of a magnetically-coupled resonator. A natural next step would be to construct an electrically-coupled resonator. Both the current configuration and the inverted version where the inductor is on the inside and the capacitor is on the outside should be examined. Figure 6-1 shows the resonator and wire connector packaged on a single chip. The upper photograph is the side with the slits; there are wires connecting the SMAs to the slits. The lower photograph is the side without the slits. The model shown is not tunable, but this can be combined with a piezo-actuator sealed on the side without slits to construct a tunable resonator. This version has not been tested, and one difficulty in doing so is that the experimenter cannot adjust the wire loops during testing.

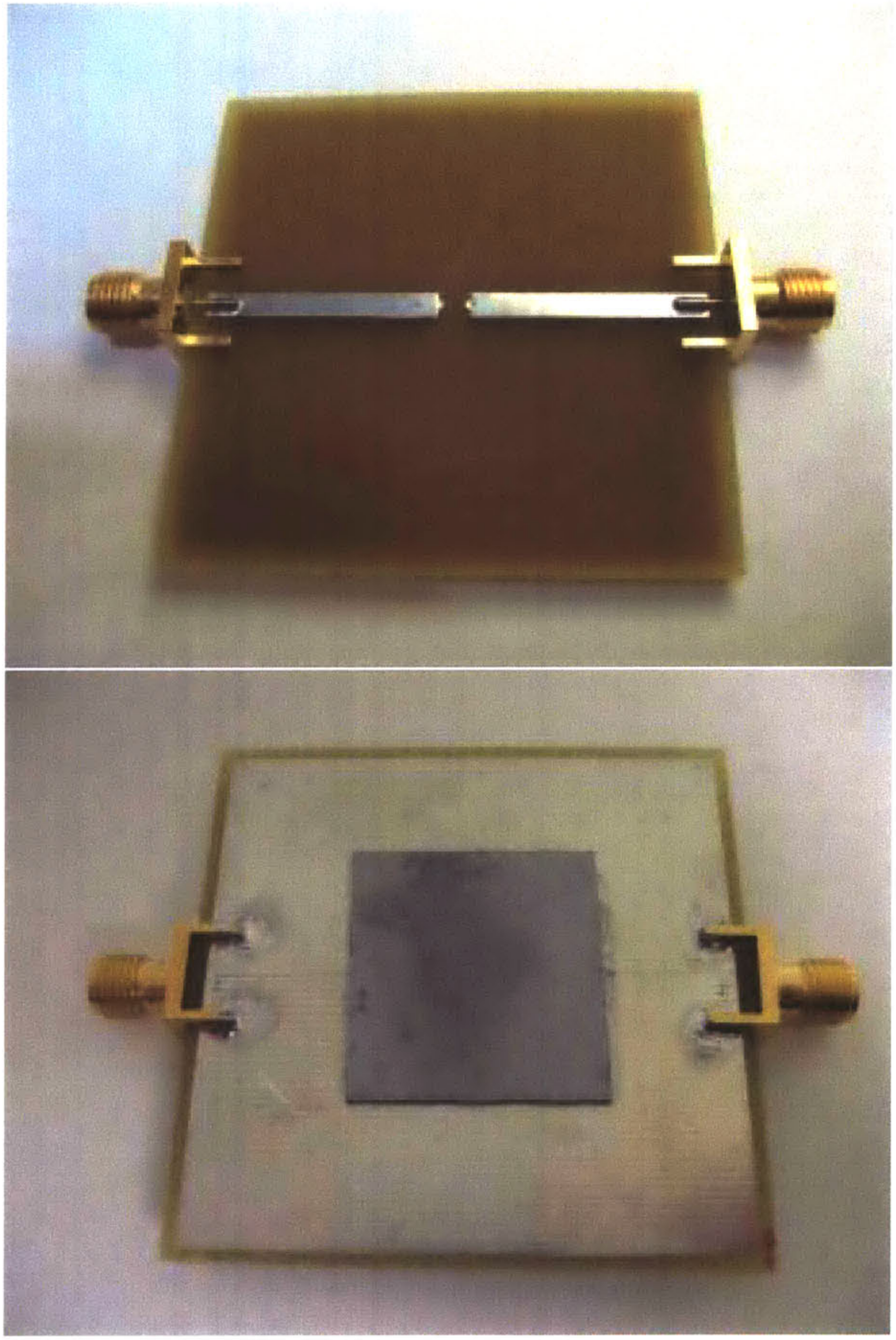

Figure 6-1: Resonator and connector packaged on a single chip.

Appendix A

Physical Dimensions of Resonator

Table A.1 shows the parameters of the five designed resonator types A – E, including physical dimensions, capacitance, inductance and resonant frequency. It is based on `wire_loop_resonator_dimensions_diary.txt`, which is shown in Section F.3 on Page 139. All resonators have a inductor depth of $D = 1000\,\mu\text{m}$ and a capacitor gap width of $d = 20\,\mu\text{m}$. Furthermore, all resonators have an additional 2.5-mm-wide rim to form the bonding surface. Thus, physical devices are 5 mm wider than the inductor width W. The design of these dimensions is described in Subsection 2.3.3 on Page 43.

Table A.1: Physical dimensions of resonator.

Type	**Capacitor width w (mm)**	**Inductor width W (mm)**	**Capacitance C (pF)**	**Inductance L (pH)**	**Resonant frequency (GHz)**
A	8.0	25.0	28.3	174	2.26
B	6.0	18.0	15.9	166	3.10
C	4.0	18.0	7.08	220	4.03
D	3.5	11.0	5.42	166	5.31
E	2.5	11.0	2.77	210	6.61

Appendix B

Chemical Formulas

The chemical formulas for the common names and abbreviations of chemicals used in Appendices C and D are given in Table B.1.

Table B.1: Chemical formulas and full names.

Term	**Chemical Formula / Full Name**
Acetone	$(CH_3)_2CO$
Aqua regia[1]	3:1 mixture of hydrochloric acid (HCl) and nitric acid (HNO_3)
BOE	Buffered oxide etch; 5:1 mixture of 40% ammonium fluoride (NH_4F) and 49% hydrofluoric acid (HF)
Cr-7	Chromium etchant; 9% $(NH_4)_2Ce(NO_3)_6$ + 6% $HClO_4$ + H_2O
HMDS	Hexamethyldisilazane; $NH(Si(CH_3)_3)_2$
Isopropanol	$(CH_3)_2CHOH$
Methanol	CH_3OH
Piranha	3:1 mixture of sulfuric acid (H_2SO_4) and hydrogen peroxide (H_2O_2)
Phosphoric acid	H_3PO_4
PR	Photoresist[2]

---

[1] Latin for "royal water." It should not be confused with *acquaragia*, which is commonly known as *turpentine* in English.

[2] Only the positive photoresist OCG 825 was used in fabrication.

Appendix C

Recipe for Etching Pyrex with Hydrofluoric Acid

The recipe shown in Table C.1 was used to etch Pyrex with hydrofluoric acid (HF). The chemical formulas for the common names and abbreviations used are given in Table B.1. All processing was done at the MIT Microsystems Technology Laboratories (MTL) Exploratory Materials Laboratory (EML). It is a modified form of a recipe suggested by Prof. Joel Voldman (MIT EECS). The results of this recipe is explained in Subsection 3.1.2 beginning on Page 46.

Table C.1: Recipe for etching Pyrex with hydrofluoric acid.

Step	**Machine**	**Recipe**	**Description**
1.1	Acid hood	Piranha (10 min), 50:1 HF dip (15 sec)	Clean wafers
1.2	Asher	Standard	Clean wafers (may be unnecessary)
2	Sputterer	200 W	Deposit 200 Å Cr and 1000 Å Au
3.1	HMDS	Standard	Coat HMDS to promote PR adhesion
3.2	Coater	1 μm thickness	Coat positive PR on front side
4	EV	2.0 s exposure	Pattern PR
5.1	Acid hood	Aqua regia dip (25 sec)	Etch Au
5.2	Acid hood	Cr-7 (20 sec)	Etch Cr
6	Acid hood	660:140:220 H_2O:HNO_3:HF (0.8 μm/min) or BOE or 50:1 49% HF:H_2O	Etch Pyrex
7	Rinse	Acetone/methanol/isopropanol	Strip PR
8	Acid hood	Repeat step 5	Strip metal

Appendix D

Device Process Flow

The process flow shown in Table D.1 was used to fabricate the resonators. Diagrams and explanations of the steps are contained in Sections 3.3 3.4 beginning on Page 51. The chemical formulas for the common names and abbreviations used are given in Table B.1. All processing was done at the MIT Microsystems Technology Laboratories (MTL), which consists of three labs: Technology Research Laboratory (TRL), Integrated Circuits Laboratory (ICL) and Exploratory Materials Laboratory (EML).

There are three types of wafers:

A. Top half of resonator

B. Bottom half of resonator

C. Capacitor gap show mask

All three wafers are processed simulatenously until Step 6. Only type A wafers, which will have a wire loop hole, go through Step 7 (backside processing). All wafers are placed in KOH in Step 8, but types A and B wafers are removed after 6 hours and 15 minutes (timed etch of 500 μm) while type C wafers are left in the bath to continue etching to completion to form a shadow mask wafer. All wafers are post KOH-cleaned in Step 9. Type C wafers are placed on top of type A wafers in Step 10 (RIE etch). In Step 11, Type A wafers are placed in KOH for 15 minutes (timed etch of 20 μm) followed up by a clean in Step 12. Types A and B wafers experience Steps 13, 14 and 15.

Table D.1: Device process flow.

Step	**Lab**	**Machine**	**Recipe**	**Description**
1	ICL	RCA hood	Standard	RCA clean
2	ICL	6D-Nitride	775°C, 200 mTorr, $SiCl_2H_2$ at 50 sccm and NH_3 at 150 sccm, 23 Å/min	Deposit 0.1 μm LPCVD nitride
3.1	TRL	HMDS	Standard	Coat HMDS to promote PR adhesion
3.2	TRL	Coater	1 μm thickness	Coat positive PR on front side
4	TRL	EV1	2.0 s exposure	Pattern PR
5	ICL	LAM490B	Nitride-on-Si, 1 min 45 sec etch time	RIE etch front side nitride
6	ICL	Asher	2 min	Remove PR
7	–	–	–	Repeat steps 3 – 6 for back side
8	ICL	KOH-TMAH hood	20% KOH, 83°C, 80 μm/hr	KOH etch to form inductor cavity
9	TRL	Acid hood	Piranha (10 min)	Post KOH clean
10	ICL	LAM490B	Nitride-on-Si with shadow mask, 1 min 45 sec etch time	RIE etch front side nitride to expose capacitor plateau
11	ICL	KOH-TMAH hood	20% KOH, 83°C, 80 μm/hr	KOH etch to form capacitor gap
12	TRL	Acid hood	Piranha (10 min)	Post KOH clean
13	TRL	Acid hood	Phosphoric acid at 150°C (30 min)	Remove nitride
14	ICL	Die saw	Wide blade	Cut up wafers into individual dies
15	EML	Acid hood	Ultrasound in DI H_2O (10 min), piranha (10 min), 10:1 HF (3 min), Ultrasound in DI H_2O (10 min)	Post-die saw clean
16	EML	Sputterer	200 W power	Deposit 0.1 μm Cr and 2 μm Au
17	EML	Acid hood	1 MPa of pressure at 300°C (60 min)	Thermocompression bonding

Appendix E

Masks

The layout of four transparency masks are given in the next few pages. Their design is explained in Section 3.5 beginning on Page 56. The first three are the ones used in resonator fabrication:

1. The front-side mask for creating the inductor,
2. The back-side mask for creating slits for the wire loop, and,
3. The mask for creating a wafer mask to create a capacitor gap.

Note the simple rectangular KOH corner compensation structures (see Subsection 3.5.2 beginning on Page 56) and the common mask alignment features (see Subsection 3.5.4 beginning on Page 60).

The fourth mask is the one used to test KOH corner compensation and gold coverage. Section 4.1 beginning on Page 63 explains the design.

E.1 Resonator Front-Side Mask

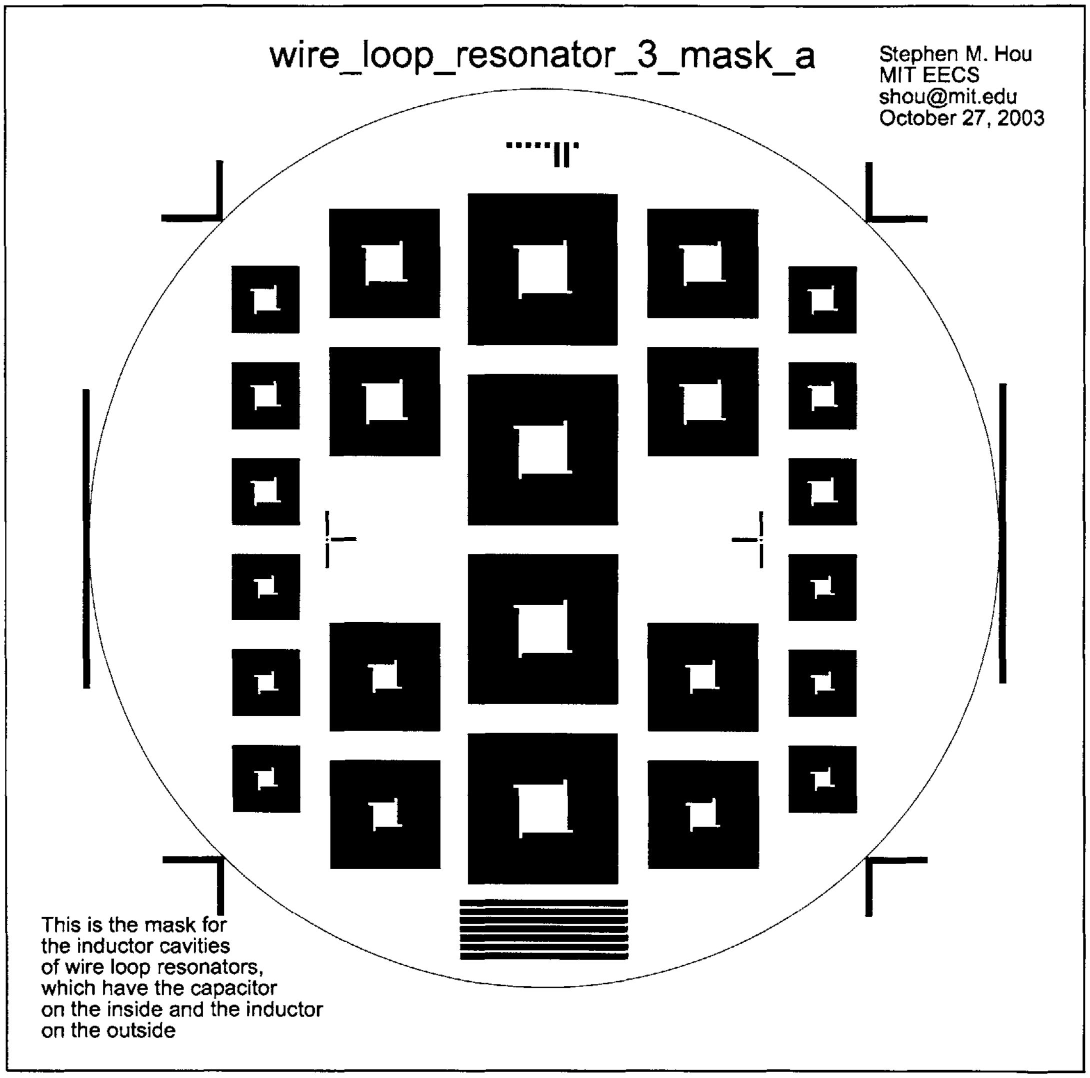

Figure E-1: Wire loop resonator front-side mask for 6” wafers.

E.2 Resonator Back-Side Mask

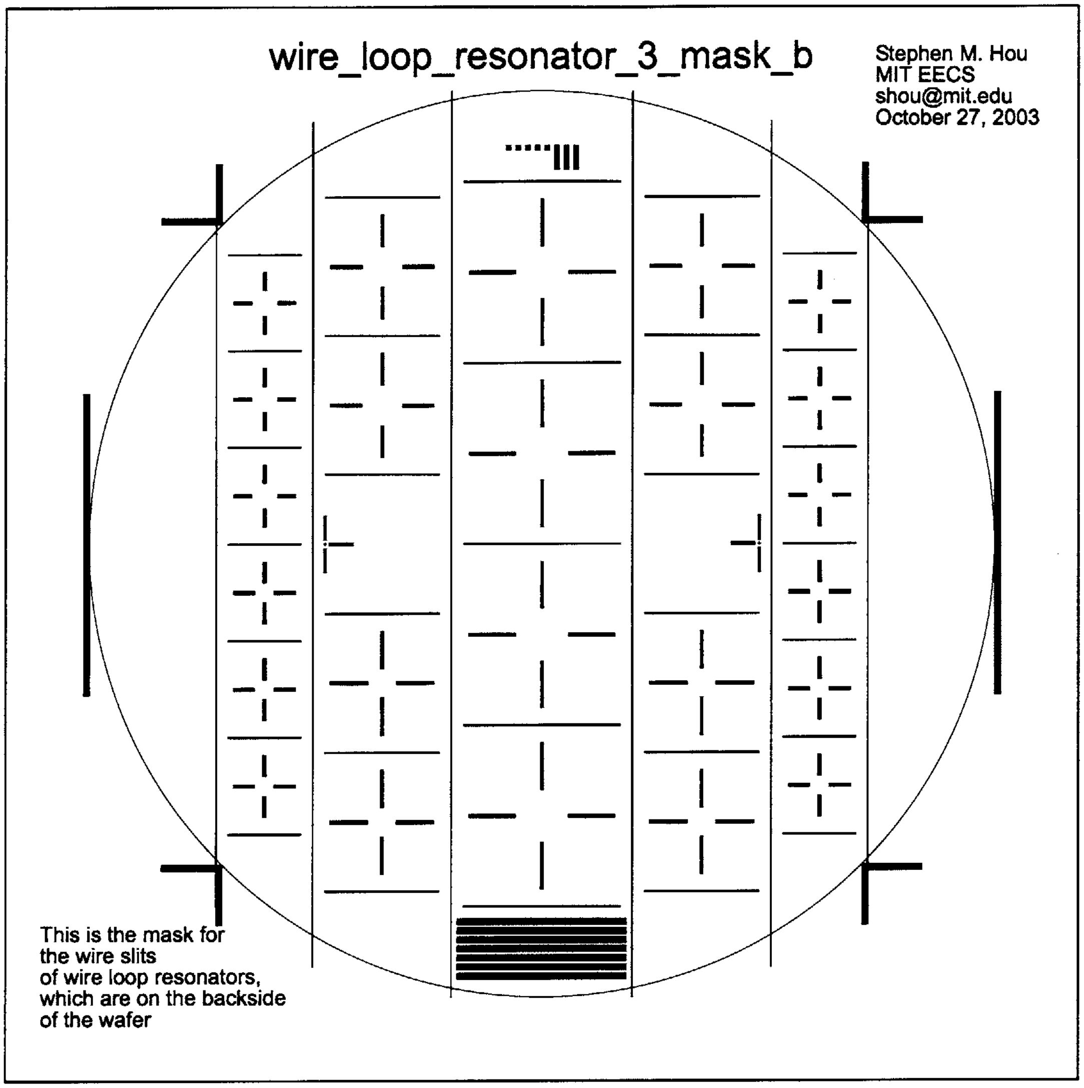

Figure E-2: Wire loop resonator back-side mask for 6” wafers.

E.3 Capacitor Etch Mask

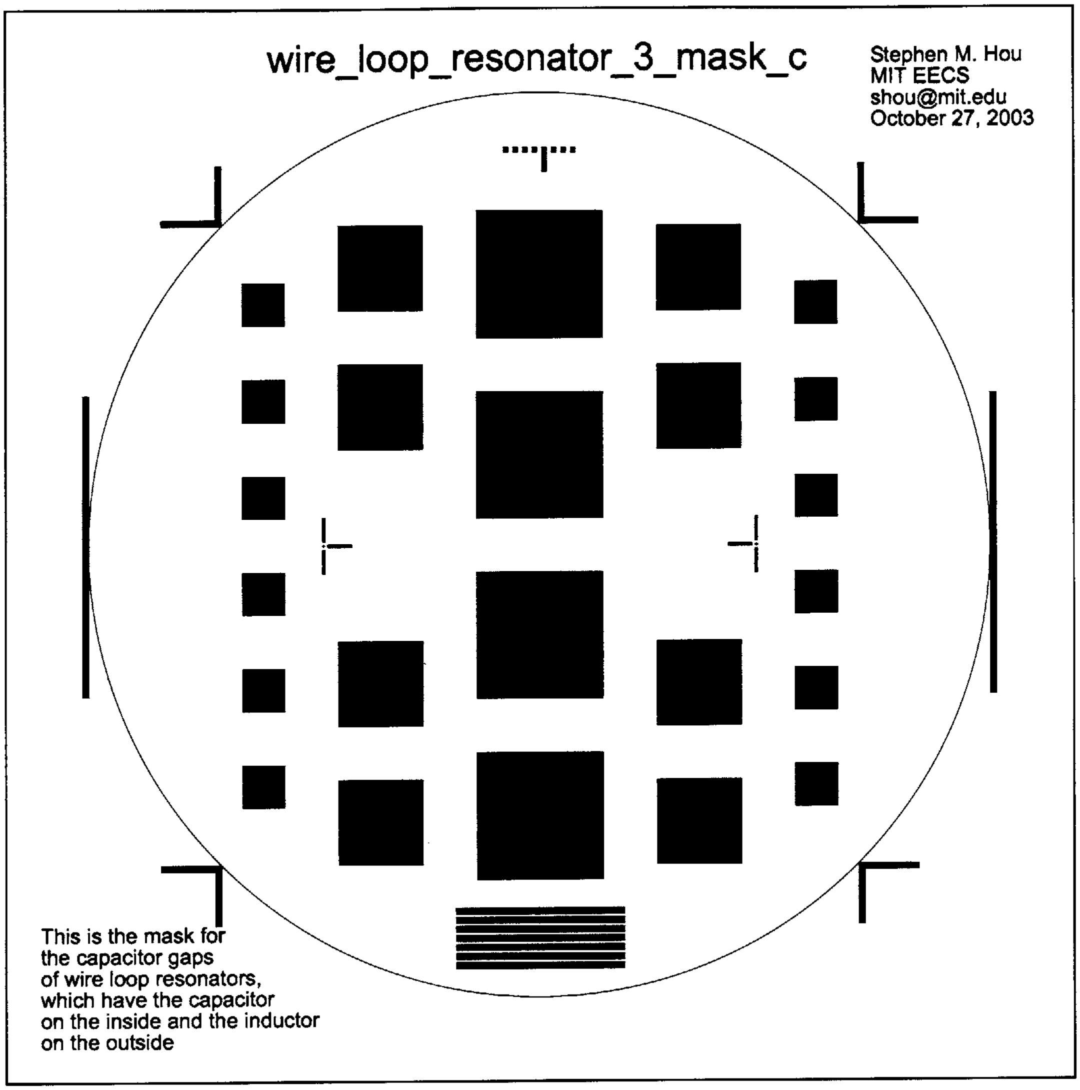

This is the mask for
the capacitor gaps
of wire loop resonators,
which have the capacitor
on the inside and the inductor
on the outside

Figure E-3: Wire loop resonator capacitor etch mask for 6” wafers.

E.4 KOH Corner Compensation and Gold Coverage Mask

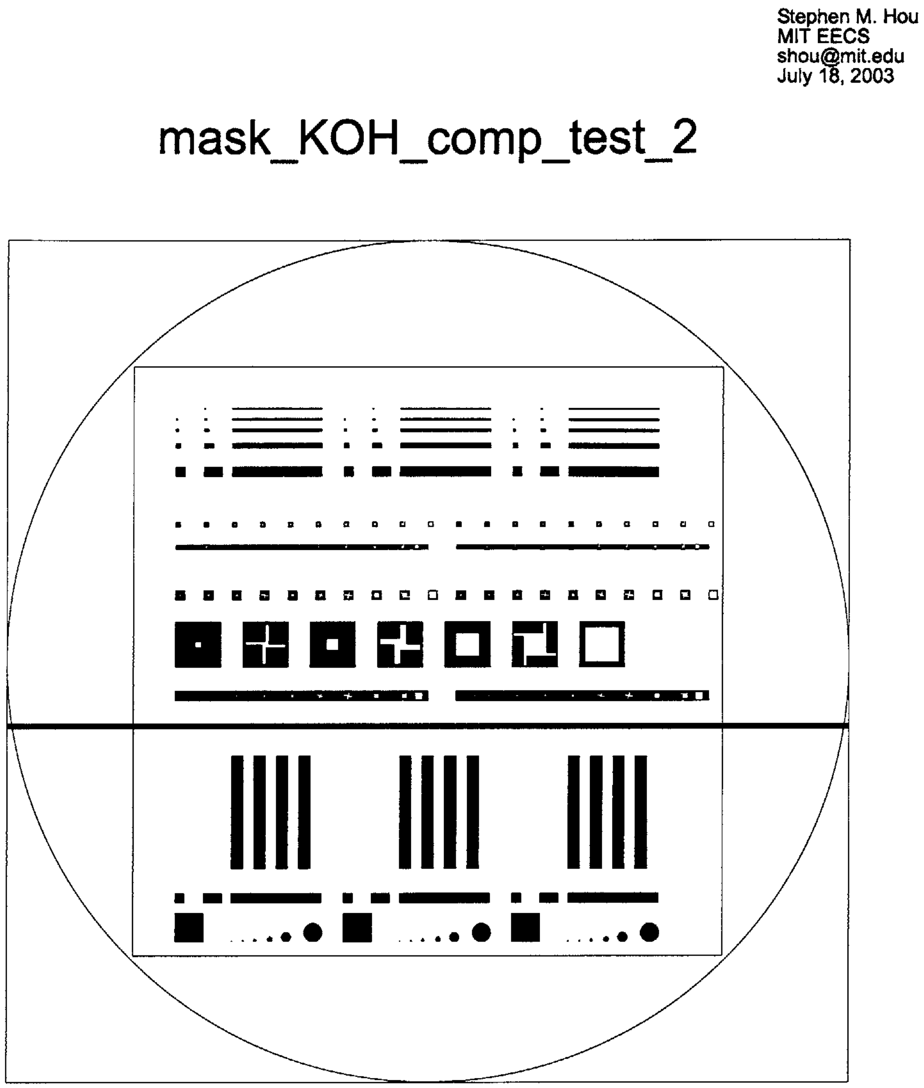

Figure E-4: KOH corner compensation and gold coverage mask for 6" wafers.

Appendix F

MATLAB Code and Diaries

F.1 `resistance_au_koh_trench.m`

The following code determines the voltage as a function of distance for the four-point probe test for the conductivity of gold across trenches and produced the plot in Figure 4-19 on Page 86.

```
% resistance_au_koh_trench.m

% Determine the resistance of 1 um gold deposited over trenches produced
% by KOH-etching <100> silicon

% last modified:   October 2, 2003



% Lot 1, wafer 2, strip #11
% basic characteristics

% raw data
I = [.10, .20, .30, .40, .50];
V = [.085, .161, .249, .325, .402];
[P, S] = polyfit(I, V, 1);
disp(strcat(’Measured resistance for is: ’, num2str(P(1)), ’ ohms’));

% physical dimensions
L = 0.02;      % m
w = 0.001;      % m
t_au = 1e-6;      % m
t_cr = 0.2e-6;      % m

% theoretical resistance
rho_au = 2.2e-8;      % ohm*m
```

```
rho_cr = 12.7e-8;     % ohm*m
R_au = rho_au*L/(w*t_au)
R_cr = rho_cr*L/(w*t_cr)
R_total_theoretical = (R_au^-1 + R_cr^-1)^-1


% Lot 1, wafer 2, strip #6
% more detailed infomation

% raw data
I = .50;     % A
V = [.032, .075, .117, .129, .149, .169, .184, .236, .247, .254, .268, .308, .318, .323, .344, .358, .368, .385];     % voltage
V = V - V(1);     % shift down by first measurement

% dimensions
tr_length = [2170, 1385, 690, 350, 175];     % length of Au on five strips, um
tr_space = [3400, 2400, 1600, 2000];     % spacing between strips, um
dx = [tr_length(1)/2, tr_length(1)/2, tr_space(1)/4, tr_space(1)/4, tr_space(1)/4, tr_space(1)/4, tr_length(2), tr_space(2)/3, ...
tr_space(2)/3, tr_space(2)/3, tr_length(3), tr_space(3)/2, tr_space(3)/2, tr_length(4), tr_space(4)/2, tr_space(4)/2, tr_length(5)];
% spacing between points on strip, um
x = [0, cumsum(dx)];     % distance along strip, um

% adjust distances to account for the probe being not exactly at the edge
% about 300 um
x_correction_scalar = 300;     % um
x_correction = [-x_correction_scalar, 0, x_correction_scalar, 0, 0, 0, -x_correction_scalar, x_correction_scalar, 0, 0, ...
 -x_correction_scalar, x_correction_scalar, 0, -x_correction_scalar, x_correction_scalar, 0, -x_correction_scalar, x_correction_scalar];
x = x + x_correction;

% theoretical voltage based on dimensions,
% also need to make Au thinner on trench walls
t_trench = t_au/sqrt(3);     % Au thickness on walls, um
t_vary = [t_au, (675*t_trench+410*t_au)/1085, (675*t_trench+410*t_au)/1085, t_au, t_au, t_au, t_au, t_trench, t_au, t_au, t_au, ...
t_trench, t_au, t_au, t_trench, t_au, t_au, t_trench, t_au];     % thickness of each segment, um
for J=1:length(dx)
     % calculate the increment voltages, be careful of adjustments of dx
     xt_center = dx(J)/t_vary(J+1);     % length over thickness, main part
     if (x_correction(J) < 0)
       xt_low = -x_correction(J)/t_vary(J);
     else
       xt_low = -x_correction(J)/t_vary(J+1);
     end
     if (x_correction(J+1) < 0)
       xt_high = x_correction(J+1)/t_vary(J+1);
     else
       xt_high = x_correction(J+1)/t_vary(J+2);
     end
     dV_theo(J) = 1e-6*I*rho_au/w*(xt_center + xt_low  + xt_high);     % voltage across each segment
end
V_theo = [0, cumsum(dV_theo)];     % cumulative voltage at each point
V_theo_scale = 1.8*V_theo;     % scale to meet measured voltage

% plot
close all;
figure;
plot(x, V, '*-');
```

```
grid on;
%title('Voltage vs. Distance Along Gold Strip (Wafer 2, Strip 6) with 0.5 A current');
xlabel('Distance Along Strip (\mu m)');
ylabel('Voltage (V)');
hold on;
% highlight edges
x_edges = [x(1), x(3), x(7), x(8), x(11), x(12), x(14), x(15), x(17), x(18)];
V_edges = [V(1), V(3), V(7), V(8), V(11), V(12), V(14), V(15), V(17), V(18)];
plot(x, V_theo, 'gs-.');
plot(x, V_theo_scale, 'r^--');
stem(x_edges, V_edges, 'ko')
legend('Actual measurements', 'Theoretical voltage', 'Theoretical voltage scaled by 1.8', 'Edge of regions', 2);
```

F.2 `wire_loop_resonator_dimensions.m`

The following code calculates the theoretical capacitance, inductance and resonant frequency for five sets of physical dimensions based on the analysis in Subsection 2.3.2 beginning on Page 39. It also determines the sizes of the slits for the wire loop and the minimum width of the squares on the wafer mask that creates the capacitor gaps. The results are contained in `wire_loop_resonator_dimensions_diary.txt`, which is in the next section.

```
% wire_loop_resonator_dimensions.m

% Determine the dimensions of a wire loop resonator and the
% mask dimensions to produce the desired frequencies




% constants, all SI
e0 = 8.85418781762e-12;
u0 = 1.25663706144e-6;
phi = 54.7*pi/180;     % KOH etching angle

% fixed dimensions, m
d = 20e-6;     % capacitor gap
D = 1000e-6;     % inductor gap

% other dimensions
w = [8000, 6000, 4000, 3500, 2500]*1e-6;     % capacitor width
y = [8500, 6000, 7000, 3750, 4250]*1e-6;     % inductor width
W = 2*y + w;     % total width
w_mm = w*1000
y_mm = y*1000
W_mm = W*1000

% frequency
C = e0*w.^2/d;
L = u0*D*(W - w - D/tan(phi))./(8*w + pi*(W - w));
C_pF = C*1e12
L_pH = L*1e12
f_Hz = 1./(2*pi*sqrt(L.*C))

% slit lengths
% there are the same length as bottom of trench, so the angled KOH etch will
% make the bottom of the mask and the
% resulting slits be slightly smaller than trench
slit_lengths_mm = y_mm - D*1000/sqrt(2)

% width of capacitor mask
% this is a minimum
T_mm = 625*1e-3;     % wafer thickness
capacitor_mask_width_mm = w_mm + T_mm*sqrt(2)
```

F.3 wire_loop_resonator_dimensions_diary.txt

The following text is the output produced by `wire_loop_resonator_dimensions.m` from the previous section. It contains the theoretical capacitance, inductance and resonant frequency for five sets of physical dimensions based on the analysis in Subsection 2.3.2 beginning on Page 39. It also determines the sizes of the slits for the wire loop and the minimum width of the squares on the wafer mask that creates the capacitor gaps.

```
>> wire_loop_resonator_dimensions

w_mm =

    8.0000    6.0000    4.0000    3.5000    2.5000


y_mm =

    8.5000    6.0000    7.0000    3.7500    4.2500


W_mm =

   25.0000   18.0000   18.0000   11.0000   11.0000


C_pF =

   28.3334   15.9375    7.0834    5.4232    2.7669


L_pH =

  174.3769  165.5781  219.8298  165.5296  209.6558


f_Hz =

   1.0e+09 *

    2.2643    3.0982    4.0333    5.3120    6.6080


slit_lengths_mm =

    7.7929    5.2929    6.2929    3.0429    3.5429


capacitor_mask_width_mm =

    8.8839    6.8839    4.8839    4.3839    3.3839
```

F.4 bdwidth_win.m

The following code is the auxiliary function that returns the lower and upper frequencies that form the boundaries of the bandwidth of a given magnitude vector and its corresponding frequency vector. It searches within a band whose indices are input parameters. The function is called by `C1_and_loop_plot_freqresp.m`, which follows on the next page.

```
% bdwidth_win.m



% Function that returns the lower and upper frequencies that form the
% boundaries of the bandwidth of a given magnitude vector and its corresponding frequency vector.

% Windowed version: only searches within a band, and band is defined by index

function [freq_peak, freq_low, freq_high, Q] = bdwidth_win(freq, abs_mag, lim_low, lim_high)

% seek peak
mag_max = freq(lim_low);
index_max = lim_low;
for I = lim_low:lim_high,
  if ((abs_mag(I) > mag_max) & (abs_mag(I-100) < abs_mag(I)))
     mag_max = abs_mag(I);
     index_max = I;
  end
end
freq_peak = freq(index_max);

% seek freq_low
I = index_max;
while (abs_mag(I) >= mag_max/sqrt(2)),
  I = I - 1;
end
freq_low = freq(I+1);

% seek freq_
I = index_max;
while (abs_mag(I) >= mag_max/sqrt(2)),
  I = I + 1;
end
freq_high = freq(I-1);

Q = freq_peak/(freq_high - freq_low);
```

F.5 C1_and_loop_plot_freqresp.m

The following code produced the plots in Figures 5-5, 5-6, 5-7 and 5-8 in Section 5.3 beginning on Page 99. It plots the frequency response of device C1 and the wire loop as the device is tuned with the piezoelectric actuator. The resonant frequencies are stored in the vector `res_freq` with the FWHM frequencies in the vectors `freq_low` and `freq_high`. The quality factors Q are stored in the vector `Qv`. The auxiliary function `bdwidth_win.m` does these calculations and its code is provided on the previous page. The gap change `dx`, `res_freq` and `Qv` are saved in a file named `C1_resfreq_Q.mat`. The diary of this code, which produces the contents of `C1_resfreq_Q.mat`, is given in the next section.

```
% C1_and_loop_plot_freqresp.m

% Plots the frequency response of device C1 and wire loop as the device is
% tuned with the piezoelectric actuator.  The resonant frequencies are
% stored in the vector res_freq with the FWHM frequencies in the vectors
% freq_low and freq_high.  The quality factors Q are stored in the vector Qv.
% The auxiliary function bdwidth_win.m does these calculations.  The gap change
% dx, res_freq and Qv are saved in a file named C1_resfreq_Q.mat.

% Testing was done on 2004.03.08



% start and stop
start_index = 1;
stop_index = 16001;     % 16001 is the default

% only the loop
data = load('loop_0308_1.dat');
freq = data(start_index:stop_index, 1);     % frequency, Hz
freqGHz = freq*1e-9;     % frequency, GHz
imp_re = data(start_index:stop_index, 2);     % real impedance, Ohm
imp_im = data(start_index:stop_index, 3);     % imag impedance, Ohm
imp = imp_re + j*imp_im;     % complex impedance, Ohm
imp_mag = abs(imp);     % magnitude of impedance
imp_pha = unwrap(angle(imp))/pi;     % phase of impedance
close all;
figure;
subplot(2, 1, 1);
semilogy(freqGHz, imp_mag);
grid on;
xlabel('Frequency (GHz)');
ylabel('Impedance Magnitude (\Omega)');
subplot(2, 1, 2);
plot(freqGHz, 180*imp_pha);
grid on;
```

```
xlabel('Frequency (GHz)');
ylabel('Impedance Phase (Degrees)');



% device C1

% initialize
clear data;
res_freq = [];
freq_low = [];
freq_high = [];
Qv = [];

% data files
f(1,:) = 'device_C1_0308_piezo_000p0.dat';
f(2,:) = 'device_C1_0308_piezo_010p0.dat';
f(3,:) = 'device_C1_0308_piezo_020p0.dat';
f(4,:) = 'device_C1_0308_piezo_030p0.dat';
f(5,:) = 'device_C1_0308_piezo_040p0.dat';
f(6,:) = 'device_C1_0308_piezo_050p0.dat';
f(7,:) = 'device_C1_0308_piezo_060p0.dat';
f(8,:) = 'device_C1_0308_piezo_070p0.dat';
f(9,:) = 'device_C1_0308_piezo_080p0.dat';
f(10,:) = 'device_C1_0308_piezo_090p0.dat';
f(11,:) = 'device_C1_0308_piezo_100p0.dat';
f(12,:) = 'device_C1_0308_piezo_110p0.dat';
f(13,:) = 'device_C1_0308_piezo_120p0.dat';
f(14,:) = 'device_C1_0308_piezo_130p0.dat';
f(15,:) = 'device_C1_0308_piezo_139p3.dat';

% process data
for J = 1:size(f,1),
data = load(f(J,:));
freq = data(start_index:stop_index, 1);     % frequency, Hz
freqGHz = freq*1e-9;     % frequency, GHz
imp_re = data(start_index:stop_index, 2);     % real impedance, Ohm
imp_im = data(start_index:stop_index, 3);     % imag impedance, Ohm
imp = imp_re + j*imp_im;     % complex impedance, Ohm
imp_mag = abs(imp);     % magnitude of impedance
imp_pha = unwrap(angle(imp))/pi;     % phase of impedance
figure;
subplot(2, 1, 1);
semilogy(freqGHz, imp_mag, 'b');
grid on;
xlabel('Frequency (GHz)');
ylabel('Impedance Magnitude (\Omega)');
subplot(2, 1, 2);
plot(freqGHz, 180*imp_pha);
grid on;
xlabel('Frequency (GHz)');
ylabel('Impedance Phase (Degrees)');
[freq_peak, freq_l, freq_h, Q] = bdwidth_win(freqGHz, imp_mag, 4200, 10000);
res_freq = [res_freq; freq_peak];
freq_low = [freq_low; freq_l];
freq_high = [freq_high; freq_h];
```

```
Qv = [Qv; Q];
end

% list data
voltage = [0; 10; 20; 30; 40; 50; 60; 70; 80; 90; 100; 110; 120; 130; 139.3];
dx = voltage/150*15;     % um

% save data in file C1_resfreq_Q.mat
save C1_resfreq_Q dx res_freq Qv;

% 000 and 139.3 superimposed
data = load('device_C1_0308_piezo_000p0.dat');
freq = data(start_index:stop_index, 1);     % frequency, Hz
freqGHz = freq*1e-9;     % frequency, GHz
imp_re = data(start_index:stop_index, 2);     % real impedance, Ohm
imp_im = data(start_index:stop_index, 3);     % imag impedance, Ohm
imp = imp_re + j*imp_im;     % complex impedance, Ohm
imp_mag = abs(imp);     % magnitude of impedance
imp_pha_1 = unwrap(angle(imp))/pi;     % phase of impedance
figure;
semilogy(freqGHz(1:9601), imp_mag(1:9601), 'b');
hold on;
data = load('device_C1_0308_piezo_139p3.dat');
freq = data(start_index:stop_index, 1);     % frequency, Hz
freqGHz = freq*1e-9;     % frequency, GHz
imp_re = data(start_index:stop_index, 2);     % real impedance, Ohm
imp_im = data(start_index:stop_index, 3);     % imag impedance, Ohm
imp = imp_re + j*imp_im;     % complex impedance, Ohm
imp_mag = abs(imp);     % magnitude of impedance
imp_pha_2 = unwrap(angle(imp))/pi;     % phase of impedance
semilogy(freqGHz(1:9601), imp_mag(1:9601), 'r');
grid on;
xlabel('Frequency (GHz)');
ylabel('Impedance Magnitude (\Omega)');
%legend('No Actuation', '13.9 um Actuation');
figure;
plot(freqGHz(1:9601), 180*imp_pha_1(1:9601), 'b');
hold on;
plot(freqGHz(1:9601), 180*imp_pha_2(1:9601), 'r');
grid on;
xlabel('Frequency (GHz)');
ylabel('Impedance Phase (Degrees)');

% 000 and 139.3 separate
data = load('device_C1_0308_piezo_000p0.dat');
freq = data(start_index:stop_index, 1);     % frequency, Hz
freqGHz = freq*1e-9;     % frequency, GHz
imp_re = data(start_index:stop_index, 2);     % real impedance, Ohm
imp_im = data(start_index:stop_index, 3);     % imag impedance, Ohm
imp = imp_re + j*imp_im;     % complex impedance, Ohm
imp_mag = abs(imp);     % magnitude of impedance
imp_pha_1 = unwrap(angle(imp))/pi;     % phase of impedance
figure;
semilogy(freqGHz(1:9601), imp_mag(1:9601), 'b');
grid on;
xlabel('Frequency (GHz)');
```

```
ylabel('Impedance Magnitude (\Omega)');
figure;
data = load('device_C1_0308_piezo_139p3.dat');
freq = data(start_index:stop_index, 1);     % frequency, Hz
freqGHz = freq*1e-9;     % frequency, GHz
imp_re = data(start_index:stop_index, 2);     % real impedance, Ohm
imp_im = data(start_index:stop_index, 3);     % imag impedance, Ohm
imp = imp_re + j*imp_im;     % complex impedance, Ohm
imp_mag = abs(imp);     % magnitude of impedance
imp_pha_2 = unwrap(angle(imp))/pi;     % phase of impedance
semilogy(freqGHz(1:9601), imp_mag(1:9601), 'b');
grid on;
xlabel('Frequency (GHz)');
ylabel('Impedance Magnitude (\Omega)');
%legend('No Actuation', '13.9 um Actuation');

% display data
disp('[dx, res_freq, Qv] (i.e. gap reduction, res frequency, measured Q) is:')
[dx, res_freq, Qv]
```

F.6 `C1_and_loop_plot_freqresp_diary.txt`

The following is the diary produced by `C1_and_loop_plot_freqresp.m`, which is in the previous section. It is the contents of the file `C1_resfreq_Q.mat`, which contains vectors for the capacitor gap changes `dx`, the corresponding resonant frequencies `res_freq` and quality factors `Qv`.

```
>> C1_and_loop_plot_freqresp
[dx, res_freq, Qv] (i.e. gap reduction, res frequency, measured Q) is:

ans =

         0    3.9730  113.0097
    1.0000    3.8361  129.9006
    2.0000    3.7752  136.5040
    3.0000    3.6964  148.7847
    4.0000    3.6172  145.5960
    5.0000    3.5117  162.8586
    6.0000    3.4020  168.7850
    7.0000    3.2867  179.7888
    8.0000    3.1653  192.9363
    9.0000    3.0598  197.8177
   10.0000    2.9520  203.1540
   11.0000    2.8414  224.5106
   12.0000    2.7364  224.5164
   13.0000    2.6347  224.8411
   13.9300    2.5405  246.3366
```

F.7 C1_capgap.m

The following code produced the plots in Figure 5-9 on Page 105. It plots the resonant frequency as a functions of gap change and finds the least-squares fit to obtain the nominal capacitor gap width. It diary is in the following section.

```
% C1_capgap.m

% Plots the resonant frequency vs. gap change and finds the least-squares fit
% to obtain the nominal capacitor gap width.




% load data produced by C1_and_loop_plot_freqresp.m.
% It contains dx (gap changes), res_freq (the resonant frequecies) and
% Qv (quality factors)
load('C1_resfreq_Q');

% least-squares fit of resonance vs. capacitor gap change
freqfunc = inline('param(1)*sqrt(param(2) - dx)', 'param', 'dx');
param = lsqcurvefit(freqfunc, [0.834, 23], dx, res_freq)
K = param(1)    % estimated K
x0 = param(2)     % estimated unactuated cap gap
res_freq_fit = param(1)*sqrt(x0 - dx)
dx_all = linspace(0, x0, 10001);
res_freq_fit_all = abs(param(1)*sqrt(x0 - dx_all));
dx_part = linspace(0, 14, 10001);
res_freq_fit_part = abs(param(1)*sqrt(x0 - dx_part));

% show res vs. gap with fit
close all;
figure;
plot(dx, res_freq, '*');
hold on;
plot(dx_part, res_freq_fit_part, 'r-.');
grid on;
xlabel('Capacitor Gap Width Reduction (\mum)');
ylabel('Resonant Frequency (GHz)');

% show res vs. gap with fit, all the way down to zero freq
figure;
plot(dx, res_freq, '*');
hold on;
xlabel('Capacitor Gap Width Reduction (\mum)');
ylabel('Resonant Frequency (GHz)');
plot(dx_all, res_freq_fit_all, 'r-.');
grid on;
legend('Measured', 'Least-squares fit');

% save data
save C1_lse_vars K x0 res_freq_fit dx_all res_freq_fit_all dx_part res_freq_fit_part;
```

F.8 C1_capgap_diary.txt

The following is the diary produced by `C1_capgap.m`, which is in the previous section.

```
>> diary on
>> C1_capgap
Optimization terminated successfully:
 First-order optimality less than OPTIONS.TolFun, and no negative/zero curvature detected

param =

    0.8188   23.2276


K =

    0.8188


x0 =

   23.2276


res_freq_fit =

    3.9464
    3.8605
    3.7727
    3.6827
    3.5905
    3.4959
    3.3987
    3.2986
    3.1953
    3.0886
    2.9781
    2.8633
    2.7437
    2.6187
    2.4968
```

F.9 C1_model.m

The following code determined the circuit parameters described in Section 5.6 beginning on Page 5.6 and produced the plots in Figures 5-12 and 5-13 beginning on Page 111.

```
% C1_model.m

% Determines the circuit parameters from the poles and zeros of the
% impedance.



close all;
clear all;

Data = dlmread('device_C1_0308_piezo_000p0.dat',',');       % read data file

F  = Data(:,1);                                             % extract frequency
ZR = Data(:,2);                                             % extract real impedance
ZI = Data(:,3);                                             % extract imag impedance
Z  = ZR + j*ZI;                                             % compute complex impedance

W = 2*pi*F;                                                 % compute radian frequency

% obtain pole/zero locations by observation
WPL = 2*pi*2.2080e9;                                        % input lower pole from 000 data
WZL = 2*pi*3.9610e9;                                        % input lower zero from 000 data
WPH = 2*pi*3.9695e9;                                        % input higher pole from 000 data
WZH = 2*pi*7.0000e9;                                        % input higher zero from 000 data
G = 0.770e-8;                                               % input low freq L from 000 data

% calculate time constants
TZL = WZL^-2;                                               % compute squared time constant
TZH = WZH^-2;                                               % compute squared time constant
TPL = WPL^-2;                                               % compute squared time constant
TPH = WPH^-2;                                               % compute squared time constant

% determine the M parameters
M1 = TZL*TZH*G/TPL/TPH;                                     % intermediate fitting parameter
M4 = TPL+TPH-(G-M1)*TPL*TPH/(G*(TZL+TZH)-M1*(TPL+TPH));     % intermediate fitting parameter
M5 = TPL*TPH/M4;                                            % intermediate fitting parameter
M3 = (TPL+TPH-M4)/M5;                                       % intermediate fitting parameter
M2 = (G-M1)/M3;                                             % intermediate fitting parameter

% determine the circuit parameters
LL1 = M1                                                    % compute LL1
LL2 = M2                                                    % compute LL2
LT_lossless_unityalpha  = M2*(M3-1)                         % compute LT
CT_lossless_unityalpha  = M4/LT_lossless_unityalpha         % compute CT
CP  = M5/LL2                                                % compute CP

% given parameters
```

```
CT = 6.11e-12
LT = 266e-12

% guess other parameters
a = 0.431;                                                 % ratio of inductor areas
RLT = 22.4e-3;                                             % input series resistance
RCT = 0e-3;                                                % input series resistance
RP = 11000;                                                % input parallel resistance

WT = 1/sqrt(LT*CT);                                        % compute radian tank frequency
FT = WT/2/pi                                               % compute tank frequency
QT = 1/((RLT*sqrt(WT/WPH)/WT/LT)+(WT*CT*RCT*sqrt(WT/WPH)))  % compute tank Q

RLT = RLT*sqrt(W/WPH);                                     % scale tank inductor resistor
RCT = RCT*sqrt(W/WPH);                                     % scale tank capacitor resistor

% compute impedance
A1 = j*W*a*LT + RLT;                                       % tank inductor and series resistor
A2 = j*W*(1-a)*LT + 1./(j*W*CT) + RCT;                     % tank capacitor and series resistor
A3 = j*W*LL2.*RP./(j*W*LL2+RP);                            % loop inductor with parallel resistor
A4 = 1./(j*W*CP);                                          % loop capacitor
A5 = j*W*LL1;                                              % loop inductor
A = A3+A1.*A2./(A1+A2);                                    % compute impedance
A = A5+A.*A4./(A+A4);                                      % compute impedance

figure;
semilogy(F,abs(Z),'b');                                    % plot measured impedance magnitude
hold on;
semilogy(F,abs(A),'r-.');                                    % plot fitted impedance magnitude
xlabel('Frequency (Hz)');
ylabel('Impedance Magnitude (Ohms)');
title('Cavity Resonator (000 V)');
grid on;
legend('Measured', 'Modeled');

figure;
plot(F,unwrap(angle(Z))*180/pi,'b');                       % plot measured impedance phase
hold on;
plot(F,unwrap(angle(A))*180/pi,'r-.');                       % plot fitted impedance phase
xlabel('Frequency (Hz)');
ylabel('Impedance Phase (Degrees)');
grid on;
legend('Measured', 'Modeled');

figure;
V = [0 30 70 110 139];
C = [32.9 38.05 48.22 64.87 82.1];
plot(V,C,'*');
grid on;
xlabel('Piezo Actuator Voltage (V)');
ylabel('Estimated Tank Capacitance (pF)');
```

F.10 `C1_model_diary.txt`

The following is the diary of `C1_model.m`, which is in the previous section.

```
>> C1_model

LL1 =

   7.6940e-10


LL2 =

   6.8812e-09


LT_lossless_unityalpha =

   4.9347e-11


CT_lossless_unityalpha =

   3.2917e-11


CP =

   7.4725e-13


CT =

   6.1100e-12


LT =

   2.6600e-10


FT =

   3.9478e+09


QT =

  295.3662
```

F.11 C1_plot_resfreq_q.m

The following code produced the plots in Figures 5-14 and 5-15 in Section 5.6 beginning on Page 113.

```
% C1_plot_resfreq_q.m

% Plots the theoretical resonant frequency and Q as functions of frequency
% based on the model from C1_model.m



% load data produced by C1_and_loop_plot_freqresp.m and C1_capgap.m
load(’C1_resfreq_Q’);
load(’C1_lse_vars’);

% Now, we show it with an *independent* calculation of resfreq using the
% fitted nominal gap size, inductor, cap, etc.
L = 266e-12;
C0 = 6.11e-12;
%C0 = 1/(L*(2*pi*res_freq(1)*1e9)^2);     % unactuated capacitance
res_freq_pred = 1e-9*1./(2*pi*sqrt(L*C0*x0./(x0 - dx_part)));    % predicted resonant frequency
close all;
figure;
plot(dx, res_freq, ’*’);
hold on;
plot(dx_part, res_freq_pred, ’r-.’);
axis([0, 14, 2.4, 4]);
grid on;
xlabel(’Capacitor Gap Width Reduction (\mum)’);
ylabel(’Resonant Frequency (GHz)’);
legend(’Measured’, ’Predicted’);

% Q vs. capacitor gap change
figure;

plot(dx, Qv, ’*’);
grid on;
xlabel(’Capacitor Gap Width Reduction (\mum)’);
ylabel(’Quality Factor (Q)’);

% add estimated
hold on;
%e0 = 8.854e-12;
%C = (e0*(.004)^2)./(23.2276e-6 - dx*1e-6)
     C = C0*x0./(x0 - dx);
R0 = 4.2e-3;  %%% get from Lang
alpha = 0.433;
f0 = 1/(2*pi*sqrt(L*C(1)));
RT = (R0/alpha^2)*sqrt(res_freq*1e9/f0);
%RT = (R0/alpha^2)*sqrt(2*pi./(f0*sqrt(L*C)));
QT = (1./RT).*sqrt(L./C);    % estimated quality factor
```

```
plot(dx, QT, 'sr');
legend('Measured', 'Estimated', 4);

% display data
disp('[dx, res_freq, Qv, QT] (i.e. gap reduction, res frequency, measured Q, estimated Q) is:')
[dx, res_freq, Qv, QT]
```

F.12 `C1_plot_resfreq_q_diary.txt`

The following is the diary of `C1_plot_resfreq_q.m`, which is in the previous section.

```
>> C1_plot_resfreq_q
[dx, res_freq, Qv, QT] (i.e. gap reduction, res frequency, measured Q, estimated Q) is:

ans =

         0    3.9730  113.0097  293.6084
    1.0000    3.8361  129.9006  292.2978
    2.0000    3.7752  136.5040  287.9432
    3.0000    3.6964  148.7847  284.0575
    4.0000    3.6172  145.5960  279.9632
    5.0000    3.5117  162.8586  276.6488
    6.0000    3.4020  168.7850  273.2544
    7.0000    3.2867  179.7888  269.8173
    8.0000    3.1653  192.9363  266.3369
    9.0000    3.0598  197.8177  261.8425
   10.0000    2.9520  203.1540  257.0419
   11.0000    2.8414  224.5106  251.8998
   12.0000    2.7364  224.5164  245.9671
   13.0000    2.6347  224.8411  239.2468
   13.9300    2.5405  246.3366  232.3017
```

Bibliography

[1] Tayo Akinwande. Lecture notes on Etch and Pattern Transfer I, 6.152J/3.155J, Fall 2003. Department of Electrical Engineering and Computer Science, Massachusetts Institute of Technology, Cambridge, Massachusetts.

[2] Tayo Akinwande. Lecture notes on Etch and Pattern Transfer II, 6.152J/3.155J Fall 2003. Department of Electrical Engineering and Computer Science, Massachusetts Institute of Technology, Cambridge, Massachusetts.

[3] Ron Besser. Bulk micromaching of silicon: Wet etching. lecture notes from Chemical Engineering 702: Short course on MEMS and nanotechnology, June 2002.

[4] R.L. Borwick, III, P.A. Stupar, J. DeNatale, R. Anderson, C. Tsai, and K. Garrett. A high q, large tuning range, tunable capacitor for RF aapplications. In *The Fifteenth IEEE International Conference on Microelectromechanical Systems, 2002*, pages 669–672, January 2002.

[5] Stephen A. Campbell. *The Science and Engineering of Microelectronic Fabrication.* Oxford University Press, New York, New York, 1996.

[6] Kristin M. Carr, Vikash Gilja, Wesley M. Gifford, Stanley S. Hong, Stephen M. Hou, and Sy Bor Wang. Tutorial notes for 6.003 Signals and Systems, spring 2004. Department of Electrical Engineering and Computer Science, Massachusetts Institute of Technology, Cambridge, Massachusetts.

[7] Tah-Hsiung Chu. Lecture notes on Electric Circuits I and II, chapter 8, September 2003. Department of Electrical Engineering, National Taiwan University, Taipei, Taiwan, R.O.C.

[8] Gerald W. Dahlmann, Eric M. Yeatman, Paul Young, Ian D. Robertson, and Stepan Lucyszyn. High q achieved in microwave inductors fabricated by parallel self-assembly. In *Tech. Digest, 11th International Conference on Solid-State Sensors and Actuators (Transducers 2001)*, Paper 3C2.02, pages 1098–1101, Munich, F.R. Germany, June 2001.

[9] Peter Enoksson. New structure for corner compensation in anisotropic KOH etching. *Journal of Micromechanics and Microengineering*, 7(3):141–144, September 1997.

[10] Richard P. Feynman, Robert B. Leighton, and Matthew Sands. *The Feynman Lectures on Physics*, volume II. Addison-Wesley Publishing Company, Reading, Massachusetts, 1964.

[11] K. Grenier, B.P. Barber, V. Lubecke, M. Zierdt, H. Safar, P. Pons, and P.L. Gammel. Integrated RF MEMS for single chip radio. In *Tech. Digest, 11th International Conference on Solid-State Sensors and Actuators (Transducers 2001)*, Paper 4C1.01, pages 1528–1531, Munich, F.R. Germany, June 2001.

[12] P. Hammond. *Energy Methods in Electromagnetism.* Oxford University Press, New York, New York, 1981.

[13] Hermann A. Haus and James R. Melcher. *Electromagnetic Fields and Energy.* Prentice Hall, Inc., Upper Saddle River, New Jersey, 1989.

[14] Stephen M. Hou, Jeffrey H. Lang, Alexander H. Slocum, Alexis C. Weber, and James H. White. A high-q widely-tunable gigahertz electromagnetic cavity resonator. In *Solid-State Sensor and Actuator Workshop*, Hilton Head Island, South Carolina, June 2004.

[15] James L. Jellison. Effect of surface contamination of the thermocompression bondability of gold. *IEEE Transactions of Parts, Hybrids, and Packaging*, PHP-11(3):206–211, September 1975.

[16] James L. Jellison. Kinetics of thermocompression bonding to organic contaminated gold surfaces. *IEEE Transactions of Parts, Hybrids, and Packaging*, PHP-13(2):132–137, June 1977.

[17] Darko Kajfez and Pierre Guillon. *Dielectric Resonators.* Artech House, Inc., Norwood, Massachusetts, 1986.

[18] David R. Lide, editor. *CRC Handbook of Chemistry and Physics.* CRC Press, 84 edition, 2003.

[19] Liwei Lin, Roger T. Howe, and Albert P. Pisano. Microelectromechanical filters for signal processing. *Journal of Microelectromechanical Systems*, 7(3):286–294, September 1998.

[20] Mark K. Long, Joel W. Burdick, and Erik K. Antonsson. Design of compensation structures for anisotropic etching. In *Technical Proceedings of the 1999 International Conference on Modeling and Simulation of Microsystems*, pages 124–127, San Juan, PR, 1999.

[21] Joseph Lutsky, Rajan Naik, Rafael Reif, and Charles G. Sodini. RF bandpass filters using thin film acoustic resonators. Technical Report 898, Microsystems Technology Laboratories, Massachusetts Institute of Technology, February 1998.

[22] Joseph J. Lutsky. *A Sealed Cavity Thin-Film Acoustic Resonator Process for RF Bandpass Filters.* PhD thesis, Massachusetts Insitute of Technology, March 1997.

[23] Nadim Maluf. *An Introduction to Microelectromechanical Systems Engineering.* Artech House, Boston, Massachusetts, 2000.

[24] Kitada Masahiro and Shimizu Noboru. Effects of temperature, thickness and atmosphere on mixing in au-ti bilayer thin films. *Journal of Materials Science*, 28:5088–5091, 1993.

[25] C.-E. Morosanu. The preparation, characterization and application of silicon nitride thin films. *Thin Solid Films*, 65:171–208, 1980.

[26] Rajan S. Naik, Joseph J. Lutsky, Rafael Reif, and Charles G. Sodini. Electromechanical coupling constant extraction of thin-film piezoelectric materials using a bulk acoustic wave resonator. Technical Report 900, Microsystems Technology Laboratories, Massachusetts Institute of Technology, February 1998.

[27] James W. Nilsson and Susan A. Riedel. *Electric Circuits.* Addison-Wesley Publishing Company, Reading, Massachusetts, 1996.

[28] G. Piazza, R. Abdolvand, and F. Ayazi. Voltage-tunable piezoelectrically-transduced single-crysal silicon resonators on SOI substrate. In *The Sixteenth IEEE International Conference on Microelectromechanical Systems, 2003*, pages 149–152, January 2003.

[29] James D. Plummer, Michael D. Deal, and Peter B. Griffin. *Silicon VLSI Technology: Fundamentals, Practice and Modeling.* Prentice Hall, Inc., Upper Saddle River, New Jersey, 2000.

[30] H. Sandmaier, H.L. Offereins, K. Kühl, and W. Lang. Corner compensation techniques in anisotropic etching of (100)-silicon using aqueous KOH. In *Tech. Digest, 7th International Conference on Solid-State Sensors and Actuators (Transducers 1991)*, pages 456–459, San Francisco, CA, 1991.

[31] H. Schröder, E. Obermeier, and A. Steckenborn. Micropyramidal hillocks on KOH etched {100} silicon surfaces: Formation, prevention and removal. *Journal of Micromechanics and Microengineering*, 9(2):139–145, June 1999.

[32] George N. Schwartz. A novel precision voltage reference using a micromechanical resonator. Master's thesis, Massachusetts Insitute of Technology, June 1998.

[33] Stephen D. Senturia. *Microsystems Design.* Kluwer Academic Publishers, Boston, Massachusetts, 2001.

[34] S. Mark Spearing. Mems materials and processes: A research overview. In *Proceedings of the Advanced Materials for Micro- and Nano-Systems (AMMNS) Programme of the Singapore-MIT Alliance Symposium*, Singapore, Singapore, January 2003.

[35] William C. Tang, Tu-Cuong H. Nguyen, and Roger T. Howe. Laterally driven polysilicon resonant microstructures. *IEEE Micro Electromechanical Systems Workshop*, February 1989.

[36] Christine H. Tsau, Martin A. Schmidt, and S. Mark Spearing. Characterization of low temperature, wafer-level gold-gold thermocompression bonds. In *Materials Research Society Symposia Proceedings of Materials Science of Microelectromechanical Systems (MEMS) Devices II*, volume 605, pages 171–176, Boston, Massachusetts, 1999.

[37] Christine H. Tsau, Martin A. Schmidt, and S. Mark Spearing. Wafer-level thermocompression bonds. In *Proceedings of the Advanced Materials for Micro- and Nano-Systems (AMMNS) Programme of the Singapore-MIT Alliance Symposium*, Singapore, Singapore, January 2003.

[38] Christine H. Tsau, S. Mark Spearing, and Martin A. Schmidt. Fabrication of wafer-level thermocompression bonds. *Journal of Microelectromechanical Systems*, 11(6):641–647, December 2002.

[39] Jing Wang, Zeying Ren, and Clark T.-C. Nguyen. Self-aligned 1.14-GHz vibrating radial-mode disk resonators. *Transducers 03*, 2:947–950, June 2003.

[40] Kun Wang and Clark T.-C. Nguyen. High-order medium frequency micromechanical electronic filters. *Journal of Microelectromechanical Systems*, 8(4):534–557, December 1999.

[41] Kun Wang, Ark-Chew Wong, and Clark T.-C. Nguyen. VHF free-free beam high-Q micromechanical resonators. *Journal of Microelectromechanical Systems*, 9(3):347–360, September 2000.

[42] Alexis Christian Weber. Precision passive alignment of wafers. Master's thesis, Massachusetts Insitute of Technology, February 2002.

[43] Jun-Bo Yoon, Byeong-Il Kim, Yun-Seok Choi, and Euisik Yoon. 3-D lithography and metal surface micromachining for RF and microwaves MEMS. In *The Fifteenth IEEE International Conference on Microelectromechanical Systems, 2002*, pages 673–676, January 2002.

[44] Qingxin Zhang, Litian Liu, and Zhijian Li. A new approach to convex corner compensation for anisotropic etching of (100) silicon in KOH. *Sensors and Actuators A*, 56(3):251–254, 1996.